Recent progress in organic solar cells (Part II device engineering)

Yahui Liu[1], Bowen Liu[2], Chang-Qi Ma[2*], Fei Huang[3], Guitao Feng[4], Hongzheng Chen[5], Jianhui Hou[6], Lingpeng Yan[2], Qingya Wei[7], Qun Luo[2*], Qinye Bao[8*], Wei Ma[9*], Wei Liu[7], Weiwei Li[4], Xiangjian Wan[10], Xiaotian Hu[11*], Yanchun Han[12*], Yaowen Li[13*], Yinhua Zhou[14*], Yingping Zou[7], Yiwang Chen[11*], Yuqiang Liu[1*], Lei Meng[6*], Yongfang Li[6,13*], Yongsheng Chen[10], Zheng Tang[15*], Zhicheng Hu[3], Zhi-Guo Zhang[16] & Zhishan Bo[1*]

[1]*College of Textiles & Clothing, State Key Laboratory of Bio-fibers and Eco-textiles, Qingdao University, Qingdao 266071, China;*
[2]*Suzhou Institute of Nano-Tech and Nano-Bionics, Chinese Academy of Sciences, Suzhou 215123 China;*
[3]*Institute of Polymer Optoelectronic Materials and Devices, State Key Laboratory of Luminescent Materials and Devices, South China University of Technology, Guangzhou 510640, China;*
[4]*Beijing Advanced Innovation Center for Soft Matter Science and Engineering & State Key Laboratory of Organic-Inorganic Composites, Beijing University of Chemical Technology, Beijing 100029, China;*
[5]*State Key Laboratory of Silicon Materials, MOE Key Laboratory of Macromolecular Synthesis and Functionalization, Department of Polymer Science and Engineering, Zhejiang University, Hangzhou 310027, China;*
[6]*Beijing National Laboratory for Molecular Sciences, Institute of Chemistry, Chinese Academy of Sciences, Beijing 100190, China;*
[7]*State Key Laboratory of Powder Metallurgy, College of Chemistry and Chemical Engineering, Central South University, Changsha 410083, China;*
[8]*School of Physics and Electronic Science, East China Normal University, Shanghai 200241, China;*
[9]*State Key Laboratory for Mechanical Behavior of Materials, Xi'an Jiaotong University, Xi'an 710049, China;*
[10]*State Key Laboratory and Institute of Elemento-Organic Chemistry, Key Laboratory of Functional Polymer Materials, College of Chemistry, Nankai University, Tianjin 300071, China;*
[11]*College of Chemistry/Institute of Polymers and Energy Chemistry (IPEC), Nanchang University, Nanchang 330031 China;*
[12]*State Key Laboratory of Polymer Physics and Chemistry, Changchun Institute of Applied Chemistry, Chinese Academy of Sciences, Changchun 130022, China;*
[13]*Laboratory of Advanced Optoelectronic Materials, College of Chemistry, Chemical Engineering and Materials Science, Soochow University, Suzhou 215123 China;*
[14]*Wuhan National Laboratory for Optoelectronics, Huazhong University of Science and Technology, Wuhan 430074 China;*
[15]*Center for Advanced Low-Dimension Materials, State Key Laboratory for Modification of Chemical Fibers and Polymer Materials, College of Materials Science and Engineering, Donghua University, Shanghai 201620, China;*
[16]*State Key Laboratory of Chemical Resource Engineering, Beijing Advanced Innovation Center for Soft Matter Science and Engineering, Beijing University of Chemical Technology, Beijing 100029, China*

Received March 21, 2022; accepted April 21, 2022; published online May 26, 2022

Organic solar cells (OSCs) have gained a rapid development in the past two decades and the power conversion efficiency (PCE) of single-junction OSC has recently approached 20%. The novel materials and device engineering are two key factors of this evolution. In this review, the device engineering, including morphology characterization and optimization, device physics, flexible and large-area OSCs, and stability of OSCs are systematically summarized. In addition, the current challenges, problems and future developments are also discussed.

Corresponding authors (email: cqma2011@sinano.ac.cn; qluo2011@sinano.ac.cn; qybao@clpm.ecnu.edu.cn; msewma@xjtu.edu.cn; ychan@ciac.ac.cn; happyhu@ncu.edu.cn; ywli@suda.edu.cn; yh_zhou@hust.edu.cn; ywchen@ncu.edu.cn; yqliu@qdu.edu.cn; menglei@iccas.ac.cn; liyf@iccas.ac.cn; ztang@dhu.edu.cn; zsbo@bnu.edu.cn)

organic solar cells, device engineering, flexible solar cells, device physics, stability

1   Introduction

Organic solar cells (OSCs) belong to a multidisciplinary field composed of chemistry, materials science, physics, engineering, *etc*. For a better reviewing of this field, we briefly divide the research field of OSCs into two parts: material science and device engineering. In our previous review, the material science part of OSCs, including conjugated polymer donors and acceptors, small molecular donors and acceptors, and interface materials, was systematically summarized [1]. The nano-morphology of active layer is pivotal to the device performance. An ideal bicontinuous interpenetrating network nano-morphology of active layer can be usually obtained by morphology optimization *via* additive treatment, thermal annealing, *etc*., which can largely change the phase separation and facilitate the charge transport and collection, *etc*. Besides, the evolution of nano-morphology of active layer can be characterized by optical microscopy (OM), atomic force microscopy (AFM), transmission electron microscopy (TEM), photo-induced atomic force microscopy (PiFM), resonant soft X-ray scattering (RSoXS), and grazing incidence wide-angle X-ray scattering (GIWAXS), *etc*. Moreover, the device physics, including interfacial electronic structures and energy loss, is important for understanding the working mechanism of OSCs, and thus helps to seek new approaches to further improve the photovoltaic performance of OSCs.

Nowadays, small area single-junction OSCs can achieve a high PCE over 19% [2], which can meet the threshold of commercialized application. For further practical application, flexible OSCs and scaling-up of OSCs have attracted much attention during the past several years. Besides, the degradation and stability of OSCs are gradually becoming more and more important. The PCEs of flexible and large-area OSCs are usually lower than those of small area ones, which can be attributed to electrical, geometric, optical and other losses. The substrates, electrodes, interfacial layers, and photoactive layers of flexible OSCs are the main research topic for the further improvement of photovoltaic performance. Besides, large-scaling up of OSCs is also facing challenges including the printing compatibility of the material, printing technology, *etc*. At last, except for water and oxygen, OSCs under operation encounter stresses of light, heat and electric field, which will also lead to the performance decays. All in all, these factors are vital for future application of OSCs. Herein, we provide a detailed review about the device engineering and hope that this review could inspire more deep researches and push forward the application of OSCs.

2   Morphology characterization and optimization

In OSCs with bulk heterojunctions, exciton formation as well as charge generation and diffusion occur in the photoactive layer. Therefore, methods to observe and control the active layer morphology have been continuously explored. The observation of the active layer depends on the contrast of the blend film, while the control of the morphology depends on the molecular self- and hetero- interactions including the solvent, which in turn are related to the molecular structures. With the rapid development of nonfullerene acceptors (NFA), it is essential to understand the relations between morphology optimization and involved molecular structures. In this section, we will focus on the effect of structures on molecular interaction and packing of the donor or acceptor, as well as the donor and acceptor phase composition and distribution. We specifically consider the morphological modification strategy in the nonfullerene era. Meanwhile, this part based on the quantitative morphological parameters satisfied by various characterization techniques will be briefly introduced.

2.1   Morphology characterization

For bulk heterojunctions, the universal characterization techniques include imaging and scattering. The readily available imaging tools are OM, AFM, PiFM, and TEM. These types of real-space data are easy to be intuitively understood, and thus make these tools for fundamental morphological characterization. AFM has an advantage in observing surface roughness, PiFM can be used to distinguish the morphologies of donors and acceptors in the BHJ active layer, and OM and TEM are usually applied in observing the composition or size distribution. Combining the energy-filtered TEM and the contrast provided by electron energy loss spectroscopy, quantitative compositional information can be obtained by model calculations [3,4]. However, this method is more complex and is used rarely. In addition to the characterization techniques for the active layer morphology of the OSCs, recently, cryogenic trans-

mission electron microscopy (Cryo-TEM) has also been used to characterize the aggregation of the donors and acceptors in their blend solutions [5]. Besides, for morphology characterization of the active layers, Raman spectroscopy was employed to characterize the neat and blend films, especially for the ternary active layers. The compatibility of used materials can be reflected from the Raman mapping image or contact angle images [6,7].

RSoXS and GIWAXS are frequently used to probe polymer blends, which can determine the molecular packing and phase size distribution by averaging thousands of domains and provide statistically meaningful information [8–10]. Again, scattering is unaffected by features in the device that overlap each other in the 2D projection. For NFA based film, GIWAXS is a sufficient tool to characterize molecular stacking and crystallinity. The particular challenge in characterizing phase composition arises from the greatly reduced contrast between the blended materials, as relative to the film using fullerenes as acceptors. This reduction in contrast is due largely to the more similar C/H ratio and structural motif ratio between the donor and NFA. Regarding this, the solid-state NMR (ss-NMR) that yields nanoscale insight on local order and composition as well as interfacial structures would be a useful complementary method [11,12].

2.2   Morphology optimization

In this section, we will discuss recent advances in the morphology control of the photoactive layers and organize the optimization methods into two categories: thermodynamic and kinetic optimization. Thermodynamic methods include the control of interactions between self- and hetero-molecules (*e.g.*, acceptor and donor). Kinetic methods are various controls of solution aggregation, film formation and post-film treatment, which can modulate the crystallization and phase separation to manage the final film morphology.

2.2.1   Thermodynamic optimization

We will divide the thermodynamic optimization into two parts for the control of interactions between homologous and heterologous molecules. Owing to the generally fused-ring-conjugated structure of efficient NFAs, the small molecules have a strong tendency to assemble in a stable thermodynamic state. Therefore, modulating the intermolecular interactions is an effective strategy to regulate the molecular packing of acceptors [13]. In this regard, chemical structure design is a simple and effective method, such as the introduction of non-covalent interactions. For example, Li *et al.* [14] demonstrated the presence of hydrogen bonds between the acceptors with hydroxyl groups could result in superior molecular crystallinity compared with the counterpart (ITIC) (Figure 1a–c). Moreover, the molecule with hydroxyl groups on both terminals (IT-DOH) shows stronger

molecular packing along the backbone and π-π directions than that with hydroxyl groups on one terminal only (IT-OH), and thus yields a maximum efficiency of 12.5% for non-annealed PBDB-T-based devices. Similarly, Zhan *et al.* [15] achieved the modulation of molecule packing from 2-dimensional to 3-dimensional structure by introducing fluorine atoms into the end-group and benzene ring as side chain of the fused ring acceptor-INIC, respectively. The authors demonstrated by DFT calculations that the fluorinated FINIC dimers have four stable structures due to the fluorine-atom-introduced interaction. This is the basis for the formation of three-dimensional stacking in its single crystals. Even though they did not observe a similar three-dimensional structure in the corresponding polymer:NFA blends, it was demonstrated by GIWAXS that the fluorinated blends exhibited a superior crystallinity and face-on orientation. This is attributed to the improved dimeric packing following the fluorination of the end groups and side chains.

In addition to non-covalent interactions, the spatial steric hindrance of the side chains can also influence the arrangement characteristics of molecules, as reported by Zheng *et al.* [16]. As presented in Figure 1d, they concluded that the molecular orientation relative to the substrate changes from edge-on to face-on when the side chain switches from *n*-cetyl (85%) to 2-hexyldecyl (88%). Likewise, Peng *et al.* [17] reported an effective strategy of platinum (II) complexation to modulate the crystallinity of PSFTZ. It was shown in Figure 1e that the bulky benzene ring on the platinum (II) complex increases the steric hindrance along the polymer main chain and inhibits the polymer aggregation strength, resulting in improved device performance.

Interactions between homologous molecules generally affect their alignment behavior such as ordering, orientation, *etc.* [18,19]. The modulation of interactions between heterologous molecules will change their miscibility [20]. The miscibility of the donor and acceptor, as one of the driving forces for phase separation, tends to affect the domain size, domain composition, *etc.* [21,22]. Recently, Lee's group [23] showed that the miscibility of the donor and acceptor also affects the homogeneity of the morphology along the vertical direction. They found that the phase characteristics in thick films for the system with good miscibility are similar to those in thin films, while the systems with poor miscibility show significant differences (Figure 2a). Therefore, by miscibility modulation, it is promising to achieve a uniform morphological distribution in the vertical direction in thick films. This strategy offers the possibility for the preparation of efficient thick film devices. Ade and Ye *et al.* [24,25] have done a series of prominent works that illustrate how miscibility controls phase separation and composition. They established a quantitative relationship between amorphous-amorphous interaction parameter (χ_{aa}) and the filling factor (FF) of OSCs. This model relates the domain composition,
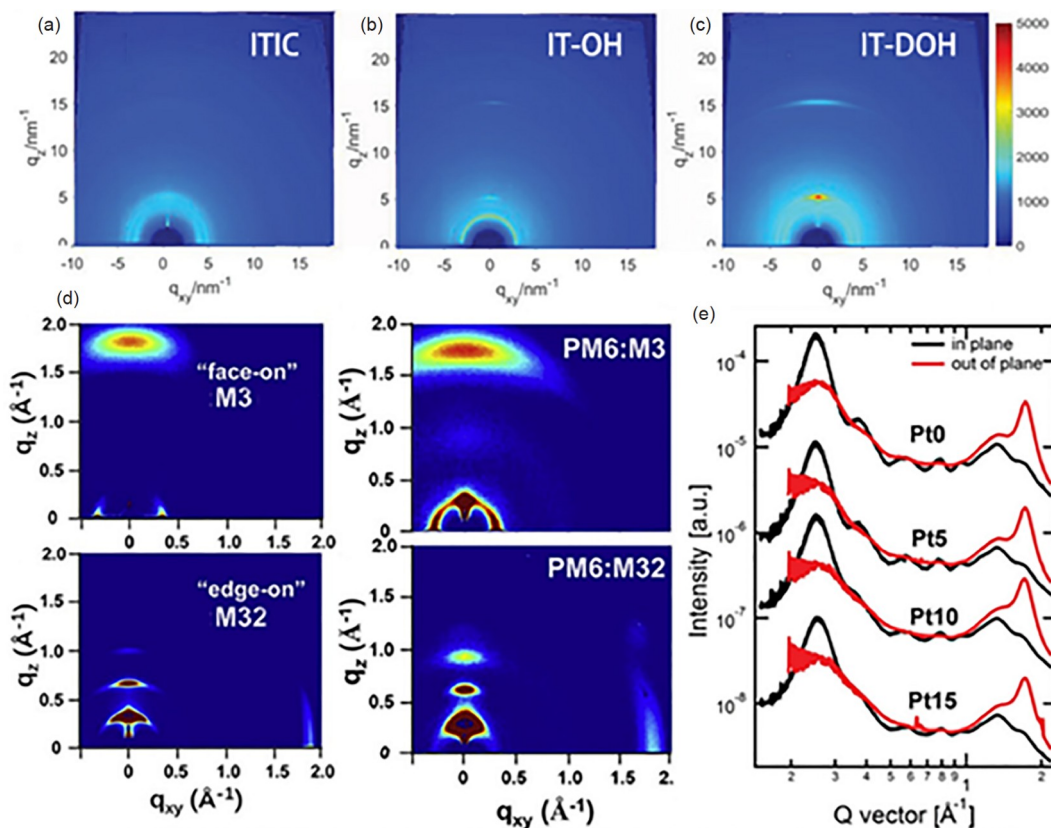
Figure 1   (a–c) GIWAXS images of ITIC, IT-OH, and IT-DOH films [14]. (d) GIWAXS images of thin film based on neat M3, neat M32 and their blends with PM6 [16]. (e) The in-plane and out-of-plane line profiles of neat polymer films extracted from GIWAXS with different Pt ratio [17] (color online).

FF and χ_{aa}, which could be used as the basis for miscibility testing and simulation methods that will reduce the trial and error test. Besides, they proposed a framework of using percolation threshold and quench depth to guide morphology revolution *via* kinetic factors, which could be used to accelerate the morphology optimization in various systems.

Interactions between heterologous molecules become quite intricate in ternary and quaternary systems. In response, rather than directly establishing quantitative framework, inferences are often made based on comparative device performance coupled with physics measurements, molecular packing, phase separation or Hansen solubility parameter calculations. Even so, the following summary of empirical morphological optimization is still valuable. Li *et al*. [26] added the strongly crystalline polymer guest P1 to the classic PBDB-T:IT-M and PBDB-T:ITIC blends. The excellent compatibility between P1 and PBDB-T significantly improved the crystallinity of the blended film even at a small P1 content of 5%, resulting in optimized FF of the device exceeding 78%. This strategy of optimizing the host morphology by considering both crystallinity and compatibility has been widely applied in other systems and has been proved to be an effective method for improving the morphology and performance of multi-component systems [27,28]. Similarly, Lu *et al*. [29] discovered a hidden mole-

cular packing structure in the ITIC:ITIC-Th blends. They demonstrated that the packing regularity of this structure is stronger than that in both pure references, which yields improved carrier mobility and device performance. Moreover, as demonstrated by Hou *et al*. [30], it is effective to introduce interactions between the hosts and the guests by means of a solid additive (we consider as guests). Modulation of this interaction can optimize the nucleation potential of the acceptor molecules and thus improve their crystallinity.

Ma *et al*. [31] achieved balanced donor and acceptor crystallinity in ternary blends by regulating the miscibility of donors and acceptors. The authors reported that in the PBDB-T:FOIC blade-coated film, PBDB-T and FOIC were less compatible and formed a higher domain purity. As a result, the crystallinity of the acceptor can be considerably stronger than that of the donor under blade-coating induction, making the electron mobility higher than the hole mobility. In contrast, in the PTB7-Th:FOIC system, where the donor-acceptor compatibility is better than that of PBDB-T:FOIC blends, the improved crystallinity of the acceptor under scraping induction is not obvious. Based on the compatibility of these two systems and the characteristics of the blade-induced crystallization, the authors obtained balanced donor-acceptor crystallinity and carrier mobility by adjusting the ratio of PBDB-T:PTB7-Th.
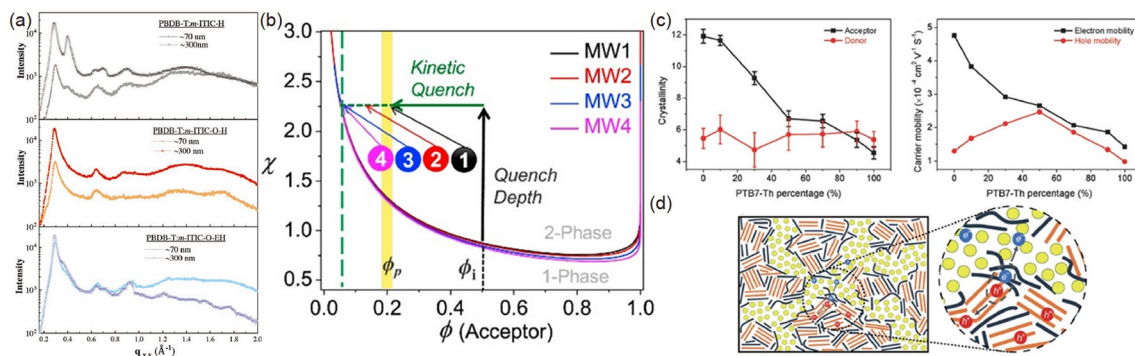
Figure 2 (a) GIWAXS scattering profiles along the in-plane direction for blends with different thickness [23]. (b) Composition of mixed domain estimated from R-SoXS for PM6:IT-4F blends that needed to be quenched close to the percolation threshold for best performance [25]. (c) The FOIC crystallinity quantified from GIWAXS and carrier mobility at different PTB7-Th content [31]. (d) Illustration of the hierarchical morphology in BTR:NITI:PC$_{71}$BM blends [32]. The green circles represent PC$_{71}$BM, the navy rods represent NITI and the orange rods represent BTR (color online).

In addition to crystallinity optimization, an excellent research case for optimizing phase separation was reported by Zhu and Liu *et al.* [32]. In this work, they used a strongly crystalline small molecule donor-BTR, a weakly crystalline small molecule acceptor-NITI, and a fullerene acceptor-PC$_{71}$BM. The innovation of this project is the successful construction of a hierarchical phase separation by exploiting the compatibility differences of the three materials. Specifically, the strong compatibility between BTR and NITI leads to the tendency of remaining mixing. However, due to the mismatch in crystallinity, the electrons in the NITI-dominated regions cannot be efficiently transported and collected by the electrodes, and thus the FF and device performance of this system are modest. The authors then introduced PC$_{71}$BM, which has weak intermolecular interactions and good compatibility with NITI, but poor compatibility with BTR due to strong intermolecular interactions. Therefore, under the influence of intermolecular interactions, PC$_{71}$BM tends to mix with NITI rather than BTR, resulting in a hierarchical phase separation in the ternary system with BTR:NITI providing the D/A interface and NITI:PC$_{71}$BM providing the electron transport channel (Figure 2d). This profile improves the disadvantage of electron transport in NITI and avoids the high voltage loss caused by the BTR:PC$_{71}$BM interface, thus obtaining high voltage, FF and energy conversion efficiency at the same time.

2.2.2 Kinetic optimization

In the previous section, we reviewed the efficient strategies for optimizing morphology in binary and ternary systems from the perspective of intermolecular interaction. In this section, we will discuss the morphological optimization in the film formation period from the kinetic point of view. Based on the characteristics of solution-processed film, we will divide them into three parts: solution state, film formation state and post-film treatment, and discuss the influence of each part on the crystallization and phase separation

stages as well as on the final morphology.

Ma *et al.* discussed the regulation of molecular pre-aggregation states in solutions. It should be noted that the characterization of molecular aggregation states is currently focused on dilute solutions at low concentrations, and there remain difficulties in characterizing them for high concentration cases. Therefore, we only comment empirically on the strategies for regulating the pre-aggregation state in solution. Considering the interactions between solvent molecules and solute molecules, the solvent is one of the principal factors affecting the pre-aggregation state. The use of distinct solutions to modulate the pre-aggregation state of molecules, especially polymers, has become a widely used method for morphology modulation [33–36]. Yan's group [37,38] has achieved a series of progress in this area, the most prominent of which is the regulation of a class of polymers with temperature-dependent aggregation properties. They used binary solvent of CB and DCB, combining with solution temperature control, to regulate the aggregation state of PffBT4T-2OD. In addition, they used non-halogenated solvent 1,2,4-trimethylbenzene (TMB) to modulate the aggregation state and film orientation of PffBT4T-C$_8$C$_{12}$ (Figure 3a). The combination of solvent and temperature management provides more scope for optimization in regulating the molecular pre-aggregation states and has been broadly applied in nonfullerene systems. For example, the crystallinity of molecules can be improved by exploiting the tendency of molecules to assemble spontaneously in the poor solvents. As indicated in Figure 3b, Peng's group [39] reported a strategy that mainly affects the solution pre-aggregation behavior of small molecules and modulates the crystallization mode and crystallization intensity in the film by changing the rest time of the solvent. This work shows the importance of the solution pre-aggregation state in the morphological evolution of thin film. The subsequent structural evolution during film formation needs to be supported by *in situ* observations.

On the other hand, Ma *et al.* [40] showed that in addition to
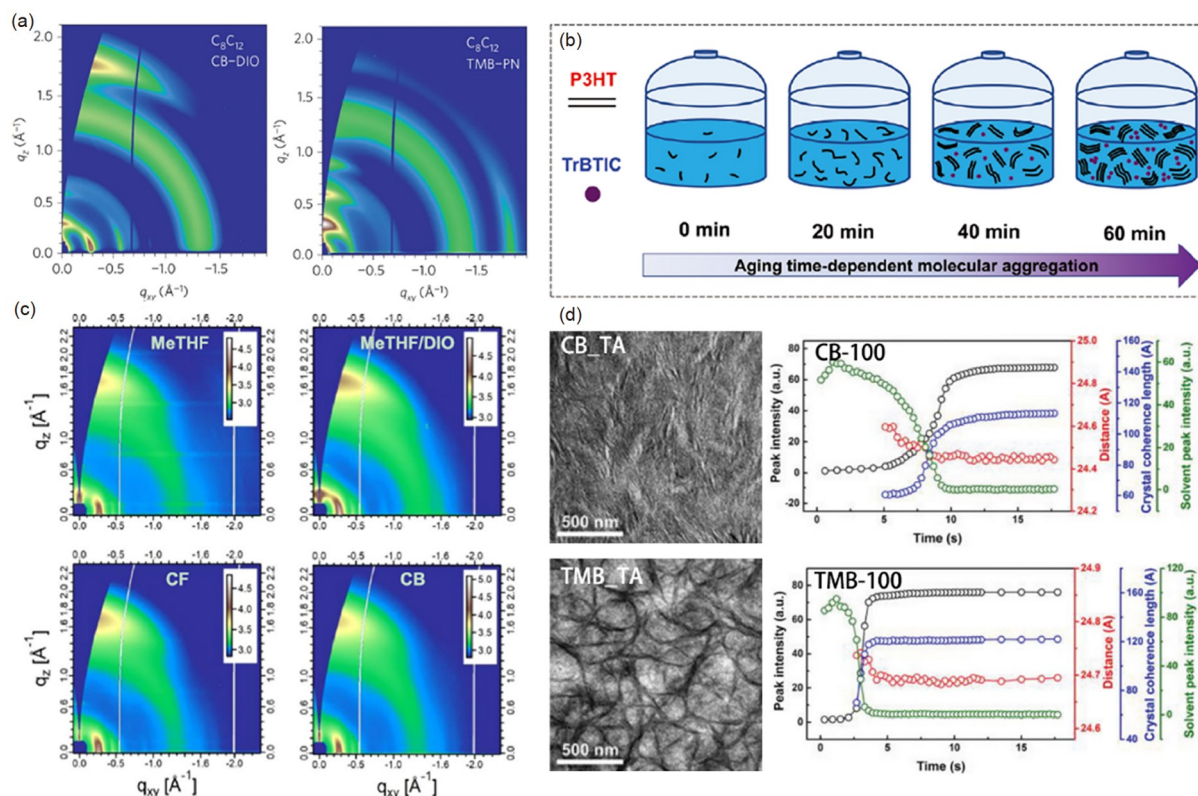
Figure 3 (a) GIWAXS images of PffBT4T-C$_8$C$_{12}$:PC$_{71}$BM films processed with different solvents [38]. (b) Illustration of the solution-ageing process [39]. (c) GIWAXS images of PTzBI:N2200 blends under different solvent condition [40]. (d) TEM images of PTzBI-Si:N2200 blends processed with CB and TMB and corresponding *in-situ* results [41] (color online).

the solubility difference caused by the solvent, the evaporation rate difference due to different boiling points also affects the blend morphology under various fabrication temperature. They compared the morphology and device performance of PTzBI:N2200 blends processed with MeTHF, MeTHF/DIO, CF, and CB solvents, and found that the crystallization of N2200 could be effectively reduced in MeTHF case as depicted in Figure 3c. In fact, MeTHF, as a poor solvent for N2200, can improve N2200 pre-aggregation state in solution to some extent. However, considering the low boiling point of MeTHF (~80 °C), it would significantly shorten the film formation time and inhibit the crystal growth of the polymer, thus obtaining a weakly crystalline and small phase separation scale. A similar result was also found by Liu and co-workers [41], who proposed that PTzBI-Si and N2200 have good compatibility, so that a homogeneous mixing state can be maintained in the solution state. Therefore, the mixed morphology can be frozen in the earlier phase separation stage and a moderate crystalline fiber network will be maintained under MeTHF-processed condition (Figure 3d). Such work highlights the importance of solvent evaporation during morphological evolution.

Basically, owing to the processing temperature can influence the solvent evaporation rate and the solute aggregation, it can also be considered to some extent that temperature

plays a solvent-like role. The advantage of the temperature field is that it can be continuously regulated, so there is more room for optimization in the film formation process. Ma's group [42,43] found that in slot-die coating, changing the solution temperature and substrate temperature can modulate thermodynamic state of the solution and the kinetic process of crystallization. They reported that adjusting the solution and base temperature can obtain similar pre-aggregation states and crystallization kinetic processes even processed with different solvents, resulting in similar active layer morphology and device performance (Figure 4a, b). This study is a critical finding for the future progress of OSCs in terms of their scalable production and optimization.

In fact, the morphology of the film formation period is influenced not only by the solvent evaporation rate but also by phase separation behavior. The common phase separation include liquid-liquid (L-L), liquid-solid (L-S), and solid-solid (S-S) phase separation. In general, the factors that influence the phase separation mode are the composition, *i.e.*, the composition of the solvent and the composition of the donor and acceptor. Janssen *et al.* [44] showed by *in-situ* optical measurements that binary solvent could cause the onset of polymer aggregation to occur before L-L phase separation in PDPP5T-based fullerene systems. In other words, the phase separation behavior in binary solvents results from the dif-
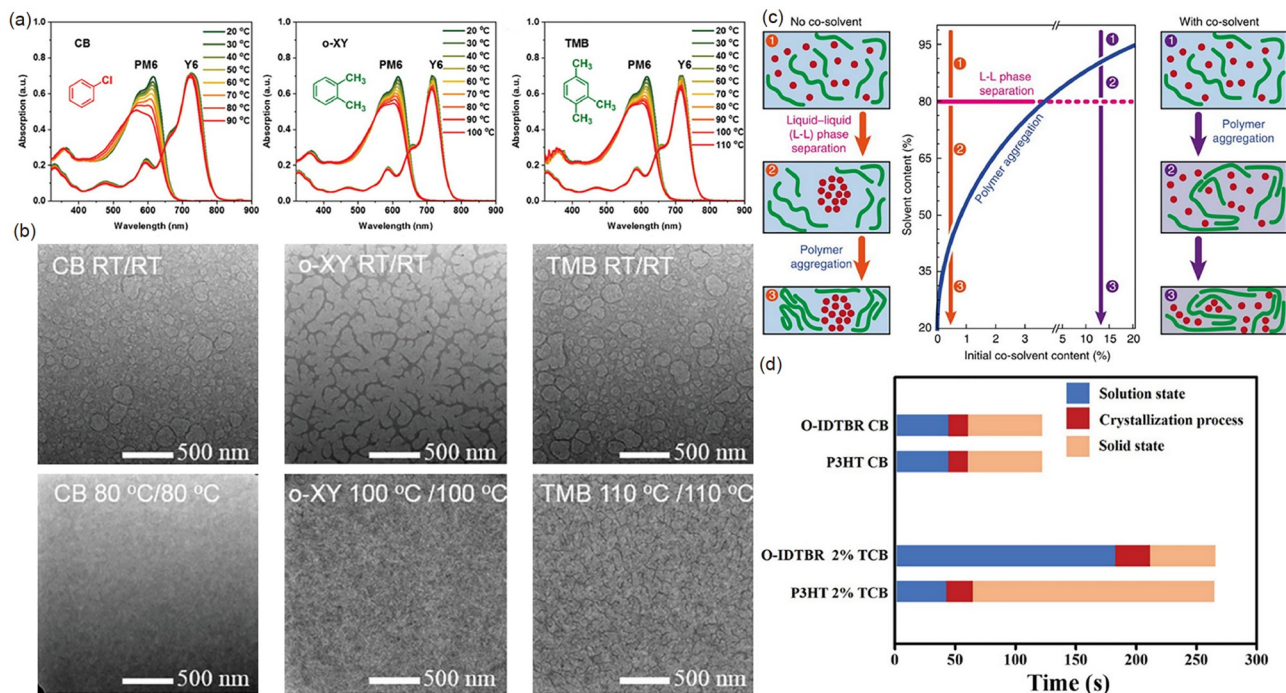
Figure 4   (a) Temperature-dependent UV-vis absorption spectra of PM6 and Y6 in CB, o-XY, and TMB [42]. (b) TEM images of PM6:Y6 blends prepared by CB, o-XY, and TMB with different solution temperature [42]. (c) The role of binary solvent in modulating polymer aggregation at higher solvent contents which, in turn, is expected to result in large-scale liquid-liquid phase separation during film drying [44]. (d) The crystallization process of P3HT and o-IDTBR within film-forming period without and with TCB in CB solvent that is deduced from *in-situ* UV absorption spectra [45] (color online).

ference in evaporation rate and solubility capability of the solvents. Therefore, the type and ratio of binary solvents can be modulated to optimize the active layer morphology (Figure 4c). For instance, Han *et al*. [45] introduced a binary solvent CB:TCB to optimize the crystallization and vertical phase separation of the active layer in P3HT:O-IDTBR system. The authors showed that due to the higher boiling point of TCB as well as its superior solubility for O-IDTBR, the binary solvent was able to prolong the film formation time and separate the crystallization processes of P3HT and O-IDTBR compared with CB. The separated crystallization processes prevent interference each other, resulting in highly crystalline film.

After the vast majority of the solvent molecules have swept away from the film, the molecular chain segments have almost lost their mobility. In this case, the main objective of morphology optimization is to provide molecular motion energy or to reduce the molecular motion potential. Commonly used methods are thermal or solvent evaporation annealing to optimize the morphology by improving the phase separation or crystallization of the blended film, and a detailed description can be found in the literature [46–49].
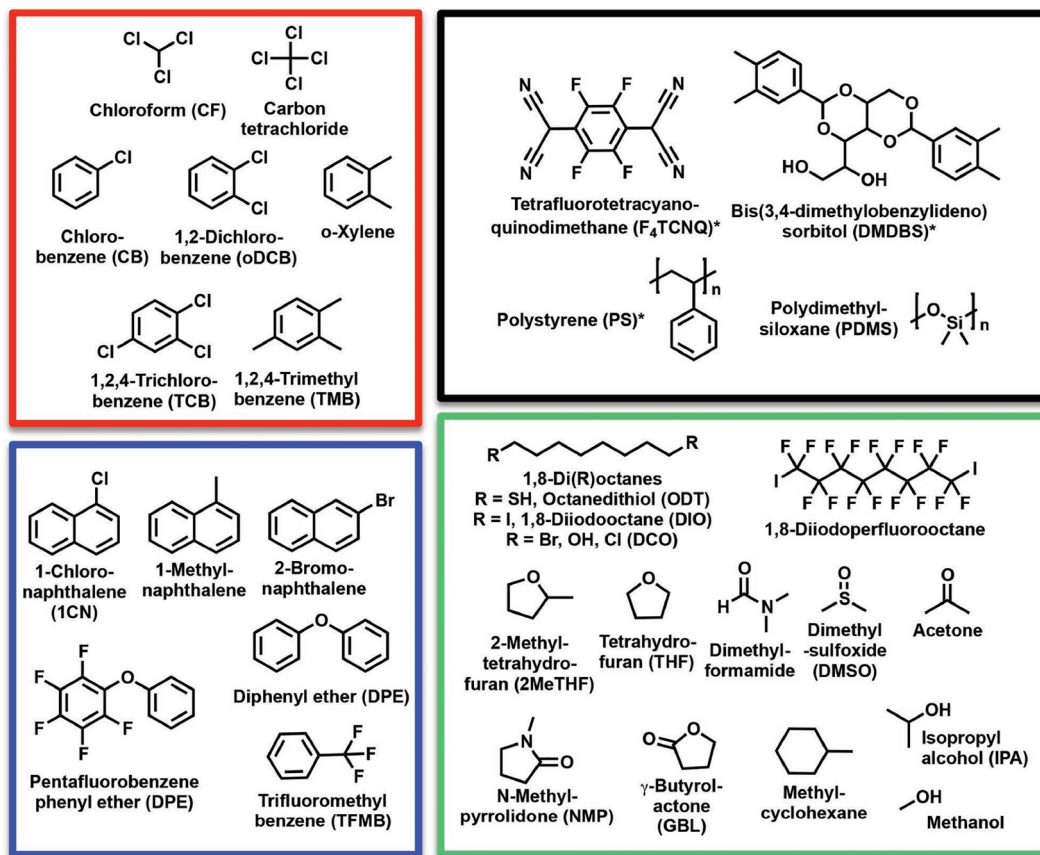
Additives including solvent and solid additives can well control the active layer morphology during the film decomposition [48,50]. The first solvent additive was reported by Peet *et al*. [51], P3HT:PC$_{61}$BM blend film display higher photocurrent with the addition of *n*-octylthiol. Subsequently,

they used *n*-octanedithiol as the additives to promote the phase separation of PCPDTBT:PC$_{71}$BM blend films, and the PCE was boosted from 2.8% to 5.5% [52]. Rogers *et al*. [53] conducted X-ray diffraction, and revealed that the solvent additive could increase the crystalline of the donor polymers. Further investigation indicate that other 1,8-di(R)octane compounds (R can be thio-, chloro-, bromo-, iodo-, cyano-, and acetate) could be also used as solvent additives. Nowadays, as shown in Figure 5, 1,8-diiodooctane (DIO), 1-chloronaphthalene (1CN), diphenyl ether (DPE), *etc*. are the normal used solvent additives. Similarly, solid additives are also successfully developed. Generally speaking, due to the different properties of host solvent and additives (such as boiling point and solubility capability), the solvent additives can much influence the phase morphology such as domain size, molecular crystallinity and molecular orientation, thus yielding enhanced photovoltaic performance. Additives can also much improve the photovoltaic performance of NFAs-based OSCs. Besides, thermal and solvent annealing as commonly used post-film treatment methods can also adjust the phase morphology [54], and ternary or quandary strategy [55] are also used to improve the photovoltaic performance of OSCs.

2.3   Outlook

In general, the means of morphology optimization are quite

Figure 5   Chemical structures of normally used deposition solvents (red), aromatic solvent additives (blue), nonaromatic solvent additives (green), and solid additives (black) [48] (color online).

mature and can basically meet the demands of the current system. Currently, the efficient system is also effective in phase separation under a broader field, and hence the subsequent morphology optimization needs to pay more attention to the molecular alignment, defect optimization, *etc*. Furthermore, along with the rapid progress of NFAs based device efficiency, the industrialization and future applications of OSCs should be highlighted. The stability of the device is considered to be an important factor limiting its application. In this context, future morphological studies of OSCs should be focused on the questions encountered in stability and industrial production. Harald *et al*. [56] have presented a pioneer work in terms of molecular-diffusion-dominated stability analysis in the mixed amorphous phases. They related the elastic modulus of polymers and the glass transition temperature of NFAs with enthalpy interaction parameters and diffusion coefficients, and thus revealed that the most stable systems were the most miscible one. For the sake of detailed structure-property relations in terms of stability, the comprehensive study of the crystallization domain and the analysis of the relationship between the optimal efficiency morphology and the stable morphology are encouraged.

On the other hand, the question of how to apply the ex-perience of morphology optimization during the transition from laboratory to manufactory and from small-area spin coating to large-area printing has yet to be revealed. Ganapathysubramanian *et al*. [57] showed through modeling calculations that there is still room for the improvement of blade coating in terms of morphology optimization compared with spin coating. Chen *et al*. [58] have made a preliminary effort in this area by extracting a parameter that describes the state of the printing process: the impulse calculation. By comparing the impulse parameters of spin coating and printing processes, it is possible to relate small-area and large-area processes. Ma *et al*. [42] proposed that for the similar blended film morphology and device efficiency under different solvents processing, separately controlling the pre-aggregation states and film formation kinetics could be a practical approach.

3   Devices physics

3.1   Interfacial electronic structures in OSCs

The photophysical and charge transfer processes in semiconductor optoelectronic devices follow the basic rules drew up by the band theory, which functionalize the devices and

determine their merits. The intensive understanding of the interfacial electronic structures is thus of paramount importance in achieving high-performance OSCs. For example, the open-circuit voltage strongly depends on the energy difference between the highest occupied molecular orbital level (HOMO) of the donor and the lowest unoccupied molecular orbital level (LUMO) of the acceptor at donor/ acceptor (D/A) interface [59–61]. The LUMO energy offset at D/A interface provides driving force for exciton dissociation, although recent studies announce its futility in nonfullerene OSCs [41,62,63]. Meanwhile, the electronic energetics at the electrode interface control charge collection efficiency. The investigation on these interfacial physics helps to quickly screen the appropriate D/A systems and charge-selective contact towards the highly efficient OSCs.

Empirical assessment of the interfacial energy level alignments, for example, by individually measuring and comparing the energy levels of donors and acceptors, generally ignores the real situation of an organic-organic contact where multiple factors influence the resulting interface energetics, such as (dark) ground state integer charge transfer (ICT) [64], interface dipole potential step [65] and charge-transfer complex [66]. This can possibly be one of the reasons why the research community has yet to reach an agreement concerning the typical role of energy level offset between D/A in novel nonfullerene OSCs. The electronic structures of the formed organic interfaces depend on the interaction strength at the heterojunction. The solution-processed organic/organic interfaces can be described by the ICT model, where integer charge transfer occurs *via* tunneling without the presence of interfacial chemical interaction [64]. The interface between organic layer and the underlying substrates also follows this regime. The details of the model and its applications in D/A and electrode interfaces will be introduced in the following sections. Meanwhile, we mainly focus on organic bulk heterojunction (BHJ) interfaces considering the widely used architecture of OSCs.

The cyclic voltammetry (CV) with the advantages of economical and low barrier to entry can provide the values of onset oxidation and onset reduction potentials as an estimation of the ionization potential (IP) and electron affinity (EA) of the materials, respectively. However, the scatter in data points can be large when fitting the CV-derived energy levels, hence undermining their credibility [67,68]. Reported CV values vary even for the same material in the publications due to the different experimental environment, instrument setup and data manipulation, which further make it difficult to construct a solid interfacial energy level diagram [61]. The photoelectron spectroscopy (PES) is one technology that can directly measure the accurate IP/EA values in ultrahigh vacuum.

The "directness" of PES is reflected by its fundamental principle, the Einstein's equation for photoelectric effect: $E_B = h\nu - E_K$. An incident light with photon energy of $h\nu$ overcomes the electron binding energy (E_B) if it is larger than the work function (WF) of the sample, and concomitantly triggers the electron emission from the surface with a kinetic energy (E_K). Ultraviolet photoelectron spectroscopy (UPS) and inverse photoelectron spectroscopy (IPES) are thus utilized with ultraviolet light (usually He Iα with the photon energy of 21.22 eV) and electron gun (5–10 eV) as the excitation source to excite the frontier-occupied electronic states and fulfill the frontier unoccupied electronic states of a solid, respectively. Figure 6 shows the PES installation of Qinye Bao's group at East China Normal University, Shanghai, China, and depicts the approach to access the energy parameters from UPS and IPES. In UPS spectra, the secondary-electron cutoff (E_{cutoff}) implies the highest binding energy of the photoelectrons, that is, photoelectrons with the lowest kinetic energy which determines the WF. Binding energy of the HOMO onset equals the energy difference between the Fermi level E_F and HOMO (E_F^{HOMO}), giving the IP by combining with the WF. IPES counts the emitted photons from the sample when the electron decays into the lower unoccupied states. The detector only allows the photons with a fixed energy, *i.e.*, the bandpass energy (E_{bp}), to
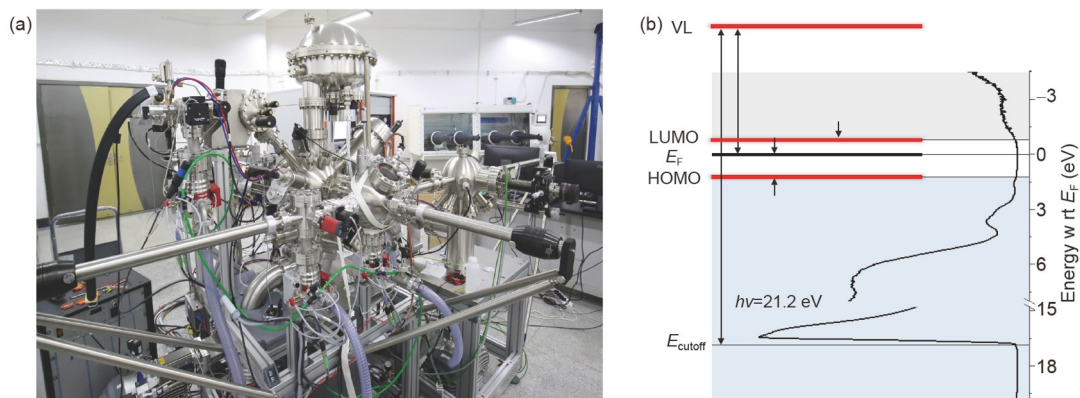
Figure 6 Schematics of (a) PES installation at East China Normal University. (b) Data extraction method of UPS and IPES (color online).

pass through the slit and then collects them. The detected energetic position in the unoccupied states region relies on changing the kinetic energy of the electron beam (E_{Kin}). Such so-called "isochromat" mode of IPES can be interpreted by the following equation: $E_B = E_{Kin} - E_{bp}$. The energy difference between the LUMO and E_F (E_F^{LUMO}) can be derived from the onset of the IPES spectra, hence providing the EA value.

The energy level alignment at the D:A BHJ interface can be precisely described by the ICT model based on the results from PES (Figure 7) [69]: (i) $E_{ICT+, D} < E_{ICT-, A}$, donor ICT+ state pins to acceptor ICT-state as a result of spontaneous integer charge transfer, leading to a potential step Δ to equilibrate the Fermi level; (ii) $E_{ICT+, D} \approx E_{ICT-, A}$, donor ICT+ state overlaps acceptor ICT-state with negligible Δ; (iii) $E_{ICT+, D} > E_{ICT-, A}$, vacuum level alignment without charge transfer at interface. The E_{ICT+} (E_{ICT-}) energy of the positive (negative) ICT state is related to the smallest energy required to take away one electron (the largest energy gained from adding one electron) from (to) the organic semiconductor molecule at the heterojunction interface producing the fully relaxed state. The values of $E_{ICT+/-}$ are determined by separately conducting UPS measurement on donor and acceptor films deposited on the different substrates with a large range of WFs. Generally, PEDOT:PSS (PEDOT: poly(3,4-ethylenedioxythiophene); PSS: poly(styrenesulfonic acid)) with a high WF (>5.1 eV) and Al with a low WF (~3.7 eV) are expected to result in Fermi level pinning to E_{ICT+} and E_{ICT-}, respectively. For the substrate with WF between the two pinning energies, the organic films will present the same WF with the substrate as there is negligible spontaneous charge transfer at organic/substrate interface [70].

The typical dependence of the WF of an organic film and its substrate is like a reverse of letter "Z", as shown in Figure 8a [70], which are well-known electron acceptors used in OSCs. The obtained E_{ICT-} values for C_{60}, C_{70}, $PC_{60}BM$, $PC_{70}BM$, $bisPC_{60}BM$, $trisPC_{60}BM$, and $IC_{60}BA$ are 4.57, 4.65, 4.31, 4.35, 4.12, 3.95, and 4.05 eV, respectively. Comparing those values with the E_{ICT+} of a donor, for example, rr-P3HT (4.0 eV), one can easily divide the heterojunction into the three cases (Figure 7), and thus draw a predicted energy level diagram at D:A interface. When $E_{ICT+, D} < E_{ICT-, A}$, the existence of interface dipole potential step Δ, can significantly increase the effective energy gap ΔEDA g. eff (defined as the $IP_D - EA_A$ after the contact where Δ is included), making bare comparison of these two values less responsible for the V_{OC} determination. The formed ICT states in the mid-gap act as trap sites to capture the oppositely-charged polarons in Figure 8b. However, in the case of $E_{ICT+, D} \approx E_{ICT-, A}$, a slight difference with low density of ICT states not only avoids ICT trap-assisted recombination, but also facilitates the exciton dissociation by occupying the most tightly bound sites in the (dark) ground state [71]. The same scenario is true for a great deal of high-performing polymer donors combining fullerene derivatives as acceptors [70]. In a more comprehensive study focused on TQ1:$PC_{71}BM$ binary blend, the $E_{ICT+, D}$ and $E_{ICT-, A}$ are found both at 4.35 eV (Figure 8c, d), which is the primary reason of the small V_{OC} loss of 0.25 eV observed in the corresponding OPV device [69]. The most popular nonfullerene PM6:Y6-based ternary system also follows such criteria where the E_{ICT+} value of PM6 was found to be 4.50 eV, perfectly matching the E_{ICT-} value of Y6 (4.34 eV), see Figure 8e, f [28].

Optimistically, we can thus propose a basic design rule for achieving high performance OPVs with minimized V_{OC} loss, that is $E_{ICT+, D} \approx E_{ICT-, A}$. However, keep in mind that the

(i) $E_{ICT+,D} > E_{ICT-,A}$ (ii) $E_{ICT+,D} \approx E_{ICT-,A}$ (iii) $E_{ICT+,D} < E_{ICT-,A}$
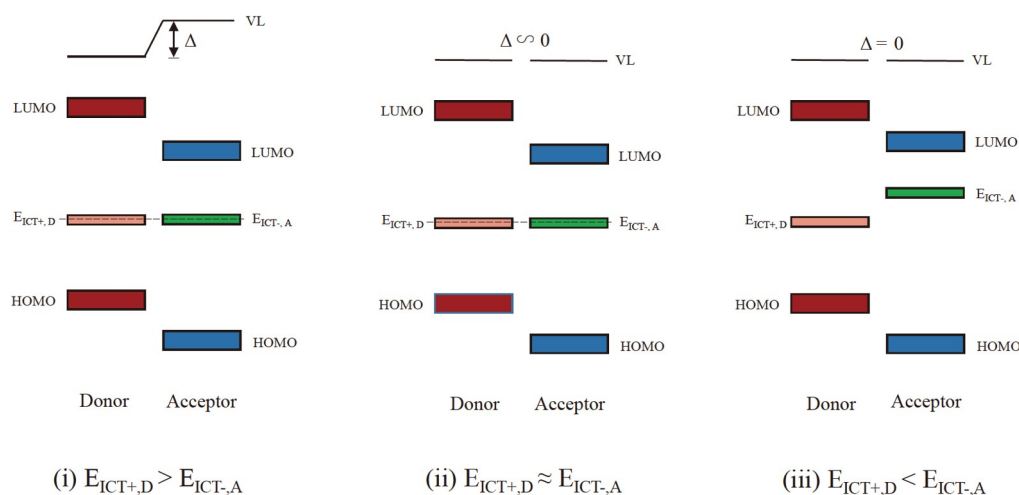
Figure 7 Three cases for the energy level alignment at D:A interfaces as ICT models: (i) $E_{ICT+, D} < E_{ICT-, A}$; (ii) $E_{ICT+, D} \approx E_{ICT-, A}$; (iii) $E_{ICT+, D} > E_{ICT-, A}$. Reproduced with permission from [69] (color online).
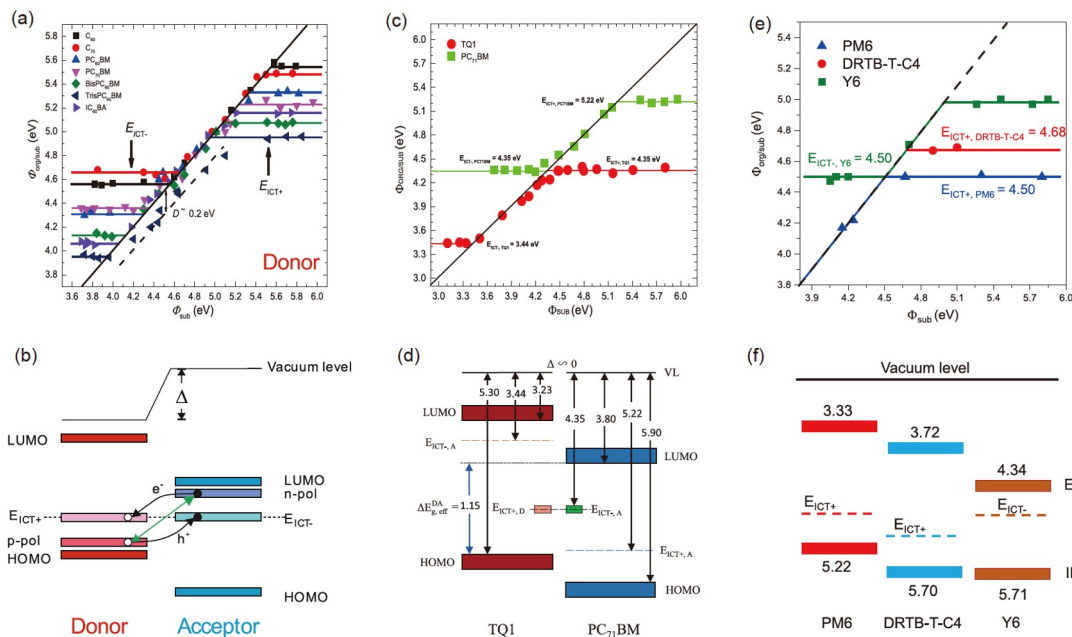
Figure 8   (a) ICT curves of a set of fullerenes. (b) Schematic illustration of the trap-assisted recombination *via* ICT states when $E_{\text{ICT}+, \text{D}} < E_{\text{ICT}-, \text{A}}$. (a, b) Reproduced with permission from [70]. (c) ICT curves of TQ1 and PC$_{71}$BM. (d) Energy level alignment at TQ1:PC$_{71}$BM interface. (c, d) Reproduced with permission from [69]. (e) ICT curves of PM6 and Y6. (f) Energy level alignment at PM6:Y6 interface (color online).

pinning energy for a molecular film may not remain same when it interacts with another polymer or especially small molecules, since the intermolecular order [72,73], crystal orientation and defects in crystalline film [74,75], as well as orbital hybridization [66] can possibly modify the energy level alignment, and even invalidate the ICT model.

The fundamental principle of electrode design can be proposed: the anode and cathode contact should pin the Fermi level to $E_{\text{ICT}+, \text{D}}$ and $E_{\text{ICT}-, \text{A}}$ on each side of the active layer; the ITO/PEDOT:PSS anode with a high WF (>5.1 eV) usually needs no additional treatment, but many studies on reducing the WF of the ITO/ZnO cathode in inverted device are reported [76–80]. For the same reason, some strong WF modifiers, such as conjugated electrolyte PFN-Br, are widely employed to realize Fermi level pinning at the metal contact [81–83]. Although the ICT model provides the basic requirement for the electrode WF, the local concentration of D: A blend near the interface can change the interfacial energetics [84,85]. Therefore, the detailed investigation on a new electrode interface is still necessary beyond just prediction in OSCs.

3.2   Energy loss in OSCs

The current state-of-the-art OSCs have external quantum efficiencies (EQEs) about 90% and fill factor (FF) over 80% [86–88]. Moreover, V_{OC} of OSCs is still considerably limited, compared with that predicted by the Shockley-Queisser (SQ) theory [89,90]. The main reason for the limited V_{OC} in

OSCs was initially ascribed to the high energetic difference (ΔE_{ct}) [91,92] between the singlet excited state (S1) of the donor or the acceptor materials and the charge transfer (CT) state [93,94] formed at the donor/acceptor interface, leading to relaxation of the excited state, causing significant voltage loss (V_{loss}) in OSCs, Previously, for fullerene OSCs, high ΔE_{ct} (>0.3 eV) was required for achieving efficient dissociation of excitons and realizing high photocurrent in OSCs. However, with the development of NFA based OSCs, efficient excitons dissociation can now be realized despite $\Delta E_{\text{ct}} < 0.1$ eV [95].Therefore, ΔE_{ct}s in current highly efficient NFA-OSCs are generally very small, playing a much less pivotal role in limiting V_{OC} of OSCs.

The reduction of V_{loss} in the OSCs using NFAs is generally over 0.5 V [96,97], considerably higher than that of high-efficiency inorganic or perovskite solar cells (<0.4 V) [98]. This is primarily due to the high non-radiative voltage loss (V_{nr}), a result of low electroluminescence external quantum efficiency (EQE$_{\text{EL}}$). The low EQE$_{\text{EL}}$ in OSCs could be associated with poor electronic contacts between the active layer and the electrodes, giving rise to significant surface recombination loss of charge carriers [99–101]. Therefore, interlayer engineering [99,102,103], for an improved electronic property at the active layer/electrode interface, has been playing an important role in reducing V_{nr} and improving V_{OC} of OSCs.

The electronic properties of CT states formed at the interface between the donor and the acceptor molecules in the active layer are also critically important in determining V_{nr} in

OSCs [93,94], because decay of photogenerated charge carriers occurs *via* the transition from the CT state to the ground state in OSCs [104]. Therefore, V_{nr} or EQE$_{EL}$ in OSCs is often expressed as a function of the decay rate of CT state [104], which is inversely proportional to CT state lifetime:

$$V_{nr} = -kT / q \ln(EQE_{EL})$$

$$EQE_{EL} = k_r / (k_r + k_{nr})$$

where k is the Boltzmann constant, q is the elementary charge, T is temperature, and k_r and k_{nr} are the radiative and non-radiative decay rates of CT state.

Increasing EQE$_{EL}$ for reduced V_{nr} has been proven to be highly challenging. Recently, it was demonstrated that reducing ΔE_{ct} of the donor-acceptor systems could lead to increased EQE$_{EL}$, allowing to achieve very low V_{nr} (<0.2 eV) in OSCs [95]. This made the low ΔE_{ct} blend systems particularly promising for achieving high efficiency solar cells. However, many of the solar cells based on low ΔE_{ct} systems suffer from inefficient exciton dissociation. Thus, a ternary blend strategy was proposed to fine tune ΔE_{ct} and to balance V_{nr} and quantum efficiency loss in OSCs, allowing the realization of V_{nr} as low as <0.15 V for OSCs with high quantum efficiency [105]. However, it was later suggested that the increased EQE$_{EL}$ achieved in the low ΔE_{ct} systems was related to increased k_r [106], a result of strong hybridization of the S1 state and CT state in blends, increasing the oscillator strength for the CT to ground state transition. Therefore, this method is expected to lead to increased radiative recombination voltage loss (V_r), which is logarithmically dependent on k_r, and thus has limited impact on the overall V_{loss} of OSCs. Besides, the high k_r could also lead to reduced FF, further limiting the performance of OSCs.

Therefore, to improve the performance of OSCs and to achieve reduction in both V_{nr} and V_{loss}, k_{nr} need to be reduced. This is difficult due to the presence of high-frequency vibrational modes in organic materials [98,107], giving rise to strong electronic coupling between the CT state and the ground state, and thus, the high k_{nr} in organic blends. Recently, it has been demonstrated that increasing the energy of CT states (E_{ct}) could lead to a reduced vibrational coupling between the states, thereby, reducing k_{nr}, and increasing EQE$_{EL}$. Nevertheless, for harvesting light of solar cells, it is undesired to use high E_{ct} material systems, since the narrow absorption spectrum, associated with the high E_{ct} systems, limits the photocurrent generation in the device.

To understand the impact of additional CT-state-related parameters, a numerical recombination model was developed [107].The roles of the reorganization energies, transition oscillator strength, static dipole moments, as well as the energy of CT states and the density of CT complex played a role in determining the V_{nr}, and the overall V_{loss} were systematically studied in theory. A number of strategies to re-

duce V_{nr} in OSCs were proposed, and reducing reorganization energies and increasing the static dipole moment of CT states were predicted to be the most effective. However, it is still unclear how one could achieve the reduced reorganization energies or increased dipole moment in organic blends. Thus, an effective experimental strategy to reduce k_{nr} and to achieve reduced V_{nr} and V_{loss} in OSCs is yet to be developed.

4 Flexible organic solar cells

Flexible OSCs nowadays have attracted enormous attention due to their excellent mechanical robustness, high power conversion efficiency, and potential applications in wearable and self-powered electronics [108–113]. With the rapid development of photoactive layers, PCEs of flexible OSCs have reached about 16% in the last few years [114]. The PCE improvement of flexible OSCs is summarized in Figure 9. The typical flexible device consists of a flexible substrate, two electrodes, a photoactive layer, and two buffer layers. Extensive efforts on these functional layers have been devoted to improving the performance of flexible OSCs, including developing flexible transparent electrodes [115], new organic photoactive semiconductors [116], and low-temperature processed [117] and mechanically robust interfaces [118]. Every functional layer is crucial for efficient device performance and mechanical flexibility of flexible OSCs. In the following section, we provide an overview of the research progress on substrates, electrodes, interfacial layers, and photoactive layers in flexible OSCs.

4.1 Substrates

The flexible substrates play an important role in realizing high-performance and mechanically stable flexible OSCs. Several characteristics of flexible substrates are critical for efficient flexible devices. (1) Optical properties: higher
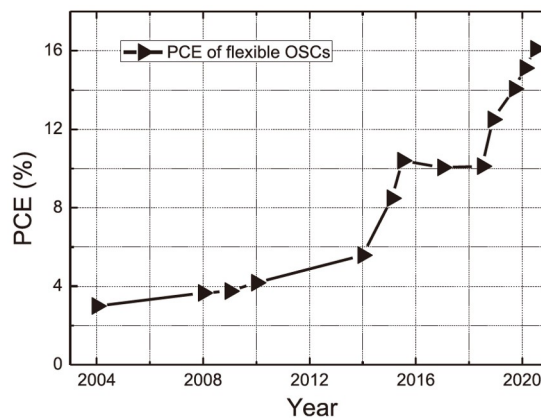

**Figure 9** Summary of PCE development of the flexible OSCs.

transparency represents more incident light into the active layer. (2) Mechanical properties: flexible substrates should hold their original functions after severe stress and strain. (3) Thermal properties: the thermal properties of flexible substrates would limit the highest preparing temperature. (4) Surface roughness: low surface roughness avoids electrical short-circuiting in the device.

Artificially synthetic polymers such as polyethylene terephthalate (PET) [119,120], polyethylene naphthalate (PEN) [121], polyethersulfone (PES) [122,123], and polyimide (PI) [124,125] are the most used substrates in flexible OSCs. PET and PEN have advantages of high transparency, low-cost, favorable bendability, and resistance to solvents [126]. PET is the most accessible flexible substrate. However, their low glass transition temperature (T_g) makes the temperature of the whole fabrication process no more than 150 °C, strongly limiting their applications. The PET substrates will deform during high-temperature treatment and the electrodes on the substrates will be destroyed at the same time (Figure 10a, b) [127]. Compared with PET and PEN substrates, PES is optically clearer and has higher T_g (223 °C) [128]. However, high cost and poor solvent resistance limit its practical applications [129]. PI exhibits excellent thermal stability among these substrates, which could tolerate a temperature of more than 300 °C. Moreover, PI as a substrate can block light of 350 nm wavelength in the UV range, which could increase the illumination stability of OSCs [130]. However, yellow color and high water absorption of PI are unbeneficial to the OSCs [131]. All polymer substrates have a relatively higher water vapor transmission rate (WVTR) or oxygen transmission rate (OTR), which would lead to the poor long-term stability of devices. Table 1 compares the typical properties of flexible polymer substrates [132,133].

4.2   Flexible transparent electrode

Indium tin oxide (ITO) is a commonly employed transparent
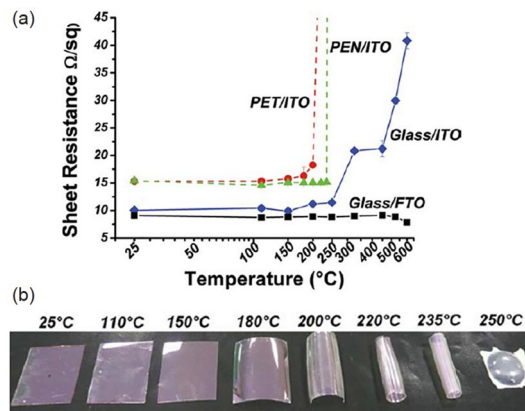
Figure 10   (a) Sheet resistance of ITO on different substrates after undergoing a thermal treatment at different temperatures for 30 min. (b) Image of PET/ITO substrates after the thermal treatment at different temperatures [127] (color online).

conductor, which can offer high transmittance of ~90% with low sheet resistance (R_S) of 10–25 Ω/sq. The PCE of ITO-based rigid OSCs have exceeded 18%. However, ITO is brittle and prone to cracking, which limits its usage in high-performance flexible OSCs.

The efficiency of flexible OSCs highly depends on the flexible transparent electrodes (FTE) due to the different optoelectronic performance between the FTE and the common rigid glass/ITO electrode. FTEs with potential applications should have the following characteristics: (1) mass-production; (2) high transmittance and conductivity (σ); (3) high mechanical stability. Several emerging materials such as conductive polymers, metal meshes, carbon nanotubes (CNTs), graphene, and metal nanowires (Ag/Cu NWs) have been explored as the next-generation FTE materials to replace ITO. In the following section, we will review the recent reports on FTEs in the flexible OSCs and the performance of the corresponding devices. The performance of representative FTE and photovoltaic parameters of corre-

Table 1   Comparison of flexible substrates

Substrates	PET	PEN	PES	PI
Refractive index	1.66	1.5–1.75	1.66	1.7
Densty (g/cm^3)	1.40	1.36	1.37	1.43
T_g (°C)	78	123	223	>300
Melting temperature (°C)	115–258	270	–	250–452
Work temperature (°C)	−50–150	–	223	>400
Youngs modules (GPa)	2–4	5–6	2.2	2–3
Tensile strength (MPa)	55–75	200–275	83	150–230
Compression strength (MPa)	80	–	–	51
WVTR (g/(cm^2 day))	21	6.9	73	64
OTR (cm^3/(cm^2 day))	6	2	235	22
Water absorption (%)	0.4–0.6	0.3–0.4	–	1.3–3.0

sponding flexible OSCs are summarized in Table 2.

4.2.1 PET/ITO flexible electrodes

In the early stages of flexible OSCs development, conducting metal oxides (MO) films such as ITO films and aluminum-doped zinc oxide (AZO) films have been used as transparent electrodes. In 2008, Jen *et al.* [141] fabricated a polyethylene terephthalate (PET)/ITO-based flexible OSCs shows only slightly reduced PCE (3.3%) in comparison to that of glass/ITO-based rigid OSCs. However, the PET/ITO FTE will crack during thermal treatment and bending test due to the high crystallinity of ITO (Figure 11a) [142]. Chang *et al.* [134] used Zn and Sn to replace 30% In of ITO to synthesize amorphous $Zn_{0.3}In_{1.4}Sn_{0.3}O_3$ (a-ZITO), which could grow on polyester substrates to prepare the FTE (Figure 11b). In comparison to polycrystalline ITO film, a-ZITO microstructure shows grain-boundary-free and excellent adhesion characteristics, giving continuous and uniform morphology over several micrometers (Figure 11c). Thus, the a-ZITO-based electrode shows a higher transparency (>80%), a lower R_S (<20 Ω/sq), and good mechanical flexibility (bending radius of ~2.5 mm). As expected, the related flexible OSCs demonstrates to have an improved bending durability retaining 85% of its initial PCE after 10-time bending cycles at a radius of 5 mm.

Although the PET/ITO flexible electrode has been successfully used in the flexible OSCs, the sputtered electrode makes them less cost-effective due to the use of high vacuum equipment. The commercially available FTEs should be prepared in a non-vacuum environment under favorable thermochemical conditions to simultaneously reduce production costs and further improve optoelectronic and mechanical properties.

4.2.2 Conducting polymer FTE

Conducting polymers with solution-processing ability and intrinsic flexible nature, such as PEDOT, are attracting considerable attentions. Usually, the PEDOT is doped with PSS, and the negatively charged PSS allows PEDOT to be dispersed in an aqueous solution and simultaneously serves as the counterion for the positively charged PEDOT. However, the unfavorable conductivity (σ) of the resultant PEDOT:PSS film as low as 1 S/cm seriously limited its application as an FTE in flexible OSCs.

To increase the conductivity of PEDOT:PSS films, it was usually doped with organic molecules in aqueous PEDOT: PSS solution to enhance crystallization of PEDOT and post-treated with polar organic acid to tune the phase separation

Table 2 Summary of photovoltaic parameters of high-performance flexible OSCs based on different electrode

Electrode	*FoM*	Active layer	V_{OC} (V)	J_{SC} (mA/cm^2)	FF (%)	PCE (%)	Ref.
Arylite/a-ZITO	80	PTB7:PC$_{71}$BM	0.729	14.7	59.4	6.42	[134]
PET/PH1000	77	PM6:Y6:PC$_{71}$BM	0.828	23.57	72.03	14.06	[135]
PI@graphene	53	PM6:Y6	0.84	25.8	70	15.2	[125]
PET or PI/ MoOx/SWCNT/MoO$_x$	11	PTB7:PC$_{71}$BM	0.72	13.7	61	6.04	[136]
PET/ZnO/Cu(O)/ZnO	214	PTB7-Th:PC$_{71}$BM	0.78	16.52	57.91	7.5	[137]
PET/silver-mesh	>1,000	PTB7-Th:O6T-4F:PC$_{71}$BM	0.694	26.65	65.75	12.16	[138]
PET/AgNWs (FlexAgNEs)	442	PTB7-Th:O6T-4F:PC$_{71}$BM	0.699	26.99	69.7	13.15	[139]
PET/Em-Ag/AgNWs:AZO-SG	498	PBDB-T-2F:Y6	0.832	25.05	72.97	15.21	[140]
PI:PS spheres@ZnO@AgNWs	124	PM6:N3:PC$_{71}$BM	0.84	25.0	76.5	16.1	[114]
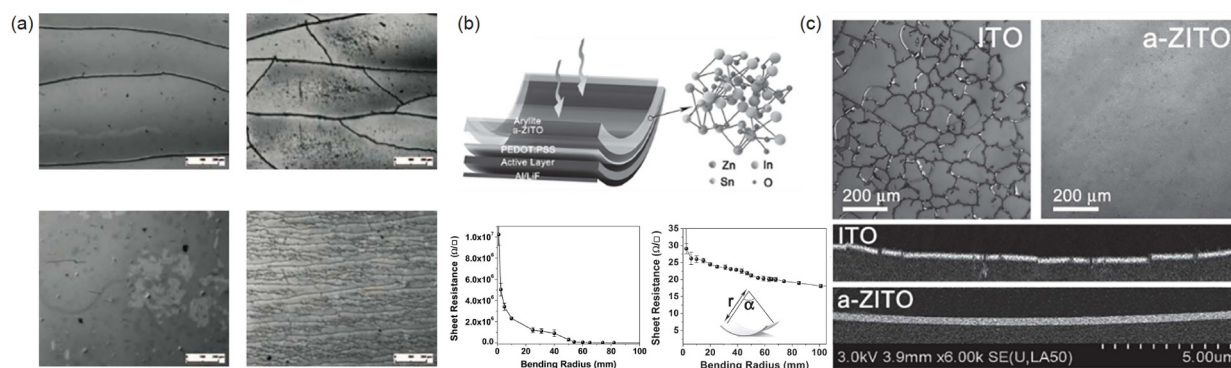
Figure 11 (a) Optical microscopy of the ITO layers on PET after annealing treatment [142]. (b) Device architecture of AryLite/a-ZITO-based flexible OSCs (top); R_S of AryLite/ITO and AryLite/a-ZITO electrodes with different bending radii (bottom). (c) Optical microscopic and SEM cross-sectional images of AryLite/ITO and AryLite/a-ZITO substrate [134] (color online).

between the PEDOT and PSS components (Figure 12a). Bao *et al.* [143] increase the conductivity of PEDOT:PSS film by 2–3 orders of magnitude by incorporating binary additives including dimethyl sulfoxide (DMSO) and fluorosurfactant Zonyl-FS300 (Zonyl). It was observed that the phase separation/morphology between PEDOT and PSS was fine-tuned, delivering a R_S of 46 Ω/sq at 82% of transmittance. The flexible OSCs based on this PEDOT:PSS shows a comparable PCE with that of the rigid device based on ITO electrode. Similarly, polar organic acid treatments are also demonstrated to enable tuning the phase separation for improving conductivity. The corrosive nature of acids, particularly for the strong acid, would easily make the plastic substrates deformed. Therefore, a series of milder acids were explored. Ge *et al.* [144] found that the methanesulfonic acid (CH_4SO_3) could effectively remove the hydrophilic PSS from PEDOT:PSS matrix on the PET substrate at room temperature and induce PEDOT assembly with favorable stacking. The resultant PET/PEDOT:PSS electrode simultaneously achieves high optical and electrical characteristics (average transmittance ≥ 90% in the range of 450–900 nm and σ = 2,860 S/cm), which promote PCE exceeding 10% for the related flexible OSCs that retained ~94% of its initial PCE after 1,000-cycle continuous bending tests (bending radius of 5.6 mm, Figure 12b). To avoid the corrosion of plastic substrates, the transfer-printing method was also employed to prepare PEDOT:PSS-based FTE with high conductivity (Figure 12c) [145]. Lee *et al.* [146] reported that the PEDOT:PSS film was treated with a strong acid H_2SO_4, and was then transferred to a PEN substrate to realize a high conductivity of 4,000 S/cm, high transmittance

(T>90% in the visible region) and robust bending durability (Figure 12d). However, some researchers found that the PEDOT:PSS with weak acidity may also lead to the device degradation during the storage. When the acid component PSS was removed to a certain extent by treating it with methanol or formic acid, the storage life time of the related device was effectively extended [147].

Although the PEDOT:PSS-based FTEs have been demonstrated to present substantial potential application in flexible OSCs, their parasitic absorption in the near-infrared (NIR) region leads to serious loss of light transmittance, which would significantly deteriorate PCEs. For example, when using the ternary active layer of PM6:Y6:PC_{71}BM with extended absorption spectrum close to 1,000 nm, the resultant flexible OSCs based on PET/methanesulfonic-acid-treated PEDOT:PSS showed a dramatically decreased J_{SC} compared with that of rigid glass/ITO-based device due to the mismatched transmittance of PEDOT:PSS and absorption of the electrode particularly in the NIR region [135]. Herein, it is necessary to further optimize the transmittance of FTE for pursing high efficiency.

4.2.3 Carbon materials-based flexible transparent electrodes
(1) Graphene
Graphene is a long-range ordered hexagonal carbon structure with an ultra-flat surface morphology. Because of its excellent photoelectric properties, mechanical stability, chemical stability and thermal stability, it has been considered as a promising material to replace ITO in the preparation of FTE. There are several methods to produce graphene sheets
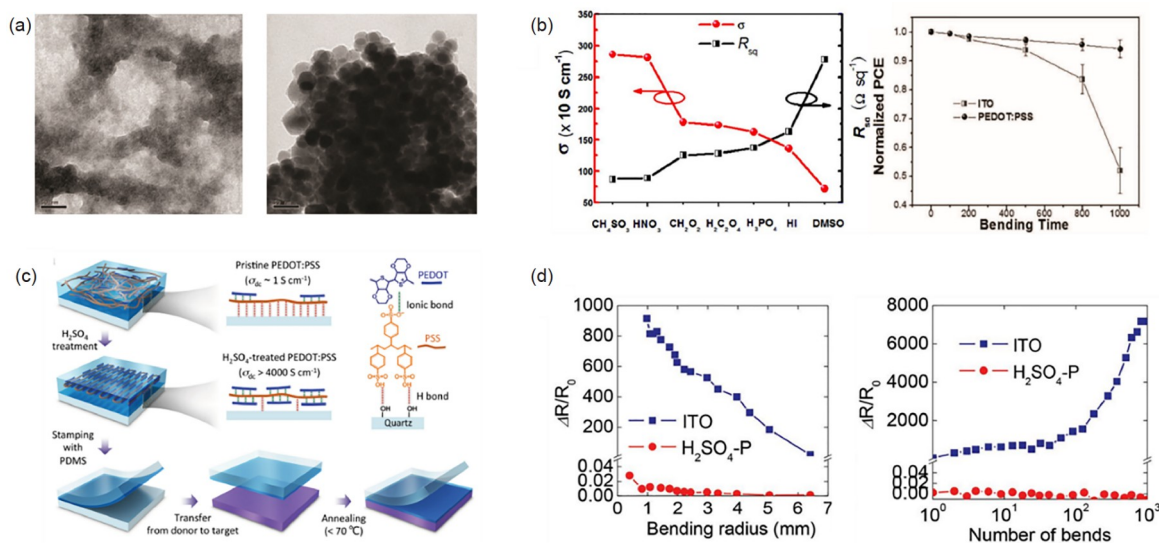
Figure 12 (a) TEM images of the pristine PEDOT:PSS films (left) and with acid treatments (right). (b) Comparison of square resistance and electrical conductivity of the PEDOT:PSS with different treatments (left); Normalized PCEs of flexible devices in bending test (right) [144]. (c) Transfer printing procedure of H_2SO_4-treated PEDOT:PSS film. (d) Resistance versus bending radius for H_2SO_4-treated PEDOT:PSS and ITO films on 125 μm-thick PEN substrates (left); Increase in resistance of the H_2SO_4-treated PEDOT:PSS and ITO films as a function of the number of bending cycles at a bending radius of 4 mm (right) [145] (color online).

such as chemical vapor deposition (CVD), mechanical exfoliation, epitaxial growth on SiC, chemical and liquid exfoliation. Among these techniques, CVD-graphene presents more potential for fabricating FTEs toward large scale and high conductivity. Unfortunately, it seems to be impossible to directly grow CVD graphene on a plastic substrate due to the extremely high growth temperature. Up to now, the graphene-based FTEs are typically fabricated with the following two strategy: (1) the synthesis of graphene on a catalytic metal substrate by CVD; (2) transfer the grown graphene to a target flexible-substrate using a supporting membrane such as polymethyl methacrylate (PMMA). However, the graphene and substrate cannot maintain intimate contact under mechanical stress due to the week van der Waals interaction between them. Moreover, the graphene films usually exhibit higher R_S due to defects in crystals and wrinkles during the transfer, which is the biggest obstacle for its application in FTEs. To address this issue, chemical doping and multilayer stack approaches are explored to improve conductivity. Kong *et al.* [148] modified the graphene with parylene as an interface layer by a hot rolling process, and the parylene can not only enhance the adhesion to graphene making less damage during the transfer, but also enables to improve its conductivity by doping graphene through Cl-containing parylene. The obtained PET/EVA/parylene/two-stack graphene electrode showed a R_S below 300 Ω/sq and a transmittance over 90%, and the related flexible OSCs showed an even comparable PCE to that of PET/ITO-based device. Moreover, Park *et al.* [125] directly integrated PI on graphene (Figure 13a) for assisting graphene growth. The PI-assisted graphene (PI@-graphene) electrode exhibits an ultra-clean surface together with a highest transmittance exceeding 92% and a R_S of

83 Ω/sq (Figure 13b). In addition, this electrode well maintains the high flexibility and thermal stability of PI film and graphene, contributing to a high-performance flexible OSCs with a PCE of 15.2% and robust flexibility with retaining over 90% of the initial PCE after 1,000-bending cycles at a radius of 2 mm. This is also the highest reported PCE so far for flexible OSCs based on graphene electrodes.

(2) Carbon nanotubes

Carbon nanotubes (CNTs) are also one of the most promising carbon materials for their application in electronic devices owing to their fine-tuned electrical properties such as bandgaps and conductivities ranging from conductors to semiconductors. Single-wall carbon nanotubes (SWCNTs) are considered to be a good candidate for a FTE due to their high transparency over a broad range of wavelengths along with high conductivity. Chhowalla *et al.* [149] used solution-processed SWCNTs to replace ITO as the electrode to fabricate OSCs in 2005, and a comparable PCE with that of ITO-based control devices was achieved, because the 3D nature of the interface between the SWCNTs and the P3HT:PCBM nanocomposite is beneficial for charge carrier extraction. Later, Gruner *et al.* [150] utilized transfer-printing method to prepare SWCNTs on PET substrate, and the resultant FTE shows a transmittance of 85% at 550 nmand a R_S of 200 Ω/sq. The related flexible OSCs yield a PCE of 2.5%, and the device performance can be well maintained even after fold (inducing compressive or tensile strain). In 2005, Matsuo *et al.* [136] introduced a way to fabricate efficient and flexible CNT-based OSCs with the application of direct and dry deposited SWCNT films and demonstrated the dual functionality of thermally annealed MoO_x on SWCNTs as both FTE (MoO_x-doped SWCNTs) and electron-blocking layer (Figure 13c). The SWCNTs based OSCs exhibited a
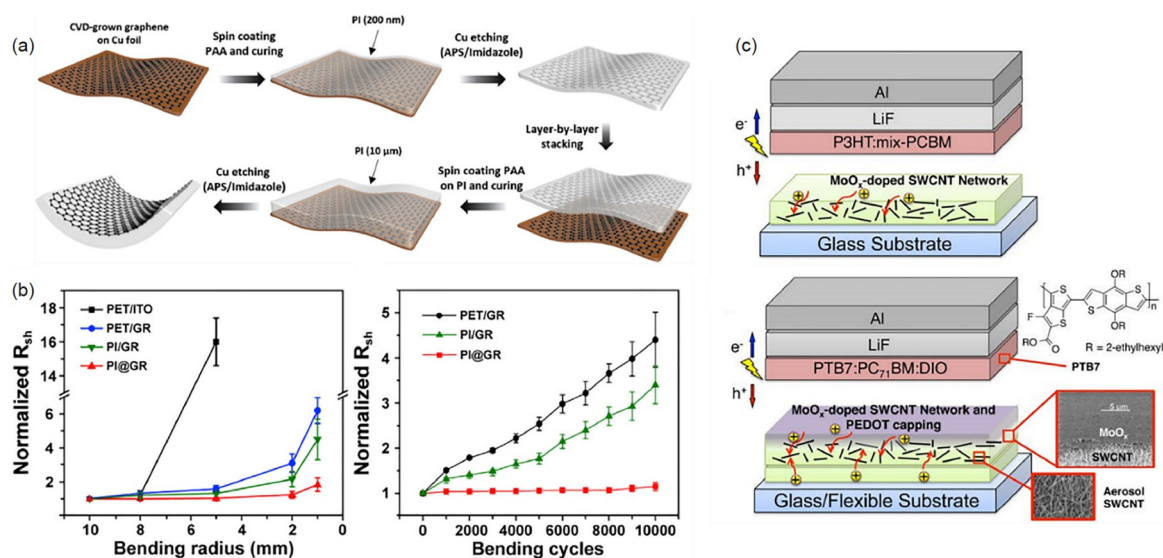
Figure 13 (a) Fabrication process of PI@graphene. (b) Normalized R_S of PET/ITO, PET/GR, PI/GR, and PI@GR at various bending radius after 1,000 cycles. (left); Normalized R_S of PET/GR, PI/GR, and PI@GR for various numbers of bending cycles with the radius of 5 mm.(right) [125]. (c) Device architecture with SWCNT-based electrode [149] (color online).

PCE of 6.04%, and retained its performance after 10 bending cycles with radius of 5 mm.

Although the grapheme- and CNTs-based FTEs have been successfully used in flexible OSCs, it seems that there is long way toward application. As for graphene, it's necessary to develop solution-processed graphene films with high uniform and conductivity on a large scale. The CNTs should relieve the trade-off between the transparency and the conductivity.

4.2.4   Metal based flexible transparent electrodes
(1) Ultrathin metal

Considering the high parasitic absorption of PEDOT:PSS-based electrodes and the complex fabrication process of carbon-material electrodes, metal (*i.e.*, Ag, Au, and Cu) with ultrathin thickness and microstructure attracted considerable attention as the potential alternatives to conventional ITO owing to their high conductivity and transparency in the wide range. Ultrathin metal films with the thickness of 10–25 nm, prepared by vacuum thermal evaporation, present excellent optoelectrical features and robust flexibility. However, the growth of the ultrathin metal follows the Volmer-Weber

nucleation mode, which is highly dependent on the substrate nature. The poor adhesion of the plastic substrate is unfavorable for nucleation and growth of the metal film, resulting in a noncontinuous film with discrete islands and random crevices. The rough morphology would decrease the optical transparency and conductivity [151]. Fortunately, this behavior can be mitigated by pre-depositing a layer of metal oxide on the substrate surface, where the nucleation of deposited metal could be homogeneous and metal atom diffusion rate is efficiently suppressed. Thus, recent research efforts to designing ultrathin metal electrode have been devoted to the oxide/metal/oxide (OMO) structures. Yun *et al*. [137] fabricate a continuous, smooth ultrathin copper *via* limited copper oxidation with a trace amount of oxygen (Figure 14a, b). They found that nanoscopic cluster migration could be substantially suppressed in weakly oxidized (Cu(O)) films at the very early stages during Cu growth due to obviously improved film wettability. As a result, the zinc oxide (ZnO)/Cu(O)/ZnO electrode exhibits an average transmittance of 83% (400–800 nm)and a R_s of 9 Ω/sq. A flexible OSC based on the OMO electrode achieved a promising PCE of 7.5%, outperforming the flexible OSC
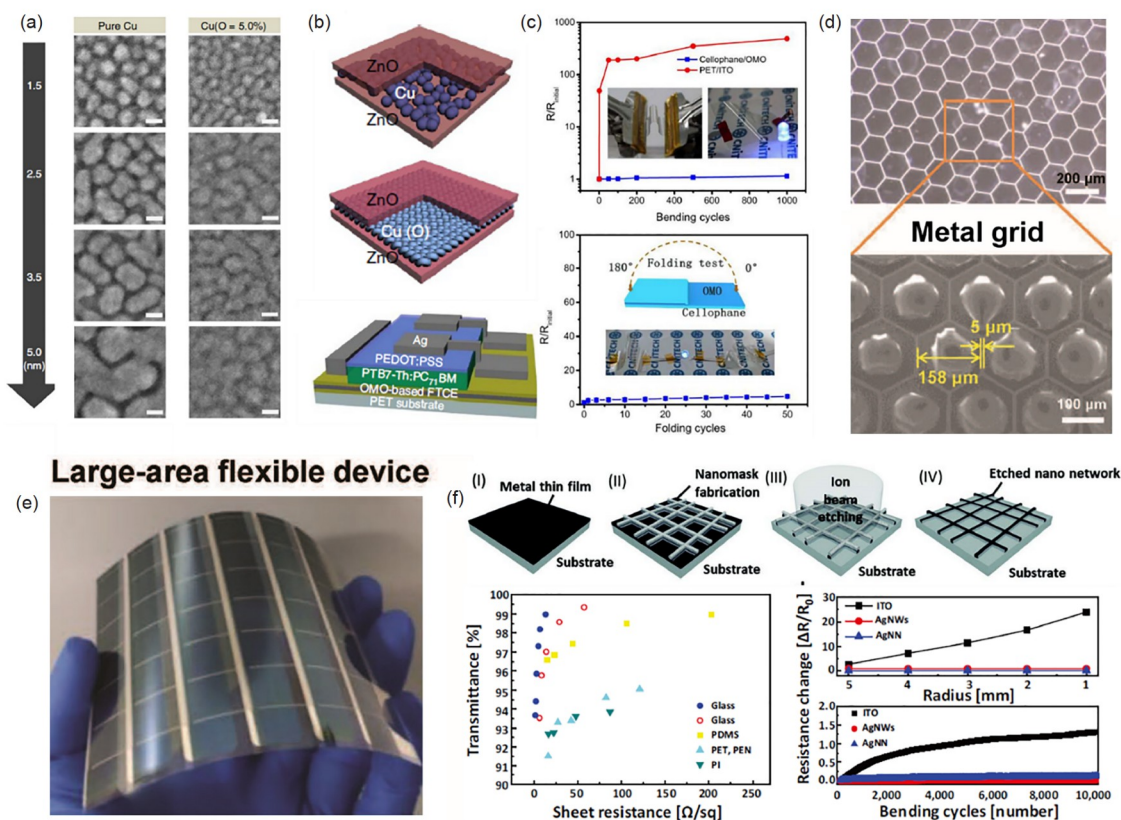
Figure 14   (a) The growth behavior of Cu and Cu (O=5.0%) clusters on ZnO films. Scale bar, 10 nm. (b) Schematic diagrams representing the different morphologies of Cu and Cu (O) films in an OMO configuration [137]. (c) Change in resistance of cellophane/OMO and PET/ITO as a function of bending cycle with radius of 1 mm (top); Change in resistance of OMO electrode as a function of folding cycle (bottom) [152]. (d) Optical microscopy and SEM images of the PET/Ag-mesh substrate. (e) The large area flexible device [138]. (f) Schematic illustration for the fabrication of monolithic, etched NNs using nanofiber networks as a mask (up); resistance change of different electrodes with decreasing bending radius and increasing bending cycles [121] (color online).

counterpart based on ITO electrode and showing a ~10% reduction in PCE even after bending at a radius of 1 mm. Similarly, Song *et al*. [152] deposited a ZnO/ultrathin Ag/ZnO on a 25-μm cellophane, showing a R_S of 7.2 Ω/sq and transmittance of 81.7% in 400–800 nmregion accompanied with excellent flexibility (Figure 14c). The resultant device exhibited a PCE of 5.94% and maintained 92% of the initial value after folding 35 cycles.

(2) Metal mesh

Metal meshes are usually fabricated on a plastic substrate by different printing techniques, such as gravure printing with an engraved plate, flexographic printing with a relief plate and inkjet printing, which can precisely control the microstructure of metal meshes to fine tune the optoelectronic properties including sheet resistance, transmittance. Li and Chen *et al*. [153] developed a high-resolution embedded Ag mesh pattern with 3-μm-wide and 2-μm-thick Ag mesh lines on PET substrate (Figure 14d). The Ag mesh/PET films with the Ag coverage of 4.3% displayed a low R_S of ~0.5 Ω/sq and high light transmittance of 85% (including PET substrate). However, the obtained high transmittance is attributed to the low surface coverage of Ag mesh, and the gaps between Ag meshes will cause parasitic lateral current flow. Thus, a hybrid electrode consisting of high-resolution Ag mesh and PH1000 film was fabricated on PET substrate sequentially, showing a fully coverage electrode with a low R_S of 1.2 Ω/sq. As expected, the average transmittance in the visible region decreased to 80% in comparison with the bare Ag-mesh-based FTE. However, the device still demonstrated a good PCE of 5.85%, which is much higher than that of the device based on PET/ITO electrode. This hybrid FTE could be also fabricated by roll-to-roll printing technology [154]. Wei *et al*. [138] demonstrated a large-area flexible OSC devices by further reducing the optical and electrical losses in the flexible substrate, and a promising PCE of 12.16% for the single-junction cell (1 cm^2) has been attained, which is very close to the PCE (12.37%) of the small area (0.04 cm^2)rigid device fabricated by spin coating process. This strategy could further promote the module areas of flexible OSCs as high as 25 and 50 cm^2 for achieving excellent PCEs around 10% (Figure 14e) by slot-die method. It suggests that the PET/Ag mesh electrode present a huge potential in the application of flexible organic solar cells even comparable with large-area printing technology. In addition, Ag-mesh-based FTE can be fabricated by various printing technologies. Someya *et al*. [155] utilize a reverse-offset printing process to print a uniform and ultrathin Ag mesh (thickness of 100 nm) on ultra-flexible substrates. By fine-tuning the space length of the mesh, a R_S of 17 Ω/sq and an average transmittance of 93.2% in the visible region was achieved which even surpassed the photoelectric properties of sputtered ITO electrodes. This ultrathin FTE also exhibits superior mechanical stability at a buckling structure, displaying

only 16.6% and 10.6% change in R_S under 50% compression and after 500 stretch/release strain cycles, respectively. The flexible OSCs based on this electrode could also contribute a PCE of 8.3%. Besides the printing technology, the metal mesh electrode with high optical transmittance and conductivity could be also fabricated by patterning the ultrathin metal. Lee *et al*. [121] explored a conductive silver nano networks (AgNN) on a flexible substrate by using a dry etching pre-deposited thin metal film where a randomly distributed nanofiber networks was selected as shadow masks (Figure 14f). The transmittances of monolithic nano-networks reach 94.4% accompanied with a R_S as low as 2.4 Ω/sq. This FTE was also found to have high thermal, environmental, and mechanical stabilities. As a result, based on this electrode, the flexible OSCs without using any buffer layer also achieve a high PCE, and the related device performance was almost not changed after 3,000-time bending cycles.

As above summary, the FTE based on metal mesh generally exhibits superior conductivity and transmittance compared with those of carbon and conducting polymer counterparts. However, the complex preparation process and high-standard equipment greatly increase the preparation costs. Therefore, how to prepare metal-based FTE by utilizing solution-processing method is more practical.

(3) Metal nanowires

Metal nanowires (NWs) were usually synthesized by the polyol reduction method. For example, AgNWs synthesized by the reduction of $AgNO_3$ with ethylene glycol in the presence of structure-directing agents and steric stabilizers such as polyvinylpyrrolidone (PVP). These provide superior advantages for fabricating FTE, including solution processability, high transparency, excellent conductivity and stability. Cui *et al*. [156] prepared FTEs consisting of random-distributed AgNWs by solution process. The resultant FTE showed comparable transmittance in visible region with metal-oxide thin films under the same R_S, where a solar photon flux-weighted transmissivity (T_{Solar}) reached 85% accompanied with a R_S of 10 Ω/sq. In addition, the bending test has a slight influence on the R_S of FTE at a radius of 4 mm.However, the PVP ligands are hard to be removed, and their insulating properties would create high contact resistance at the NW/NW junctions, making it difficult to obtain high conductivity at a low content of metal NWs. Duan *et al*. [157] proposed a rapid electrochemical cleaning strategy to thoroughly remove the surface PVP ligands, and the conducting properties of the AgNWs thin films was efficiently enhanced, delivering a reduced R_S from 49 to 13 Ω/sqwith a 90.91% transmittance at 550 nm.Besides, the AgNWs-based FTEs usually present relatively rough surface, which is unfavorable for the deposition of subsequent active layer. For example, the AgNW networks can easily penetrate the 100-nm-thick active layer, resulting in the

short-circuit and poor performance. To overcome this problem, a hybrid electrode was proposed by coating a buffer layer such as PEDOT:PSS or metal oxide on AgNWs. Lee *et al.* [158] employed AgNWs and ZnO by the solution-processing method to fabricat FTEs. The ZnO coated on AgNWs film showed a R_S of 10 Ω/sq, and a transmittance of 82% at 550 nm.The resultant flexible OSCs exhibit a comparable PCEs with that of rigid glass/ITO-based devices. Mixing AgNWs with conducting polymer PH1000 is another efficient way to adjust the surface morphology and conductivity of the electrode, but the transmittance would be reduced due to the high parasitic absorption of PH1000. Li *et al.* [159] found that when blending PH1000 with AgNWs, the content of PH1000 could be significantly reduced while simultaneously realizing low R_S of 6 Ω/sq, high transmittance (86% at 550 nm)and smooth surface. Recently, a biomimetic electrode based on AgNWs was proposed by using the contact film transfer technique to mimic the internal anatomy of the leaf [114]. By bottom-top solution-processing conductive AgNWs, transparent ZnO protecting layer, light-scattering polystyrene (PS) spheres, and ultrathin flexible PI substrate. The resultant electrode with smooth surface topology (root mean square (RMS) ~2.4 nm), low R_S (23.4 Ω/sq) and high transparency (88.2%) with haze over 43% was simultaneously realized. The high haze is beneficial for the effective scattering of the incident light, which could increase the light utilization. Finally, the optimized

flexible OSC with this electrode exhibited a record PCE of 16.1% at the published time, and 85% of its initial PCE was retained even after 5,000 bending cycles at a bending radius of 1.0 mm (Figure 15c, d).

Moreover, the conductivity of the AgNWs films is highly dependent on AgNWs' distribution and connection. To improve the conductivity, external treatments such as thermal annealing, selective growth of silver nanoparticles at the NW-NW junction, joule heating, cold isostatic pressing, capillary force effect, electroless-welding AgNWs networks and hybrid AgNWs with other functional materials were carried out. Among them, thermal treatments easily make the plastic substrate distort due to the low glass transition temperature of plastic substrate. Seo *et al.* [115] developed a cold isostatic pressing (CIP) method that enabled intimate contact between AgNWs, which could reduce R_S from 49.3 to 20.7 Ω/sq and simultaneously possess an excellent transmittance of 94.8% at 550 nmwavelength. The CIP electrode has a lower resistance than that of the annealed AgNWs because the low temperature processing could suppress oxidation of surface AgNWs. Besides, CIP treated AgNWs electrode shows a lower surface roughness, which can reduce the occurrence of short circuit and obtain higher device reproducibility. Recently, Li *et al.* [140] proposed a "welding" concept to design an FTE by tightly binding the upper electrode and the underlying substrate with embedded AgNWs (Em-Ag) (Figure 15e–g), where the upper electrode
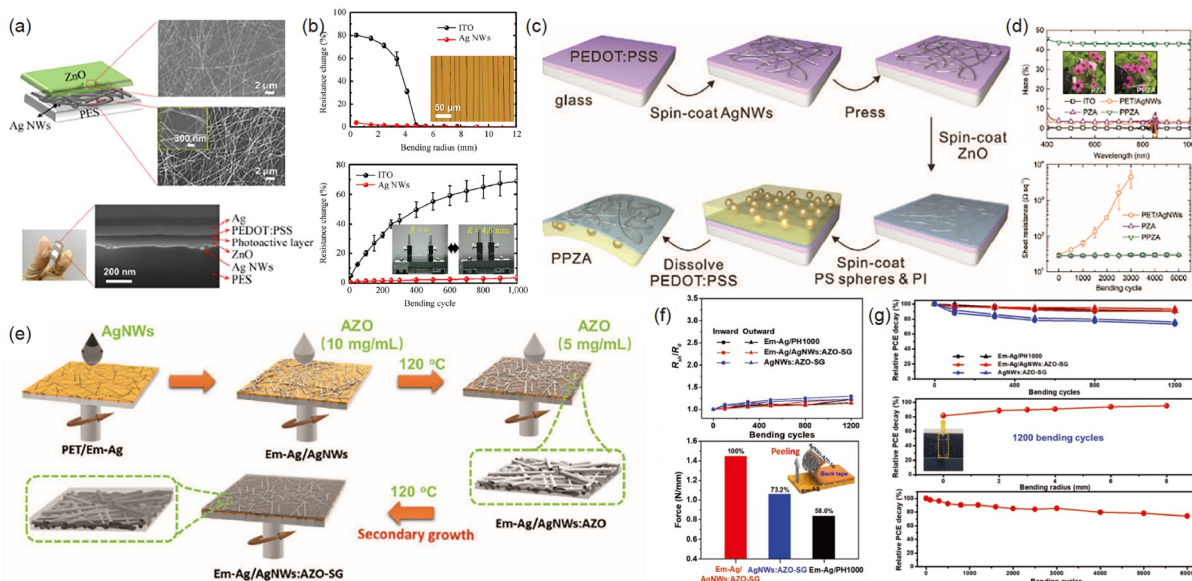
Figure 15 (a) SEM image of an AgNW electrode and a ZnO buffer layer on the AgNW films (top); photograph of PES/AgNW film-based flexible OSCs and SEM image of a fabricated device (bottom). (b) Changes in the resistances of the electrodes based on the flexible PES/AgNWs and PES/ITO films as a function of the bending radius. Inset: optical image of the electrode based on the PES/ITO film after being bent with a radius of ~4 mm (top) and change in resistance as a function of the number of bending cycles with the bending radius of ~4.8 mm (bottom) [160]. (c) Schematic of the fabrication of the biomimetic electrode. (d) Haze spectra (top); resistance evolutions as functions of the number of bending cycles (bottom) [114]. (e) Schematic diagram of Em-Ag/AgNWs:AZO-SG electrode fabrication. (f) R_S change of various FTEs with increasing bending cycles (top); the adhesive force values of various FTEs (bottom). Inset: schematic illustration of adhesive force measurements. (g) PCE evolution of flexible OSCs for those based on different FTEs versus bending cycles at a radius of 4 mm (top); Em-Ag/AgNWs:AZO-SG FTE versus bending radius after 1,200 bending cycles in the inward direction (middle); Em-Ag/AgNWs:AZO-SG FTE *versus* bending cycles at a radius of 4 mmin the inward direction (bottom) [140] (color online).

consisting of solution-processed Al-doped ZnO (AZO) and AgNWs network is well welded by utilizing the capillary force effect and secondary growth of AZO (AZO-SG). The welding FTE exhibits a reduction of the AgNWs junction site resistance at relatively low temperature, which helps the R_S decrease to ~18 Ω/sq accompanied with the highest transmittance of ~95% at 550 nmeven extending to the near-infrared region. The flexible OSCs based on this FTE exhibit a record PCE of 15.21%, showing a consistent J_{SC} value with the device based on glass/ITO electrode. Moreover, the flexible OSCs could retain 75% of their initial PCE values after 6,000 bending cycles at a bending radius of 4 mm and 81.7% after the device was completely folded. This enhancement in flexibility is ascribed to the increased adhesion between the electrode and the substrate by the "welding" strategy. Chen *et al.* [139] blended a polyelectrolyte poly (sodium 4-styrenesulfonate) (PSSNa) with water-processed AgNWs, where the PSSNa anions with ion electrostatic charge repulsion preferentially adsorbed on AgNWs. The weak repulsion force is conductive to stabilizing AgNWs in aqueous solution without aggregation. Importantly, this PSSNa-assisted AgNWs could directly deposit on a flexible substrate to fabricate FTEs (FlexAgNEs) with mesh-like patterns and high smoothness. As a result, FlexAgNEs shows a R_S as low as 10 Ω/sq and around 92% transmittance at 550 nm,and these excellent performance enables to fabricate flexible tandem OSCs with high efficiency and robust mechanical stability.

Generally, there is a trade-off between the transparency and the conductivity for FTEs, which makes the FTE hard to achieve high transmittance and high conductivity at the same time. To balance them for the potential application of FTE in flexible OSCs, a quantitative standard by calculating the figure of merit (*FoM*) was proposed according to the following equation:

$$T = \left(1 + \frac{Z_0 \sigma_{op}(\lambda)}{2R_s \sigma_{d.c.}}\right)^{-2} \quad (1)$$

where Z_0 is the impedance of free space (Z_0 = 377 Ω), $\sigma_{d.c.}$ and $\sigma_{op}(\lambda)$ are the direct current and optical conductivities of the materials, respectively. The value of $\sigma_{d.c.}/\sigma_{op}(\lambda)$ is defined as being the *FoM* that is used to evaluate the performance of FTE. The transmittance (*T*) of the FTE was measured at a wavelength of 550 nm.The *FoM* values of the electrodes as mentioned above were listed in Table 2.

After several years of the development, FTEs for flexible OSCs have achieved fruitful results. However, during the OSCs developed towards commercial application, traditional electrodes with unfavorable opto-electrical properties seriously prevent this proceeding. As shown in Figure 16, metal oxide and conducting polymers based FTEs still suffer lower *FoM* values; conducting polymers such as PEDOT:PSS exhibit extremely strong water absorbing capacity and inherent
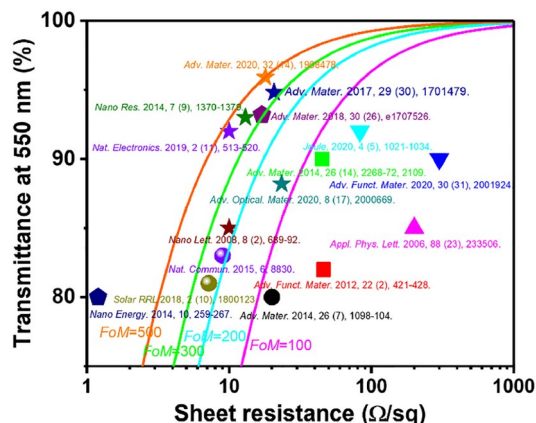
Figure 16 Transmittance and R_S of different types of flexible transparent electrodes: Metal oxide (circle); PEDOT:PSS (square); graphene (down triangle); CNTs (up triangle); OMO (sphere); metal mesh (pentagon); NWs (star). Curves with different FOM values are indicated by different colored lines (color online).

parasitic absorption in the long-wavelength region; the preparation of ultra-thin metals needs the high vacuum environment; the complex preparation process and low *FoM* of carbon materials make them impossible to produce flexible and transparent electrodes with stable performance on a large scale. In comparison, the FTEs based on metal meshes and NWs seem to be the best choice for future applications in flexible OSCs. As for metal-mesh-based FTE, the geometry of the metal mesh should be further precisely controlled to obtain high transmittance, conductivity and smooth surface by using cheap technology. As for AgNWs-based FTEs, how to reduce contact resistance between NWs and increase the reproducibility in large scale by solution process is highly desirable. Meanwhile, the synthesis of high-quality AgNW ink with weak aggregation, high stability, no ligand and suitable viscosity is necessary for future commercial application using printing technology.

4.3 Interfacial layers

Requirements are more stringent for interfacial layers in flexible OSCs compared with those in rigid devices. Low-temperature processing to avoid the destruction of flexible polymer substrates (PET, for instance) and good mechanical flexibility are desired in efficient flexible OSCs.

As for the electron-transporting layer, low-temperature-processed metal oxides have been widely used in flexible OSCs. Chen's group [139] successfully employed room-temperature-processed ZnO nanoparticles to fill the AgNW network. A well-coverage AgNWs:ZnO was realized and the flexible single-junction and tandem devices achieved PCE of 13.1% and 16.5%, respectively. Moreover, Li's group [140] fabricated flexible OSCs on the electrodes by combining the embedded AgNWs substrate and AgNWs:AZO. The AZO

was annealed at the temperature of 120 °C. Their single-junction flexible OSCs show a high PCE of 15.21%. Though ZnO works well in many flexible OSCs, it is essentially brittle and tends to crack especially under high strain which is detrimental to the mechanical robustness of the flexible OSCs [161,162].

Mechanical flexibility is important for interfacial layers to achieve good deformation cycling durability. Polymer interfacial layers stand out due to their naturally excellent flexibility. PEIE as a low-work function interfacial layer, which could be processed at room temperature, has been widely applied in fullerene-based OSCs [102]. Jiang *et al.* [161] employed a polymer of polyethylenimine ethoxylated (PEIE) on Ag mesh/PEDOT:PSS stacks. Their ultrathin OSC on Ag mesh/PEDOT:PSS/PEI showed much better flexibility than the device on Ag mesh/ZnO (Figure 17a–c). Though PEIE demonstrates excellent mechanical robustness, it is prone to react with non-fullerene acceptors, which would destroy the chemical and electronic structure of acceptors [163,164]. Zhou's group [165] introduced a strategy of increasing the protonation of PEIE to produce flexible OSCs. The PEIE showed more protonated N^+ processed from an aqueous solution, which could work efficiently for non-fullerene active layers. They achieved a flexible OSC with a PCE of 12.5%. But the thickness of these polymer surface modifiers like PEIE is required to be less than 10 nm due to their insulating nature. Zhou's group [166] further introduced zinc ions to chelate with PEI to increase its conductivity and chemical stability. The new interfacial material was donated as PEI-Zn. PEI-Zn showed thickness-insensitive properties, which could be thick up to 100 nm.

Meanwhile, PEI-Zn inherits the good flexibility of PEIE. Cracks can be observed for the ZnO film after 500 times continuous bending with a bending radius of 4 mm. While no crack appeared on the surface of the PEI-Zn film after the same bending conditions (Figure 17d–f). Furthermore, Zhou *et al.* [167] demonstrated large-area flexible organic modules showing the efficiency of 13% based on the Ag grid/AgNWs/PEI-Zn transparent electrode. The polymer-based PEI-Zn shows promising applications in printed electronics and flexible electronics.

Conducting polymer PEDOT:PSS can work well as electrodes and the hole-transporting layer in OSCs. PEDOT:PSS is an ideal material for interfacial layers in flexible OSCs due to their high flexibility, high electrical conductivity, low-temperature production, and tunable work functions [168]. PEDOT:PSS AI 4083 (a formulation of PEDOT:PSS) is generally employed as hole-transport layers. It can collaborate with several flexible electrodes, such as AgNWs, graphene, and PEDOT:PSS. Fan's group [169] deposited AI 4083 on perchloric acid ($HClO_4$)-treated PEDOT:PSS electrodes, achieving flexible OSCs with over 16% PCE. On rough surfaces such as AgNWs and graphene, a layer of highly conductive PEDOT:PSS (PH1000) is often needed to smooth the surface. Ge's group [170] employed PH1000 to flatten the surface of graphene & AgNWs electrodes. An extra layer of AI4083 was used as the hole-transporting layer. Their flexible OSC demonstrated a PCE of 13.4%. But there is a drawback of PEDOT:PSS that is low transmittance in the spectral region over 600 nm, which will reduce the J_{SC} of OSCs. This drawback will be further expanded when the PEDOT:PSS films become thick.
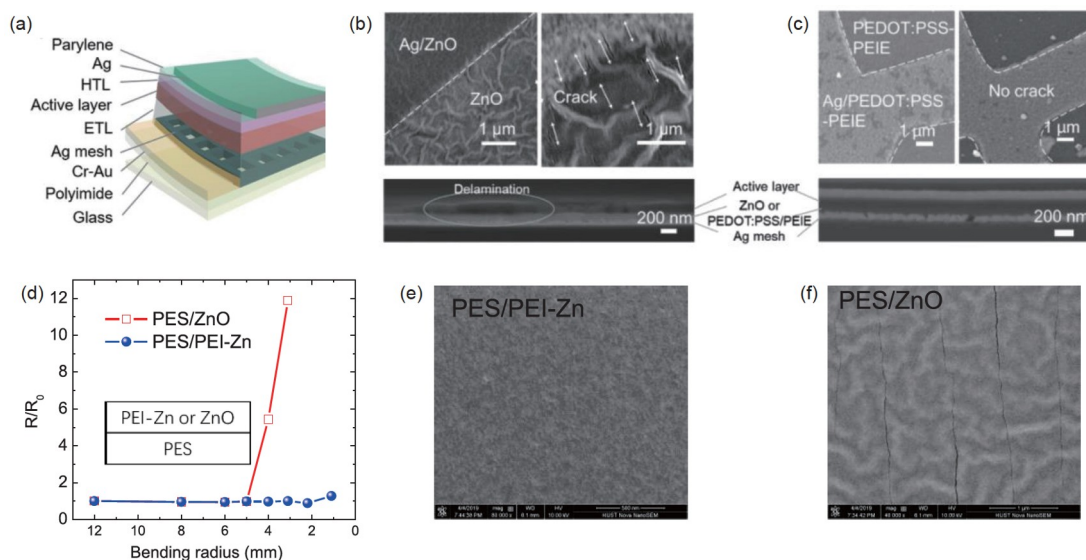
Figure 17 (a) Structure of flexible OSCs. (b) Top-view (top) and cross-section (bottom) SEM images of Ag mesh/ZnO stacks. Ag mesh/ZnO before (top left) and after (top right) peeling off are measured. Cracks are formed after peeling off. (c) Top-view (top) and cross-section (bottom) SEM images of Ag mesh/PEDOT:PSS/PEIE stacks [161]. (d) The changes of the resistance of the PES/ZnO and PES/PEI-Zn films under different bending radius. (e, f) SEM images of the PEI-Zn and ZnO films on PES substrates (PES/PEI-Zn and PES/ZnO) after 500 times continuous bending with a bending radius of 4 mm. Cracks appeared on the surface of ZnO films [166] (color online).

4.4 Photoactive materials

To date, the most efficient OSCs have been fabricated with polymer donors and small-molecule acceptors. Despite the high PCEs, the small molecular acceptors have relatively poor flexibility due to their brittle crystalline features [171]. To improve the flexibility of the OSCs based on small molecules, Han *et al*. [172] introduced insulating poly(aryl ether) (PAE) resins into the PM6/Y6 binary system. The devices with 30 wt% PAE retain the PCE of 15.17% and exhibit enhanced 4.4-fold elongation at break (25.07%) than those without PAE, showing impressive flexibility. After bending at a radius of 10 mmfor 100 times, the flexible cells with PAE remained unchanged, while the active layer without PAE had distinct cracks on the film surface (Figure 18a–c). Though fullerene-based acceptors are considered to be unfavorable on mechanical properties, Huang *et al*. [173] found that the addition of a proper amount of $PC_{71}BM$ molecules slightly disrupted the crystallization of IEICO-4F. The added $PC_{71}BM$ was located in the amorphous region and made the blend morphology with amorphous regions, which improved film ductility and flexibility.

All-polymer solar cells based on polymer semiconductors as both donors and acceptors have unique advantages over the small molecule acceptors-based OSCs in mechanical durability [174]. Kim's group reported that the all-polymer active layer demonstrated significantly enhanced flexibility compared with polymer/PCBM devices [175]. The all-polymer layer exhibited maximum extensibility of 7.2% and tensile modulus of 0.43 GPa,which were 60- and 470-fold increase than the polymer/PCBM films, respectively (Figure 18d, e). To further improve the mechanical properties of all-polymer solar cells, poly(dimethylsiloxane-co-methyl phenethylsiloxane) (PDPS) was added into poly(6-fluoro-2,3-bis-(3-octyloxyphenyl)quinoxaline-5,8-dyl-alt-thiophene-2,5-diyl) (TQ-F):N2200 all-PSC matrix to control the intercalation behavior and nanocrystallite size in the polymer-polymer blend by Chen and co-authors [176]. Samples with 10 wt% PDPS exhibited much improved mechanical durability with superior toughness values of up to 9.67 MJ/m^3 and elongation at a break of 50.92%. Their flexible devices on graphene electrodes showed a PCE of 5.60% and retained 90% of the initial PCE after bending 100 times with a bending radius of 3.0 mm. The chemical structure, molecular weight, dispersity, and thin-film morphology of active materials are all related to the mechanical properties [174]. Wang's group [177] developed polymer acceptors with different bridging atoms and achieved a flexible all-polymer solar cell with a PCE of 6.37%.

Though all-polymer active layers show excellent flexibility and stretchability, most of the flexible OSCs are still based on the nonfullerene small-molecule acceptors due to
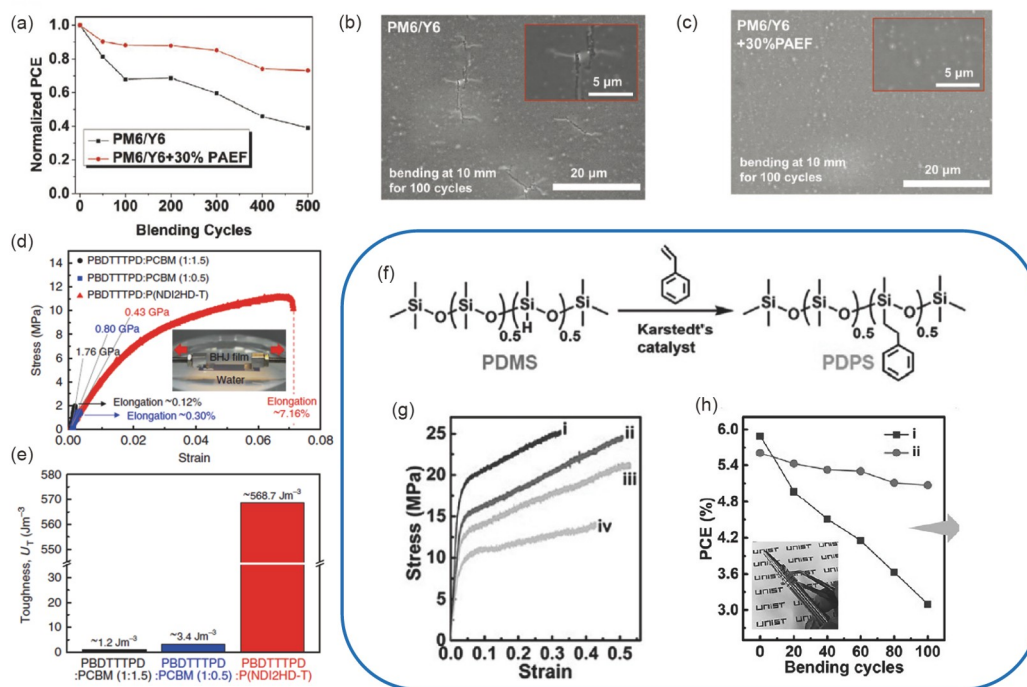
Figure 18 (a) Normalized PCEs as a function of bending cycles at a bending radius of 10 mm. Scanning electron microscopy images of the active layers after bending at 10 mm for 100 cycles: (b) PM6/Y6 without PAEF; (c) PM6/Y6 with 30% PAEF [172]. Strain-stress curves (d) and toughness (e) of polymer: PCBM and all-polymer blend films [175]. (f) Synthetic route for PDPS. (g) Strain-stress of blend films with different amounts of PDPS: (i) 0PDPS, (ii) 10PDPS, (iii) 20PDPS, (iv) 50PDPS. (h) The PCEs of (i) 0PDPS and (ii) 10PDPS based flexible all-polymer solar cells with bending cycles at a bending radius of 3 mm [176] (color online).

their high efficiency. The PCEs of all-polymer solar cells on the rigid substrates have recently reached up to 15.4% [178]. There will be more flexible OSCs based on all-polymer photoactive layers in the future.

4.5 Ultrathin and ultra-flexible organic solar cells

To evaluate the flexibility of flexible devices, cyclic bending tests with a fixed bending radius are often conducted. For the ultrathin flexible OSCs (the thickness of substrates is less than 10 μm), the conventional bending test is not suitable. The ultrathin devices are transferred to a pre-strained elastomer. The cell is at a flat or compressed state by stretching and releasing the elastomer. Through the stretching and releasing cycles, the mechanical flexibility of the ultrathin device is measured. During bending, tensile and compression stress are respectively experienced on the outer and inner surfaces. By balancing the tensile and compression stress, there is a neutral mechanical plane, where no stress is applied. The neutral plane is characterized by the distance b from the substrates [179]. Figure 19a shows the multilayer stacks from the substrate to the top later. E_i and h_i denote Young's moduli and thicknesses of the individual layers. The position of b is given by [180]

$$b = \frac{\sum_{i=1}^{n} E_i h_i \left[\left(\sum_{j=1}^{i} h_j \right) - \frac{h_i}{2} \right]}{\sum_{i=1}^{n} E_i h_i} \quad (2)$$

When bending at a radius of R, the strain ε_r at an arbitrary position (r is the distance from the bottom surface) yields [181]:

$$\varepsilon_r = \frac{r - b}{R + b} \quad (3)$$

The thickness of flexible substrates mentioned above is usually more than 100 μm, while the total thickness of OSCs including electrodes, buffer layers, and the photoactive layer is less than 1 μm, so the neutral plane is often located in the substrate, and b is about half of the thickness of the substrate. The strain of devices (r is equal to the thickness of substrates) can be simplified to $\varepsilon = d_1/(2R)$, where d_1 is the thickness of the substrate. According to this equation, the device bears a smaller strain at the same bending radius by choosing a thinner substrate. In other words, the thinner devices could ensure better bending stability. Several groups have fabricated flexible OSCs on ultrathin substrates. Kaltenbrunner *et al.* [182] reported an ultrathin OSC fabricated on 1.4-μm-thick PET and achieved a PCE of 4.2%. The ultrathin cell can reversibly withstand extreme mechanical deformation with a radius of 35 μm. Recently, Zhou's group [166] demonstrated an ultrathin OSC on 1.4-μm-thick PEN with a PCE of 15.0%, which is the best performance of ultrathin OSCs. The ultrathin cell shows nearly unchanged performance after deformation cycles at the compression ratio of 45%. The

deformation test was carried out with the assistance of a pre-stretched elastomer (Figure 19b–e). These ultrathin OSCs could remain their performance under a bending radius of tens of micrometers, showing excellent mechanical flexibility. According to Eq. (2), it is possible to minimize the degradation of the performance of the device by shifting the active devices to the neutral plane. The Someya group [183] fabricated the ultrathin solar cells sandwiched between two-parylene substrates (Figure 19f). The two-parylene films not only encapsulate the cells but also shift the position of the neutral plane. As shown in Figure 19g, their cells with the structure could bear 49% compression even with the brittle transparent electrode of ITO.

## 5 Semitransparent organic solar cells

In recent years, semi-transparent organic solar cells (ST-OSCs) have attracted significant attention due to their potential from the internet of things (IoT) to building-integrated photovoltaics (BIPV) [184,185]. Because of the structure of molecular orbitals, organic photovoltaic materials possess tailorable and discontinuous absorption characteristics (Figure 20a) [186–188], which offers their unique advantage for ST-OSCs. Partial photons can be captured by ST-OSCs for electrical power supply, while partial ones can penetrate ST-OSCs for daily requirements. There are two general parameters used to evaluate the performance of ST-OSCs, *i.e.*, power conversion efficiency (PCE) and average visible transmittance (AVT) [189]. In general, AVT is measured in the visible wavelength range and defined as follows:

$$AVT = \frac{\int T(\lambda) P(\lambda) S(\lambda) d(\lambda)}{\int P(\lambda) S(\lambda) d(\lambda)} \quad (4)$$

where T is the transmittance, P is the photopic response (determined by the spectral sensitivity of the human eye), S is the solar photon flux under AM 1.5G for window applications, and λ is the wavelength.

To achieve high PCE and AVT, the main strategy is to design narrow-bandgap (NBG) photovoltaic materials to realize the absorption of infrared region photons and also to keep the penetration of visible light through these materials. Besides, ternary strategy is also used by an ultra-narrow bandgap material as the third component *via* adjusting the polymer donor content in the active layer containing a wide bandgap polymer and narrow-bandgap small-molecular acceptor [190–192]. The precise control of the bandgap of the photoactive layer is the prerequisite to realize the fine adjustment of PCE and AVT. In this section, we mainly provide an overview of the research progress of the photoactive materials of ST-OSCs, and the application of ST-OSCs beyond photovoltaics will be discussed.
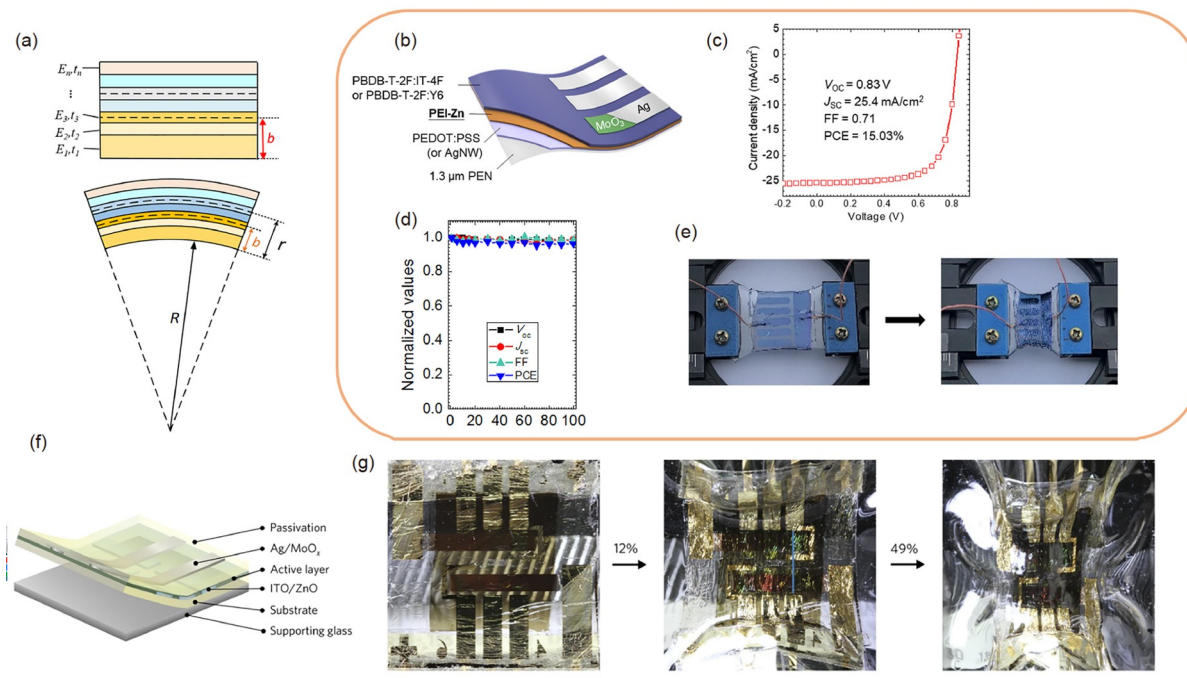
Figure 19 (a) Schematic of the flexible device under flat or bending states for analysis of bending strain. (b) Structure of the ultrathin OSC. (c) *J-V* characteristics of an ultrathin device. (d) Evolution of photovoltaic parameters after different compressed-flat cycles of ultrathin cells. (e) Ultrathin cells are attached onto the pre-stretched VHB. The cells are at flat state. Two wires are in contacted with the anode and the cathode of the cell, separately [166]. (f) Schematic of the double-side-coated OPVs. The ultrathin solar cells are sandwiched between two-parylene substrates. (g) Picture of ultrathin solar cells under different compression [183] (color online).

5.1 Polymer donors

Diketopyrrolopyrrole (DPP) unit is a widely used building block of NBG polymer materials due to its strong π-π interactions. Dou *et al.* [193] demonstrate efficient single and tandem polymer solar cells featuring a NBG-conjugated polymer PBDTT-DPP with a bandgap of 1.44 eV. Combining the highly transparent silver nanowire-metal oxide composite conducting network as the rear transparent electrode, a PCE of 4% was achieved for solution-processed ST-OSCs, in which maximum transparency of 66% was displayed at 550 nm [194]. PTB7-Th is another widely adopted NBG donor for ST-OSCs. Chen *et al.* [195] reported an acceptor-donor-acceptor (A-D-A) structured non-fullerene acceptor (ACS8) based on IDT as the core, alkylthio-substituted thiophene as the π-bridge and electron-withdrawing IC2F as the end groups, with an ultra-narrow bandgap (1.3 eV). ST-OSCs based on PTB7-Th:ACS8 exhibited a PCE of 11.1% with an AVT of 28.6%. Su *et al.* [196] reported ST-OSCs based on a trifluorinated polymer donor PBFTT and a tetrachlorinated acceptor IT-4Cl. The PBFTT:IT-4Cl pair showed matched energy levels, complementary absorption spectra in the NIR region and a good blend morphology. When ultra-thin Au was used as the electrode of ST-OSCs, PCEs of 7.9%–9.1% with an AVT of 37.3%–27.6% were realized. In 2014, Chang *et al.* [197]

demonstrated tandem ST-OSCs utilizing the same donor polymer blended with $PC_{61}BM$ or $PC_{71}BM$ as active layers in two sub-cells. Two polymers were used in this study: a medium bandgap polymer poly(indacenodithiophene-co-phananthrene-quinoxaline) (PIDT-phanQ) and an NBG polymer PCPDTFBT. The ST-OSCs based on PIDT-phanQ exhibited a PCE up to 8.5% with an AVT of ~40%.

5.2 Small-molecule acceptors

PCBM was chosen as the acceptor of ST-OSCs early [194]. However, the efficiency of PCBM-based ST-OSCs was poor owing to the low utilization of solar spectra. In 2015, Zhan *et al.* [198] demonstrated a non-fullerene acceptor ITIC, which not only promotes the rapid development of non-fullerene acceptors but also provides numerous narrow bandgap acceptors for ST-OSCs. Based on a strong electron-donating group dithienocyclopentathieno[3,2-b]thiophene flanked by strong electron-withdrawing group 1,1-dicyanomethylene-3-indanone, an acceptor IHIC with a narrow optical bandgap of 1.38 eV was synthesized and applied in ST-OSCs. Because of the strong near-infrared absorption and high extinction coefficients of IHIC, the ST-OSCs based on the blends of PTB7-Th:IHIC exhibited a champion PCE of 9.77% with an average AVT of 36% [199]. Through chlorination of the molecular structure to enhance the intramolecular charge
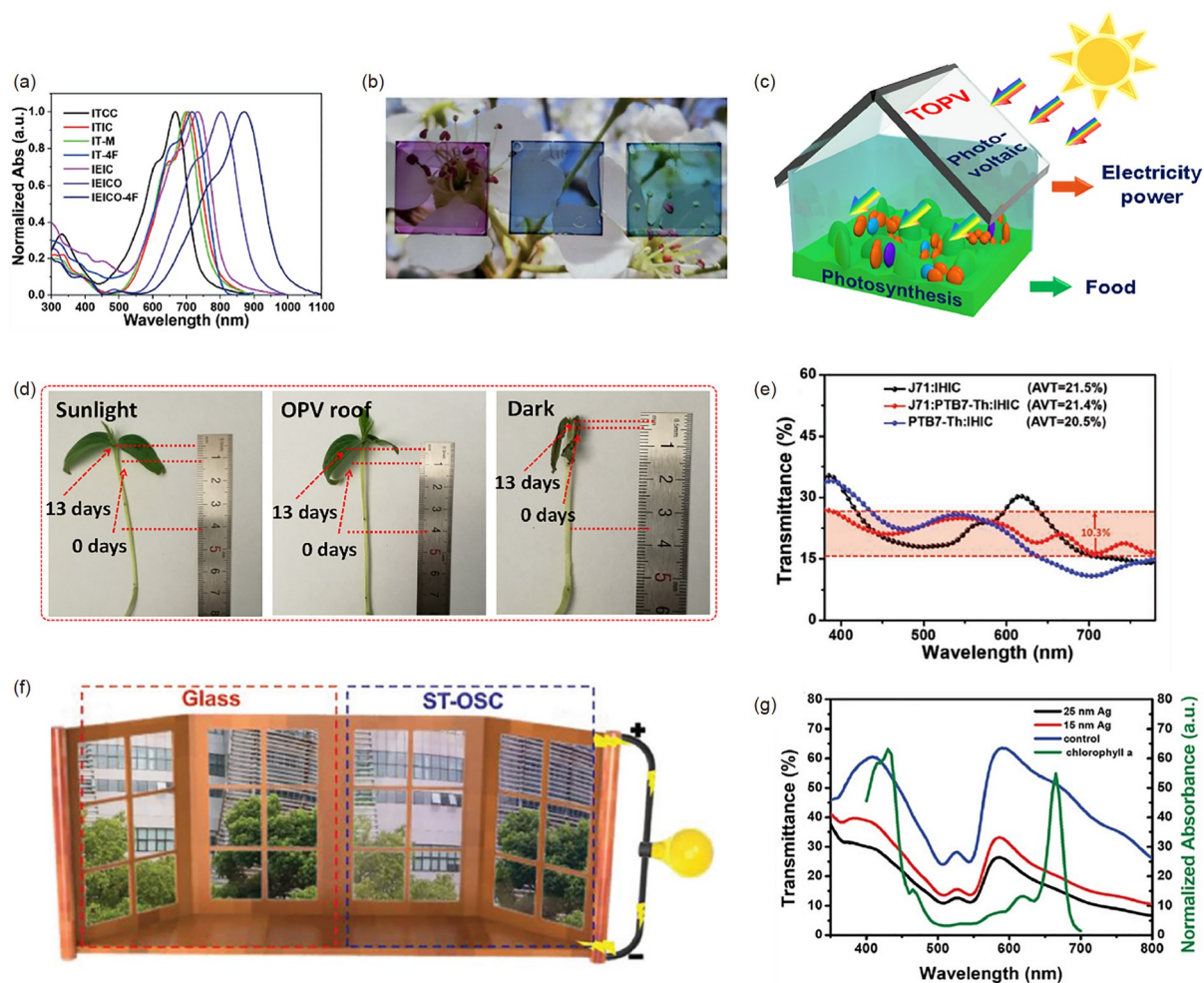
Figure 20 (a) Absorption spectra of organic photovoltaic materials with different bandgaps [186]. (b) Photograph of ST-OSCs with different photovoltaic materials [200]. (c) Schematic illustration of ST-OSCs for agricultural application [211]. (d) Photographs of the length change of Mung beans under different light conditions [211]. (e) Transmittance spectra of ST-OSCs with a dielectric mirror [208]. (f) Schematic illustration of ST-OSCs as a self-powered window of buildings [208]. (g) Transmission spectra of ST-OSCs with localized and discontinuous wavelength [212] (color online).

transfer effect, Cui *et al.* [200] synthesized an NBG (1.23 eV) non-fullerene acceptor IEICO-4Cl. The absorption spectrum of the IEICO-4Cl is mainly located in the near-infrared region, and a PCE of 8.38% with an AVT of 25.7% was achieved in ST-OSCs with it as the acceptor. Meanwhile, as shown in Figure 20b, when blended with different polymer donors (J52, PBDB-T, and PTB7-Th), the colors of the blend films can be tuned effectively. To increase the AVT, Li *et al.* [201] designed and synthesized a chlorinated NBG non-fullerene small molecule acceptor ID-4Cl and applied it for the fabrication of ST-OSCs. The introduction of chlorinated end groups reduces the optical bandgap of the acceptor and provides a strong absorption in the near-infrared region, avoiding the sensitive visible region of human vision. As a result, the ST-OSC based on PM6:ID-4Cl showed a PCE of 6.99% with an AVT of 43.7%.

Recently, the emergence of non-fullerene acceptor Y6 and its derivatives provides promising acceptors for ST-OSCs

[202]. Hu *et al.* [203] reported ST-OSCs based on PM6:Y6, in which the opaque OSCs and ST-OSCs exhibited high PCEs of 15.7% and 12.37%, respectively. Li *et al.* [204] developed ternary blends with alloy-like near-infrared (NIR) acceptors, which are effective to improve device efficiency while maintaining visible transmittance, resulting in a PCE of 13.1% for ST-OSCs with an AVT of 22.4%. Zheng *et al.* [205] reported a ladder-type dithienonaphthalene-based acceptor (DTNIF) with a high-lying LUMO energy level and adopted it as a third component material in ternary OSCs, in which a PCE of 13.49% is achieved when the AVT is 22.58%. Luo *et al.* [206] designed and synthesized an NBG electron acceptor Y14 based on a new fused dithienothio-phen[3,2-b]-pyrrolobenzotriazole (BTA-core). The ST-OSCs based on PBDB-T:Y14 yielded a PCE of 12.67% with an AVT of 23.69%, demonstrating that the NBG BTA-core-based non-fullerene acceptors are promising candidates toward high-performance ST-OSCs.

5.3 Application beyond photovoltaics

ST-OSCs are deemed to be one of the most promising photovoltaic devices from IoT to BIPV due to their flexibility, lightweight and transparency [183,207–210]. Within the AM 1.5 G solar spectrum, 47% and 51% of the solar energy are distributed within the visible and the infrared region, respectively. On the other hand, 10%−50% of visible transmittance is suitable for the growth of lots of plants [184]. Therefore, ST-OSCs possess a great potential in agricultural application. For instance, Liu *et al*. [211] applied high-performance flexible ST-OSCs as the roof and windows of a "greenhouse" (Figure 20c). In this case, PTB7-Th was used as the donor with different acceptors of IEICO-4F, FOIC and F8IC, respectively. Infrared region photons can be captured by ST-OSCs for electrical power supply; in the meantime, visible light can penetrate solar cells for the plant growth. It is found that the growth status of Mung beans under different sunlight (sunlight filtered by ST-OSCs and normal sunlight) had similar results, as shown in Figure 20d. Zhang *et al*. [208] introduced a dielectric mirror to control the reflected intensity of wavelength. The distribution of transmittance intensity became more uniform (Figure 20e) and the color-rendering index approached 100. Therefore, the ST-OSC has potential as self-powered windows of buildings, as the illustration presented in Figure 20f. Intriguingly, Wang *et al*. [212] recently found that the transparent region of ST-OSCs can match well with the absorption of chlorophyll a, as shown in Figure 20g, when PB2TCl-o:BTP-eC9-4F was used as the active layers of ST-OSCs. In other words, despite tuning the molecular structure of organic photovoltaic materials, their absorption range can be designed, and consequently, the ST-OSC can tailor the solar spectra targeting different applications beyond photovoltaics.

6 Scaling-up of organic solar cells

With the rapid development of NFAs, a big progress of small-area OSCs has been made in recent years. Nowadays, scaling-up of the organic solar cells (OSCs) becomes the most challenge for the commercialization of OSCs. This part will introduce the printing technology for the large-area OSCs, summarize the development of the rigid and flexible large-area OSCs, and analyze the main challenges for the development of large-area OSCs.

First of all, the solidification physics that controls the film thickness and drying behavior of the active layer is the necessary background to discuss the challenge of scaling up roll-to-roll (R2R) manufacturing. Spin-coating is now the most commonly used thin film deposition technique in laboratories. As shown in Figure 21a, spin-coating is generally carried out in two stages, and the final film thickness has no

connection with the amount of distribution. Due to the centrifugal force, the distributed fluid is ejected from the edge of the substrate at a rate proportional to the cube of the film thickness. When they are self-leveling, the thickness of resulting film is uniform. Therefore, the waste of materials caused by this method is also very serious. When the spray rate is made smaller than the evaporation rate to reduce the film thickness, a wet film is formed and it dried by evaporation. The centrifugal flow of the environment atmosphere around the sample surface may cause the film to dry quickly and make it unstable. However, the meniscus of the film never crosses the substrate, so the spin coating is relatively stable in terms of ink wetting characteristics.

In order to successfully transfer the small-area OSCs prepared by a laboratory-scale process to the large-area OSCs produced in industry, using solution-processing technology that mimics the industrial manufacturing process to develop OSCs devices is very important. When using solution-processable organic semiconductors for cost-effective large-scale solar panel production, the meniscus-guided coating (MGC) method of blade coating, slot die coating, bar coating and solution shearing illustrated in Figure 21b–f has great potential to be used for large-scale OSC production [213–215]. Since different technologies will lead to different active layer morphologies, it is a challenge to find the ideal coating technology to manufacture high-performance polymer solar cells. When the air, solution and solid substrate form a three-phase contact line, a meniscus at the interface of liquid and air will appear. The rheological properties of photoactive inks are important for controlling the ejection of satellite-free droplets and inducing precipitation of crystalline polymers. Moreover, the appropriate solubility and
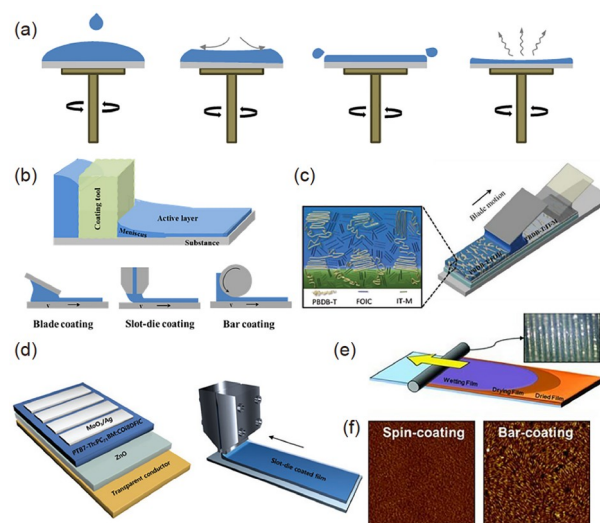
Figure 21 (a) A schematic process of spin coating. (b) The schematic illustration of the typical meniscus-guided coating. A schematic of (c) LbL sequential blade coating, (d) slot-die coating, and (e) bar coating method. (f) The atomic force microscope (AFM) images of active layers processed by spin coating and slot-die coating [213–215] (color online).

volatility of photoactive inks, which is linked to the dynamic viscosity, can enhance the processability of the ink and avoid nozzle clogging. The evaporation of the volatile solvent on the meniscus causes the solution to flow outward to compensate for the evaporation loss, thus leaving accumulated non-volatile solutes near the contact line. This ring residue is called a coffee stain or coffee ring. The coffee ring effect (CRE) will cause uneven film deposition and thereby reduce the performance of solution-processed devices. By using a coating head which controls film deposition to make the meniscus traverse the substrate, MGC is working to suppress the CRE of the solution droplets. The fluid flow during blade coating is usually composed of a major shear flow and a minimal extension flow.

Blade coating is a simple and effective technology to prepare large-area devices. It is a prototype tool for slot die coating and a self-metering technique like spin coating. The wet film thickness is determined by the blade speed and the film viscosity. The change in wet film thickness is close to ~2/3 when using the horizontal dip-coating method or the Landau-Levich regime, where v is the blade speed. Unlike spin coating, this technology does not waste material because it is easy to dispense the solution volume that matches the final required film area, and the energy loss of the devices processed by blade coating is less than the devices fabricated by spin coating as shown in Figure 22a–c [216]. The stability of the coating depends on the wetting characteristics of the solution on the substrate, and the final film morphology depends on the drying conditions (substrate temperature and ambient gas flow) after the wet film is deposited. The substrate temperature and ambient gas flow can affect the volatilization efficiency of the ink solution, which has great influence on the aggregation and crystalline orientation properties of organic materials, leading to different morphology when printing at different substrate temperatures and ambient gas flow. Furthermore, the layer-by-layer (LbL) sequential blade-coating method as shown in Figure 22d has been developed [217,218]. Compared with the BHJ film, the active layer film prepared by the LbL sequential blade-coating method has a higher absorption coefficient, larger domain size and vertical phase separation, which is conducive to charge transport and extraction performance (Figure 22e, f) [31,216,217]. As demonstrated in Figure 22i, j, blade-coating with a patterned squeegee is also effective in changing the flow-induced conformation and increasing the orientation ordering to lower the free energy barrier to nucleation for increasing the nucleation density [219].

For industrial-scale deposition, slot-die coating, which can deposit a striped patterned layer, is usually the most accurate coating method for thin films associated with organic photovoltaics. The ink can be directly loaded into the coating head under pressure and translated perpendicular to the substrate to form a striped pattern. Slot-die coating is a pre-

metered technology. Factors such as the viscosity of the polymer ink, the coating speed and the thickness of the mask, especially the solubility parameter strongly affect the morphology of the slot-die coating film (Figure 22g, h) [220]. In slot-die coating, the wet film thickness is determined by the ratio of the solution delivery rate to the moving substrate speed. Therefore, the resulting active layer film thickness is easy to be controlled and the materials are saved. In this technology, a series of web-speeds and solution rates can be used to solve the technical instability (such as chattering) caused by the wetting characteristics of the ink on the surface of the solid substrate and the underside of the die. The final film morphology by using this technology is determined by the evolution of the wet film in the downstream dryer, which is usually carried out under moderate heating (<100 °C). Compared with spin-coating, although the slot-die coating can save material, because the entire length of the dryer must be determined to determine the film characteristics, the optimization requires the use of a large amount of material.

Some researchers have discovered that Hansen solubility and temperature parameters can actually be used to determine the appropriate solvent system to prepare active layer films with excellent performance. Thus, they found that a single solvent that can controllably dissolve the donor and acceptor according to the process temperature can be used to optimize the active layer film instead of a co-solvent system that uses a host solvent and solvent additives. By using MGC technology, the coating can be stacked layer by layer as shown in Figure 22k [221]. The polymer donor coating exhibits pre-aggregation of polymer chains with enhanced molecular face-to-face orientation, which is beneficial to improve the charge transport and J_{SC}. And the phase separation and domain size are more appropriate compared with the one-step-coated active layer film.

In addition to spin coating or MGC methods, there are also various large-area coating methods. Spraying is a representative coating method to form a series of layers that make up the OPV structure. Spraying is a non-contact, fast and scalable coating technique in which ink is atomized through a nozzle, and is compatible with solutions with different viscosities. Due to its high-resolution printing capabilities and its suitability for free-form manufacturing, inkjet printing technology can be used to prepare solution-processable OPV. However, there are still some unresolved problems when preparing the inks from organic materials like the inks is usually required to have appropriate viscosity and surface tension, and the volatile solvents contained also can cause the precipitation of crystalline polymers sometimes.

Doctor blade and slot-die coating are preferred processing methods for laboratory researchers in the large-area printing of organic solar cells because the ink formulation used, including solvent, concentration, additives, can be optimized
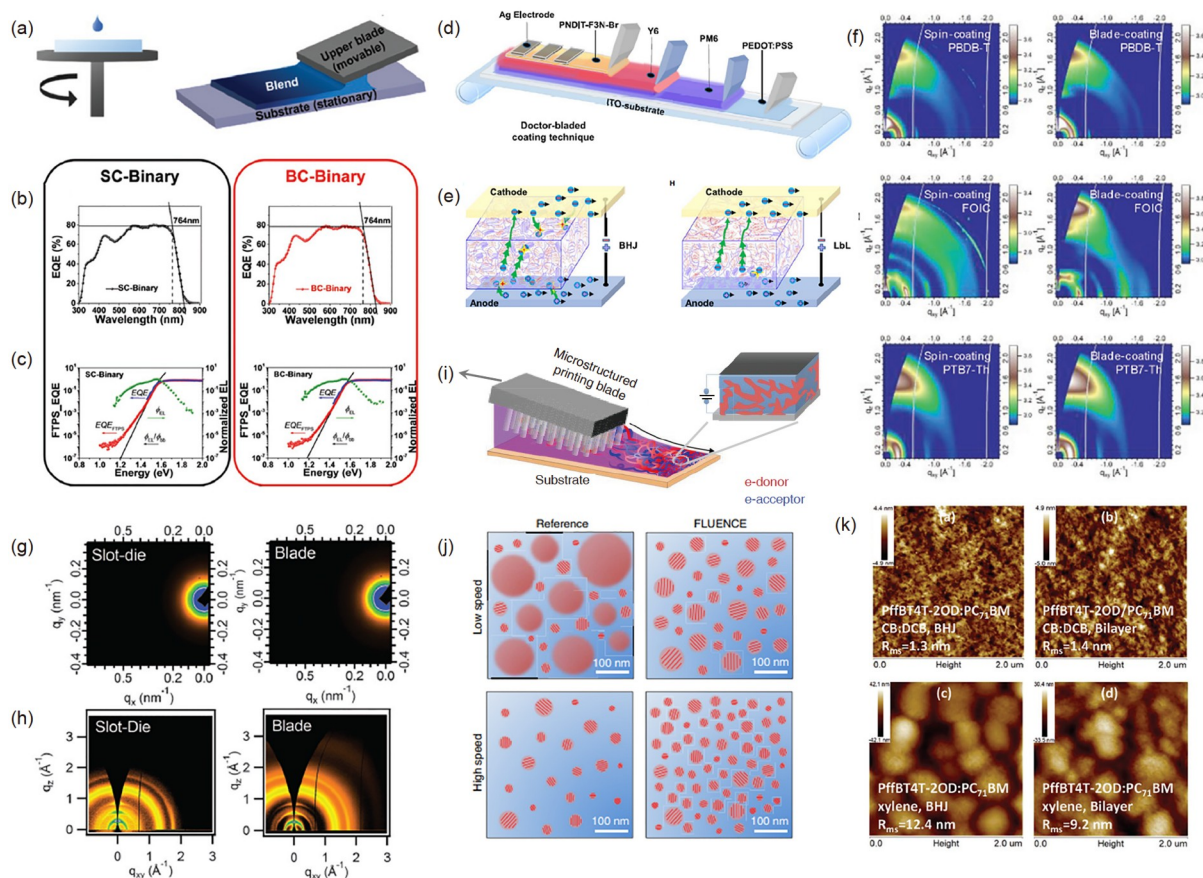
Figure 22 (a) The schematics of spin coating, blade coating. (b) EQE spectra, (c) measured quantum efficiency (EQE, blue line), Fourier transform photocurrent spectroscopy (FTPS-EQE, red lines), electroluminescence (EL, green lines), and external quantum efficiency (black lines) of the devices processed by spin coating and blade coating method. (d) A schematic of large-area LbL sequential blade coating method. (e) The illustrations of possible morphological features and physical processes of BHJ and LbL blend-based devices. (f) The 2D GIWAXS patterns of active layer films processed by spin coating and blade coating method. (g) R-SoXS and (h) GIXD of slot-die and blade coated films. (i) A schematic of the blade coating process using a special blade with arrays of micropillars. (j) Schematic illustrating the possible in-plane morphology. The blue medium denotes the amorphous electron-acceptor polymer, and the red domains represent electron donor, forming amorphous (shown without red bars) and semi-crystalline domains (with red bars). (k) AFM images of active layers processed with CB:DCB solvent in BHJ structure, CB:DCB solvent in bilayer structure, xylene solvent in BHJ structure, and xylene solvent in bilayer structure [31,216,217,219–221] (color online).

and transferred from spin-coating. However, doctor-blading and spin-coating are basically different. Thereby, a big challenge is how to achieve lab-to-manufacturing translation. To comprehensively describe the morphology evolution during such a lab-to manufacturing translation process, a quantitative transformation factor of shear impulse was proposed by Chen *et al.* [58]. They confirmed the impulse conversion factor between the traditional spin coating process and the slot die coating through studying the ink concentration and the specific parameters in the film-making process (Figure 23a–d). On the basis of the theory, the film morphology could be optimized and compared with the spin-coated films, and the efficiencies of the solar cell devices based on the fullerene acceptor (PTB7-Th:PC$_{71}$BM) and nonfullerene acceptor (PBDB-T:ITIC) with an effective area of 1.04 cm^2 reached 9.10% and 9.77%, and efficiencies of the solar cell modules with an effective area of 15 cm^2 were 7.58% and 8.90%, respectively.

The film morphology and homogeneity of the large-area films should be paid pay attention to the large-area OSCs. Generally, the photoactive films were deposited at relatively low temperature during the spin-coating. However, several groups demonstrated the temperature both of solution and substrate should be controlled at higher temperature during doctor-blade and slot-die coating. Particularly, this was an effective method to regulate the aggregation and crystallization process of the NFA-involved films (Figure 23e–h) [43]. Such a strategy was suitable to regulate the slot-die coated films either with halogenated or hydrocarbon solvents [42]. Besides fabrication temperature, the additives suitable for doctor-blade coating were also different from those for spin-coating. Among various additives, 1,8-diiooddooctane (DIO), 1,8-octanedithiol (ODT), and chloronaphthalene (CN), the use of ODT allowed higher performance and device stability [222]. In addition, the NFA easily formed excessive aggregation in the doctor-blade or slot-die coated
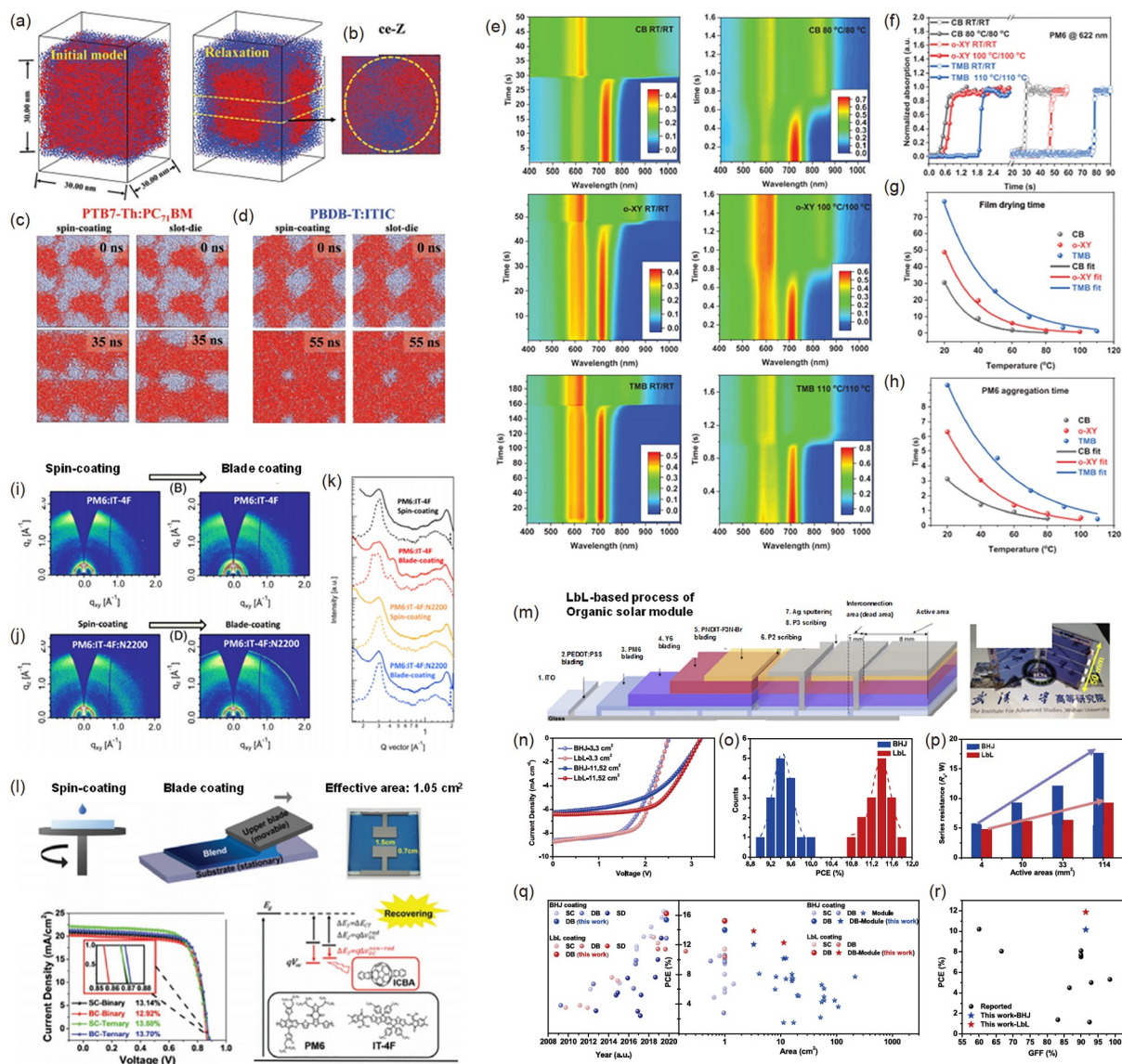
Figure 23   (a) Simulation protocol of PTB7-Th:PC$_{71}$BM blend films. (b) Picked slice from the *Z*-direction. (c) Time sequence snapshots of the PTB7-Th: PC$_{71}$BM from CGMD simulation. (d) Time sequence snapshots of PBDB-T:ITIC blend from solution [58]. (e) The evolution of the UV-vis absorption spectra during slot-die coating at different temperatures. (f) Normalized absorption at 622 nmduring slot-die coating at different temperatures. (g) Temperature dependent drying process, (h) aggregation time of PM6 [42]. (i) GIWAXS 2D patterns of the spin-coated PM6:IT-4F, blade-coated PM6:IT-4F. (j) GIWAXS 2D patterns of the spin-coated PM6:IT-4F, blade-coated PM6:IT-4F:N2200. (k) Out of plane and in-plane profiles of the films [223]. (l) *J-V* curves of the spin-coated (SC)-binary, doctor-blade coated (DC)-binary, SC-ternary, and DC-ternary device with the area of 1.05 cm^2. Schematic diagram of the corporation of ICBA lead to recover energy loss [216]. (m) LbL-based process of the organic solar modules. (n) *J-V* curves of the large-area modules. (o) Histograms of the large modules with BJH and LbL strategy. (p) Series resistance of the devices. (q) Development of OSCs fabricated through spin-coating and doctor-blade coating. (r) Distribution of the PCEs of the solar modules and the GFF values [217] (color online).

films and caused unexpected charge recombination. Huang *et al.* [223] reported the additive of n-type polymer acceptor N2200 have suppressed the aggregation of NFA, and ensured an ideal morphology with appropriate domain size (Figure 23i–k). The slot-die coated device with 1 cm^2 area showed a high performance of 15.1%. Similarly, Min and Chen *et al.* [216] demonstrated the introduction of ICBA in the photo-active blend films could induce a desired morphology of the active layer and overcome the undesirable nonradiative re-combination, leading to an enhanced efficiency of 13.07%

(1.05 cm^2) in the doctor-blade coated device relative to the binary device (12.92%) (Figure 23l). Further, the result showed the formation of alloyed acceptor in ternary blend films could enable the formation of pseudo-planar hetero-junction [224]. In recent years, researchers also found that LbL or sequential deposition can achieve comparable or even better device efficiency than one-step coated organic films since the sequential deposition of donors and acceptors can greatly regulate the phase separation morphology. Moreover, a wider range of solvents including non-halogen solvents can

be selected to achieve high performance [221]. Min *et al.* [217] demonstrated the LbL route was effective to lower the scaling lag of large area devices. The PM6:Y6 device in the 3.3 and 11.52 cm^2 module showed a performance of 13.88% and 11.86%, both higher than the devices fabricated from the conventional method (12.06% and 10.15% for the 3.3 and 11.52 cm^2 device) (Figure 23m–r).

For large-area device fabricated by printing or coating, the reproducibility is lower than the small-area device, because the defects on the large-area thin films would cause leakage current. Zhou *et al.* [225] demonstrated large-area tandem device has higher defect tolerance than the single cells because the thickness of the tandem device is much higher than the single device. For the 10.5 cm^2 P3HT: ICBA device with performance around 6.5%, the fabrication yield was over 90%. Similarly, high thickness-tolerability of the functional layers also largely lowered the printing difficulties and improved the device efficiency of large-area cells. Therefore, several groups devoted to developing thickness-insensitive materials. For example, Hou *et al.* [226] developed the BTP-4Cl acceptor, which showed good large-area compatibility and good processability. For the PM6:BTP-4Cl-12 heterojunction solar cells, the performance of 1 cm^2 device reached 15.5%. When the thickness of this heterojunction reached as high as 1,000 nm, the performance of 4 cm^2 OSCs was higher than 10% too [227]. Besides, a ternary strategy containing two or more than two donors or acceptors in the heterojunction layers increased the working thickness as well [228,229]. Wei *et al.* [229] reported the ternary devices with 15% p-DTS(FBTTH$_2$)$_2$ exhibited a PCE of ~10.7% with the thickness of 200–270 nm,which enabled an efficiency of 5.18% for a 20 cm^2 module. Chen *et al.* [230] demonstrated the ternary pseudo planar heterojunction strategy could induce favorable vertical phase separation during doctor-blade, which enabled high-performance 1 cm^2 devices.

Arising from longer time before drying, the morphology of the film is more impacted by surface energy of the substrates during large-area coating or printing. So, the interface layer should meet a higher requirement for the large-area devices than the small ones. Ji *et al.* [231] found the device performance and repeatability of the doctor-blade OSCs were inferior to the spin-coated cells. Reducing the surface roughness of the ZnO electron transporting layer enhanced interface compatibility between the active layer and buffer layers, and lowered the device decrease during upscaling. In order to simplify the device preparation process, the interface materials could be mixed with the active layer, and the interface layer can be enriched at the interface through self-assembly, and a high efficiency device can also be obtained. Hou *et al.* [232] mixed the PFN interfacial layer material with the PBDB-T:IT-M active layer material. After solvent treatment, PFN was enriched at the bottom of the film and formed a self-assembled electron transport layer, and the

obtained performance was comparable to the common devices. The self-assembly strategy has been applied during slot-die coating technique [233].

The large-area OSCs modules were formed through connecting the single cells in series and shunt (Figure 24a, b). Therefore, the performance was not only decided by the efficiency of single device, but also by the dead area between the single cells. The larger the dead area is, the lower geometric fill factor (GFF) of the module devices. Limited by the conduction of the transparent conductive electrode, the width of the stripe is usually limited around 1 cm. Due to the high cost of the laser equipment; the dead area was still large in most of the works. The two aspects above resulted in the lag of module efficiency. Therefore, developing high quality transparent conductive rigid and flexible electrode, and lowering the dead width should be comprehensively studied. The conventional ITO electrode was the most widely used electrode for the large-area rigid OSCs. Besides glass/ITO electrode, the thin metal electrode has smaller sheet resistance and gave potential performance as well. Zhou *et al.* [234] reported the efficiency of 10.24% for the 10 cm^2 single device with thin Ag layer transparent electrode. Though the conventional ITO transparent electrode on the glass substrate has good conduction with a sheet resistance around 10 Ω/cm^2, the flexible ITO electrode has always the sheet resistance higher than 30 Ω/cm^2. Such a large sheet resistance would cause high electrical loss during upscaling of the OSCs. Some candidates including metal grid [138,153,235], metal nanowires [236], graphene electrode have been developed for the use in large-area flexible OSCs. These greatly pushed the development of the large-area flexible OSCs.

Since the early report on scaling-up printing of OSCs around the year of 2010 (Figure 24c) [237], great progress has been made in the efficiency development for the large-area OSCs. In 2019, Huang *et al* [238]. prepared a 216 cm^2 PTB7-Th: PC$_{71}$BM cell module with an efficiency of 5.6%, and a semi-transparent cell with the same area also achieved an efficiency of 4.5% (Figure 24d, e). In 2020, Brabec *et al.* [239] reported an organic solar cell module with an area efficiency of 12.6% for 26 cm^2 and an efficiency of 11.7% for 204 cm^2, which is currently the highest efficiency for organic solar cell modules. The performance of large-area flexible OSCs is also developed quickly from 2016 due to the development of the high-efficient NFAs. Till now, the reported highest performance of the large-area flexible OSCs for the single and module was 13.61% [236] and 10.09% [138,240], respectively.

In all, both the large-area rigid and flexible OSCs have obtained great breakthrough in recent years. The highest performance is higher than 10% for the size of 100–200 cm^2. However, this size is still not large enough for the real application. Though new materials have contributed mostly to
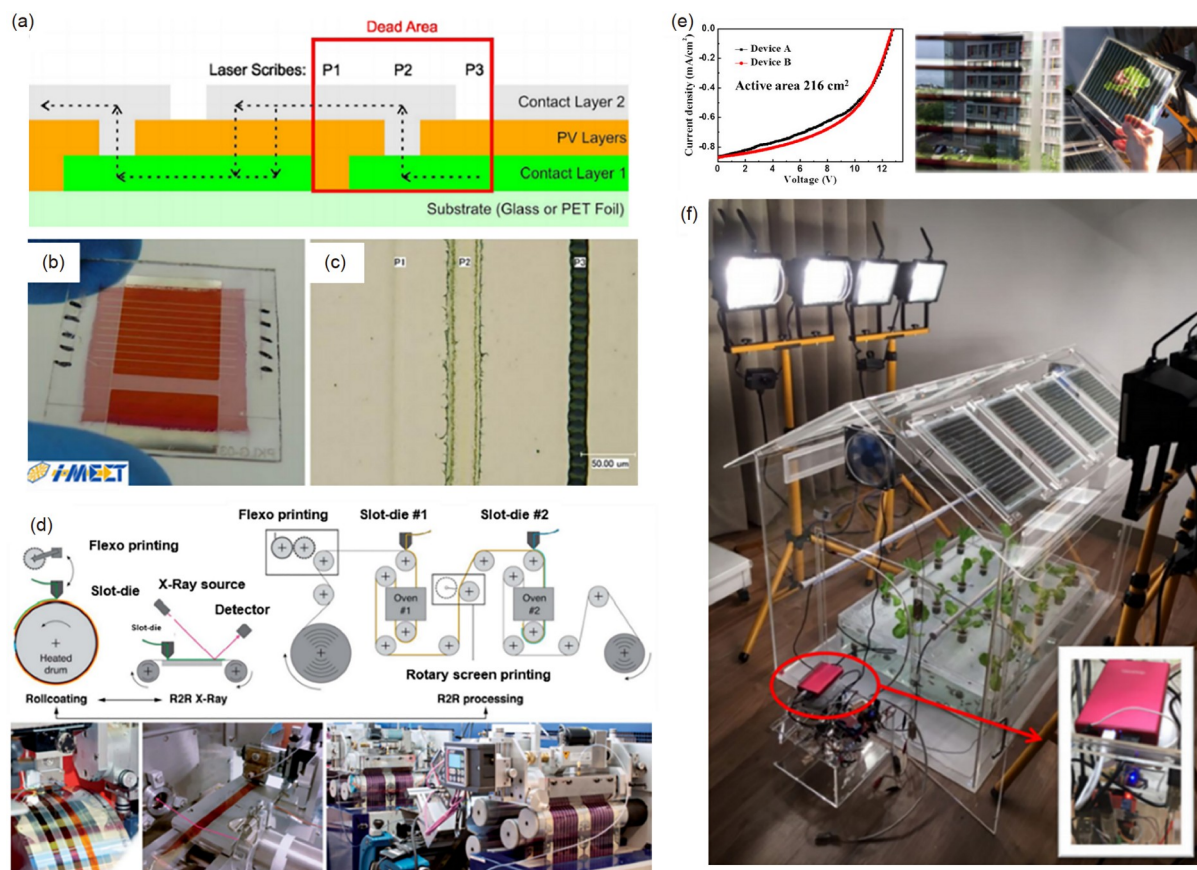
Figure 24   (a) Cross section of the monolithic interconnection. Patterning lines: P1, P2 and P3. (b) Photographs of the large-area module, and (c) the patterning line [239]. (d) Schematic diagram of the roll-to-roll printing [237]. (e) *J-V* characteristics of a 216 cm² module and the module photographs. (f) photograph of eight transparent panels on the roof of a greenhouse [238] (color online).

high performance large-area OSCs in the recent past years, some typical high-performance materials are not suitable for large-area roll-to-roll printing. The morphology regulation during large-area printing is still not mature. Therefore, the printing compatibility of the materials and printing technology should be more concerned at present and in the future.

7   Degradation and stability improvement of organic solar cells

With the rapid development of PCE, the stability of OSCs has become the next most critical issue before commercialization [241–244]. OSCs are composed of multiple nanometer organic or inorganic thin films. These nano-thin films are susceptible to performance degradation under various stress factors (Figure 25), such as water [245–247], oxygen [248], light [249,250], thermal heating [251], and even electric field [252,253], which leads to slow or fast performance decay through different pathways [241,244,254]. Among these stress factors, water and oxygen can destroy the cells irreversibly through the chemical oxidation of

various materials, which is even more severe when light illumination is included. They react with metal electrodes causing the corrosion of electrodes [245], or change the electronic property of interfacial PEDOT:PSS layer by absorbing water [247], or oxidize conjugated organic semiconductors leading to the decomposition of organic materials [248,255]. Since the chemical reaction of oxygen/water with the materials of OSCs requires the contact of the cell with oxygen/water, good encapsulation can separate the cell from the oxygen/water and then suppress this degradation pathway [255–258]. Different encapsulation methods can be seen in the literatures. For example, Tsai and Chang [256] reported the preparation of Al_2O_3/HfO_2 composite encapsulation layers by atomic layer deposition (ALD) for P3HT:$PC_{61}BM$ cells. The 26 nm Al_2O_3/HfO_2 nano-composite encapsulating film showed a water vapor transmission rate (WVTR) ($<5 \times 10^{-4}$ g/(m² day)), successfully preventing the aggression of O_2/H_2O, and the encapsulated cells retained >70% of their initial PCE upon >10,000 h storage in the accelerated aging condition of ambient air or upon >1,800 h in a 65 °C/60% RH. Sapkota *et al*. [257] reported that flexible P3HT:$PC_{61}BM$ cells encapsulated between two barrier films maintained >95% of their initial device performance
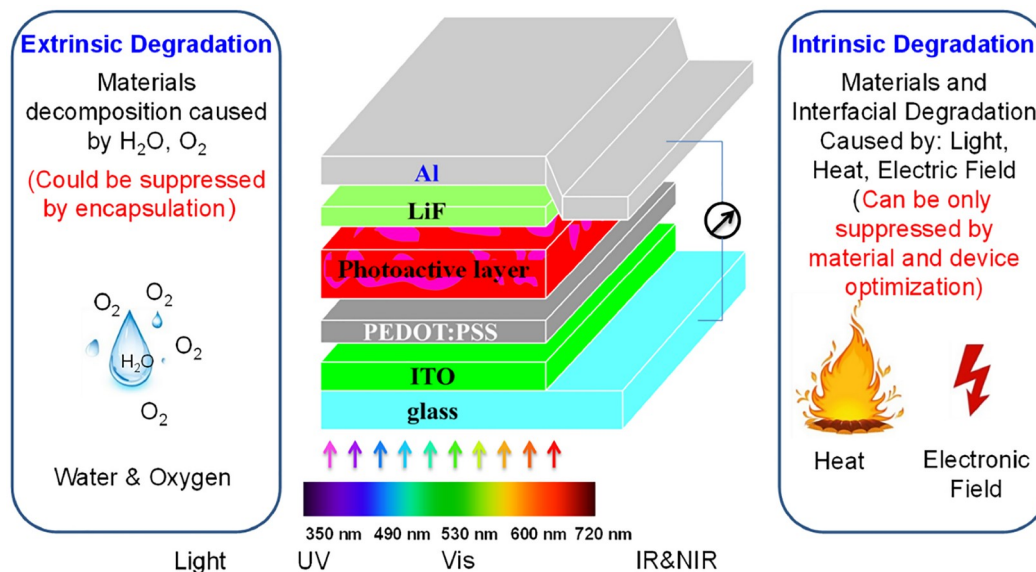
Figure 25   Device structure of polymer solar cells and various degradation pathways of the cells [244] (color online).

after 1,000 h of aging under damp-heat conditions (85 °C/ 85% RH) according to IEC standard. Very recently, a solution-processed multilayered barrier film was prepared by depositing perhydropolysilazane (PHPS) ink and then converted into a silica layer by deep UV irradiation. With this solution-processed barrier layers, P3HT:PC$_{61}$BM cells showed an enhanced device lifetime in damp heat conditions beyond 300 h [258].

In addition to water and oxygen, polymer solar cells under operation encounter the stresses of light, heat, and electric field, which will also lead to the performance decays. For example, Guldi *et al.* [259] demonstrated that photon-induced dimerization of PC$_{61}$BM happened for the fullerene-based cells, which reduced the charge carrier mobility and affected fill factor and short circuit current of OSCs. Thermally induced morphology change within the photoactive layer was proved to be another essential pathway for the performance decay of fullerene [251,260,261] and non-fullerene solar cells [262]. Yan *et al.* [263] demonstrated that performance decay of the polymer solar cells is external load-dependent, suggesting that the strength of the electric field will influence the performance decay as well. Unlike water and oxygen, light (for generating charges within the photoactive layer), heat (temperature increasing under light illumination), and electric fields (there be always internal and external electric fields under operation) are inevitably encountered when a cell is under operation. Also, these stress factors cannot be isolated by encapsulation. Therefore, performance decays of PSCs caused by light, heat and electric field are considered as the inherent or intrinsic decay process [254], which is closely related to the stability of materials used and devices' layered structure. Forrest *et al.* [264] re-

ported that thermally evaporated organic solar cells showed an extrapolating lifetime of over 27,000 years, suggesting that organic solar cells can be intrinsically stable enough for application. However, most of the solution-processed polymer solar cells showed a T_{80} lifetime (at a time reach the cell's 80% of its initial performance) typically less than 1,000 h [265,266]. Therefore, it is still highly needed to understand the intrinsic degradation processes of the PSCs and to find proper ways to suppress these degradation processes [241,242,244]. The following section will give a summary on the latest research progress on the understanding the intrinsic degradation processes of the fullerene and nonfullerene solar cells.

7.1   Degradation of fullerene-based solar cells

Depending on the acceptor used in the cells, polymer solar cells can be classified into fullerene solar cells and non-fullerene solar cells [267–269]. Owing to the different molecular structures, these two different types of cells showed totally different degradation behaviors and mechanisms. Fullerene solar cells are the most well studied OSCs [270], not only the working principles, but also the degradation pathway and mechanisms [254]. Based on the enormous research efforts devoted in the last two decades, the intrinsic degradation pathways of fullerene solar cells are well clarified [242,254,268,271,272], which include (Figure 26): (1) photodimerization of fullerene within the photoactive layer. Guldi *et al.* [259] proved that the fullerene molecules underwent dimerization, which decreased the inherent charge carrier mobility and the consequent power conversion efficiency. Heumueller and Yan *et al.* further proved that such a
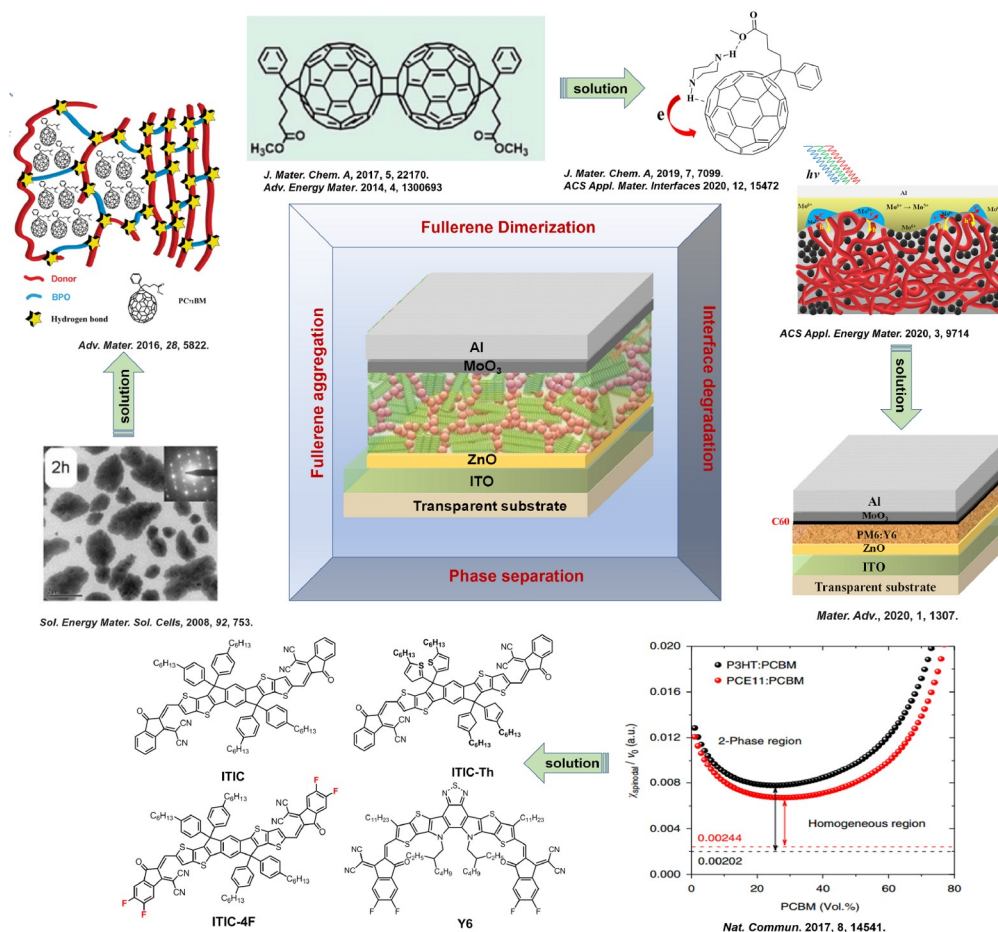
Figure 26 Degradation pathways and stability improvement methods for polymer:fullerene solar cells (color online).

photon dimerization process was morphology- [252] and external load-dependent [263]. (2) Interfacial degradation. Yan and Gu recently demonstrated that photon-induced reduction of Mo^{6+} happened on the polymer:fullerene cells under operation, which significantly reduced the V_{OC} and FF [273,274]. (3) Aggregation of fullerene molecules. Increased temperature of the cell under operation will increases the molecular motion within the photoactive layer. Owing to the high crystalline nature of fullerene molecules, fullerene molecules turned to aggregate under thermal stress, which inherently reduced the charge generation and transporting efficiency [275]. (4) Phase separation. Owing to the different compatibility of the polymer donor and fullerene molecules, the intermixed nanophases are not inherently stable. Li *et al.* [276] proved that PffBT4T-2OD:PC_{61}BM cells showed dramatic performance decay even when the cells are stored in the dark at room temperature, which was ascribed to the spinodal donor-acceptor demixing. Also, it was reported that the energy disorder will increase for the low crystalline polymers under operation, which will lead to the decrease of V_{OC} as well [277,278].

In response to the degradation of device performance

caused by fullerene dimerization, Ma *et al.* [279,280] reported the use of organic amines to quench the triplet of fullerene molecules, so as to inhibit fullerene dimerization (Figure 26). With this, J_{SC} decay was significantly suppressed and device stability was greatly improved. A more detailed comparison of the substitutes of piperazine derivatives on the stabilization effect confirmed that the N–H bond of piperazine enhanced the intermolecular interaction between fullerene and piperazine, which promoted the intermolecular charge transfer between these two components [280]. Quantum calculations on the intermolecular binding energy between oligothiophenes, PC_{61}BM, and piperazine molecules revealed that piperazine molecules were preferentially localized at the polymer:fullerene interface, which indicated that the photo dimerization of PC_{61}BM mainly happened at the donor/acceptor interface, and the organic amine serves as the targeting stabilizer at the interface [281]. The proved interfacial photon reduction of MoO_3 was reported to be suppressed by inserting a thin C_{60} layer [274]. In addition, using volatile piperazine as the additive increases the concentration of fullerene on top of the photoactive layer, which improves device stability as well [274].

As for the molecule-aggregation-induced performance decay, using polymer matrix with high glass transition temperature T_g [282], ternary strategy [283,284], is an effective way to improve the morphology stability. Since high glass transition temperature (T_g) polymers exhibit low molecular motion under T_g, using high T_g polymer matrix could decelerate the morphology change and consequently slow down the performance decay induced by the morphology changes. For example, Bertho *et al.* [282] found that when heated at 110 °C, the low-T_g MDMO-PPV:PC$_{61}$BM film formed clear large-scale PC$_{61}$BM crystals, whereas the high-T_g MDMOPPV:PC$_{61}$BM film hardly formed crystals. Also, using a third component which has a high co-crystallization with either component of the photoactive layer is also able to improve the morphology stability by "freezing" the nano structure. Zhang *et al.* [285] reported the use of BTR as a third component in PffBT4T-2OD:PC$_{71}$BM solar cells. The BTR can inhibit the excessive aggregation of PffBT4T-2OD, resulting in better device performance and stability. In addition to this, replacing PC$_{61}$BM with nonfullerene acceptor IDTBR was found to be able to suppress the "burn-in" degradation of the cell, which was ascribed to the good compatibility of NFA with polymers donor [286]. This is considered to be a good way to improve device stability.

Owing to their low light absorption ability and difficulties in chemical functionalization, fullerene acceptors are not the leading molecular acceptors for OSCs at the current moment. However, fullerene derivatives are still used in polymer solar cells, either in tandem solar cells as the acceptor to achieve a high V_{OC} [287], or in ternary solar cells as the third component to tune the morphology [135]. Although detailed stabilization effect was not clarified, there are few researches reporting that fullerene derivatives can simultaneously improve power conversion efficiency and device stability in polymer:nonfullerene solar cells [135,288,289], demonstrating that the fullerene molecule could play an important role in polymer:nonfullerene solar cells, and it is still worthwhile to investigate the stabilization effect of fullerene molecules.

### 7.2   Degradation of nonfullerene-based solar cells

Since the first report of high-performance A-D-A type NFA for polymer solar cells in 2015 [198], the power conversion efficiency of the NFA-based cells increased dramatically in the last few years and high PCE of over 18% was recently reported [290,291]. Direct comparison on the stability of roll-coated fullerene and nonfullerene solar cells revealed that the NFA-based cells showed better stability [292], indicating a promising application of NFA cells. Even though the degradation of NFA based cells was not fully investigated as has been done on the fullerene cells, various degradation pathways of the NFA cells were clarified, which include

(Figure 27):

(1) Intrinsic instability of NFA molecules owing to the C=C linker. Zhou *et al.* [293] reported that the C=C linker of the NFA molecules can be easily attacked by nucleophiles, such as organic amines, yielding the breaking of the C=C bond. Brabec *et al.* [294] compared the stability of the NFA molecules with different substituents on the terminal acceptor moiety, and results showed that the methyl groups increase the light induced decomposition of the NFA molecules, while the fluorine substituents enhance the stability of the NFA molecule against light illumination. The comparison on the decomposition of NFA molecules with a different π-conjugation core revealed that the conformation of the molecules plays an important role in determining the stability of the materials. Luke *et al.* [295] demonstrated that the structurally twisted O-IDFBR is more easily decomposed than the planar O-IDTBR. Recently, Li *et al.* [296] reported that structural confinement prevented the photoisomerization of NFAs at the molecular level and in condensed solid, helped enhancing the photochemical stabilities of molecules, as well as the corresponding OSCs, providing an effective guide line for developing high performance NFAs.

(2) Photon-induced decomposition of NFA at the metal oxide interface. Zhou *et al.* [297] reported that the NFA molecule IT-4F underwent decomposition on the ZnO surface under UV light illumination, as seen from the decrease of absorption intensity of the ZnO/IT-4F film. By mass spectrometry (MS) and NMR analyses, they confirmed that the decomposition of IT-4F mainly happened on the C=C linker between the central donor and the terminal acceptor moieties. Park *et al.* [298] also demonstrated that ITIC underwent photo-decomposition under light illumination owing to the open C=C bond. By comparing the stability difference of the NFA molecules on different ZnO surface, Ma *et al.* [299] demonstrated that the photo-decomposition rate of NFA under white light illumination is directly correlated to the light absorption ability of ZnO film. In combination with MS and electron spin resonance (ESR) measure, they proved that photon-generated hydroxyl radicals on the ZnO surface are the reactive species causing the decomposition of NFA molecules.

(3) Morphology changes of the photoactive layer. The nanoscale phase separation of the donor and the acceptor significantly influences the charge generation and transport. Therefore, the change of nano-morphology of the photoactive layer will cause performance changes of the cells [300]. Brabec *et al.* [262] demonstrated that the initial nano-morphology of the photoactive layer played an important role in determining the performance and stability of the cells. Under operation, reorganization of the conjugated polymer chain and the formation of acceptor domains will induce more traps within the photoactive layer, which will decrease the FF of the cells. By using co-solvent additive to tune the
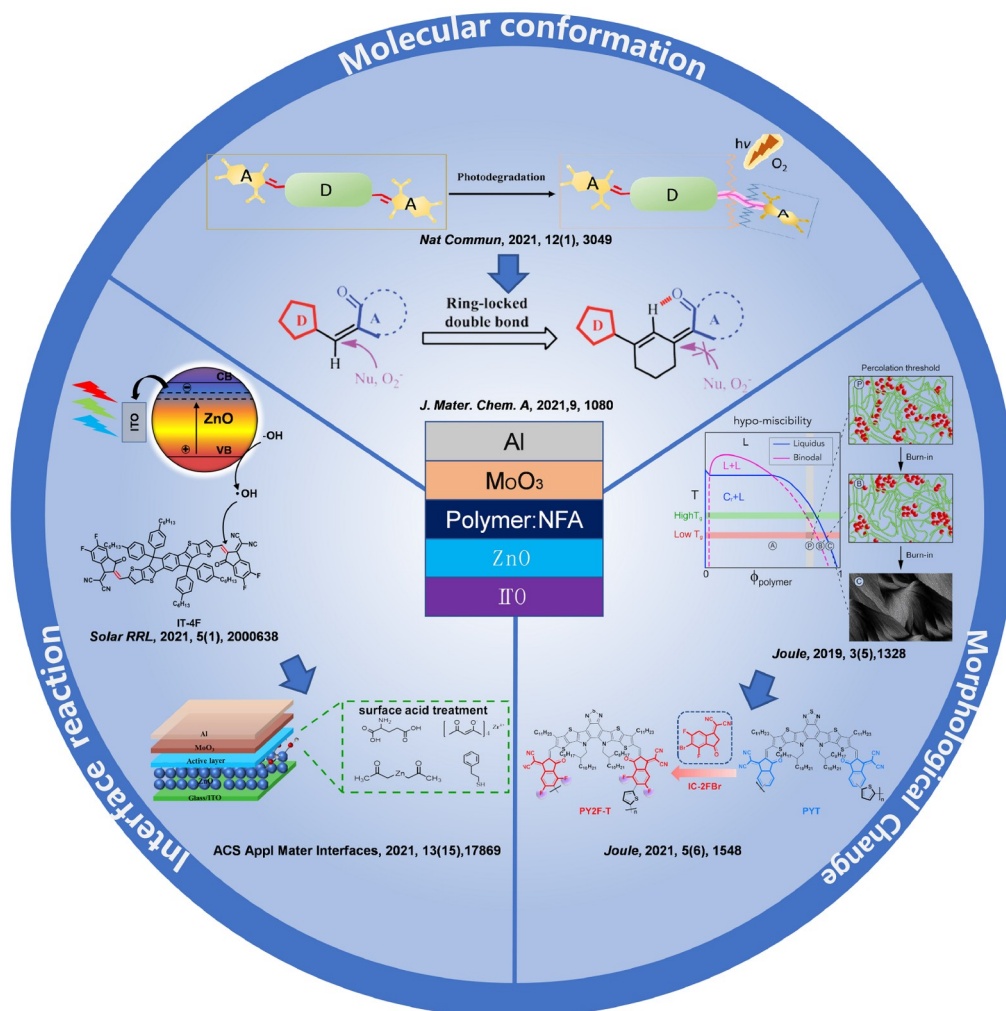
Figure 27 Degradation pathways and stability improvement methods for polymer:nonfullerene solar cells (color online).

morphology of the photoactive layer, the stability of the cells can be improved, demonstrating the device processing need to be carefully optimized. Xin *et al*. [301] demonstrated that the compatibility of the NFA molecules with the polymer matrix was also related to the fluorine atoms on the terminal acceptor moiety. They found that mF-ITIC showed the best compatibility with polymer matrix, and therefore showed the best performance stability, whereas the oF-ITIC showed the poorest stability owing to the worst compatibility. But nevertheless, owing to the close 2D planar molecular structure, the NFA molecules showed improved morphology stability than fullerene molecules. Upama *et al*. [302] demonstrated that NFA-based cells showed rather stable nanomorphology even under thermal annealing.

In response to the unstable C=C bond of the NFA molecules, reducing the concentration of nucleophiles should be able to increase the stability of the cells. For example, by tuning the pH value of the PEI aqueous solution, Zhou *et al*. [303] significantly increased the illumination stability of

NFA solar cells. Ma *et al*. [299,304] also reported the use of Lewis acid treatment on ZnO surface, which also significantly increase the stability of the NFA solar cells. Replacing high reactive ZnO with low photo-catalytic active SnO_2, or using more stable Y6 can also increased the stability of the NFA cells [297,303]. However, since the open C=C bond can be attacked by water/O_2 or other nucleophiles, fusing the C=C bond should be the best way to increase the stability of the polymer:NFA cells. Li *et al*. [305] reported the synthesis of a new NFA molecule with a ring-locked C=C bond, which showed improved intrinsic chemical and photochemical stability of acceptor molecules. Also, Zhu *et al*. [306] reported also the synthesis of a new electron acceptor, ITYM, which has an all-fused-ring structure. This type of all-fused-ring electron acceptor (AFRA) showed extraordinary stability against light illumination, demonstrating the stabilization effect of the fusing C=C bond strategy. Besides, Yao *et al*. [288] inserted a cross-linkable fullerene derivative (c-PCBSD) between the ZnO and active layer and doped it into
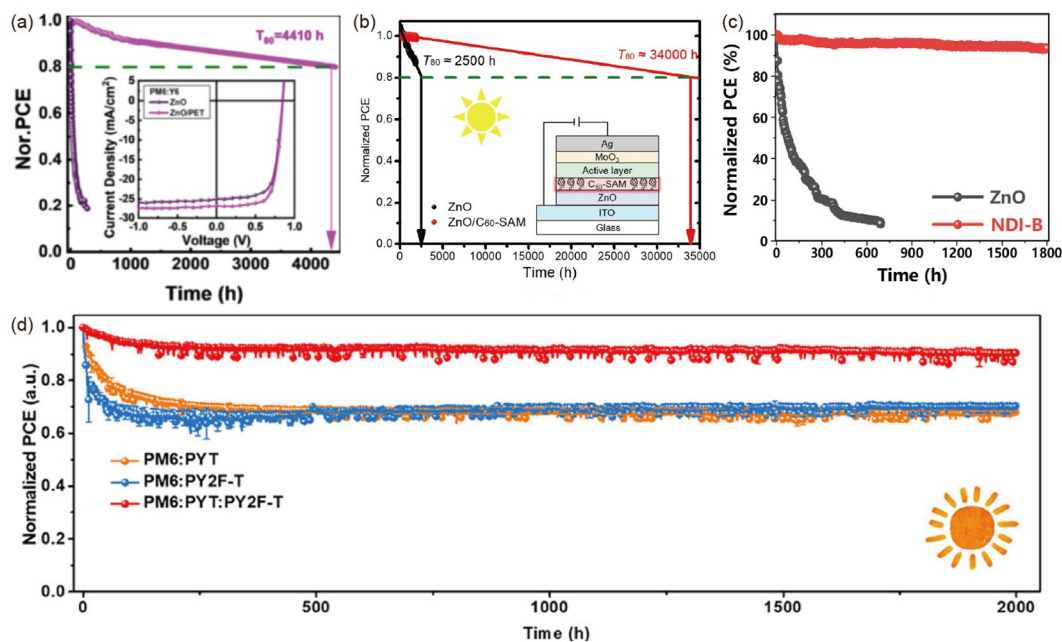
Figure 28 Stable polymer:nonfullerene solar cells with extrapolating lifetime over 4,000 h. (a) PCE decay of the PM6:Y6 inverted solar cells with the pristine ZnO and PET-treated ZnO ETLs [304]. (b) PCE decay of PTB7-Th:IEICO-4F-based inverted OSCs with ZnO and ZnO/C60-SAM ETLs [308]. (c) Photostability of the ZnO and NDI-B devices [310]. (d) Normalized PCEs expressed as a function of light-soaking time under MPP tracking [309] (color online).

the active layer of PM6:Y6, which not only isolated the reaction of ZnO and Y6, but also stabilized the morphology of the active layer, greatly improving the device stability. Studies have also shown that fullerene derivatives doped into the active layer can be used as a sacrificial reagent to undergo photocatalytic reaction with ZnO to improve device stability [289].

In short summary, various degradation pathways and detailed degradation mechanisms of polymer solar cells were clarified based on the research results in the last few years. With them, the methods to enhance the stability of the polymer solar cells were developed, and the overall intrinsic stability was greatly improved. For example, Yip *et al.* [307] reported a stable polymer solar cell based on PTB7-Th:EH-IDT, which showed a high PCE of 9.17% and a long operational lifetime (T_{80}) over 2,000 h. By ZnO surface treatment with PET, stable polymer solar cells with an extrapolating life-time of over 4,000 h were reported [304]. By surface modification of ZnO with a monolayer of fullerene, Yip *et al.* [308] reported also an extrapolating lifetime of over 20 years. Recently, Min *et al.* [309] demonstrated by using a third component of polymer PYT, the ternary all-polymer solar cell (all-PSC) exhibited an impressively high power conversion efficiency of 17.2% and the extrapolated T_{80} lifetime of 20,500 hfor the ternary system was determined (Figure 28). Besides, Hou *et al.* developed the device using NDI-B as a cathode interlayer (CIL) exhibiting a photovoltaic efficiency of 17.2% and retained 93% of its initial PCE after continuous illumination for 1,800 h, sug-

gesting that a T_{80} of over 1,800 h can be achieved under the operating conditions [310]. Although more investigations on the degradation mechanism of the high performance NFA solar cells are still needed, with more knowledge on the degradation mechanism of the cells, effective methods to improve device performance will be established and the lifetime of the polymer solar cells will be gradually increased.

8   Conclusions

In this review, the device engineering of OSCs is systemically summarized, including morphology characterization and optimization, devices physics, the fabrication of flexible and large-area OSCs, and the stability of OSCs. In addition, we also discussed the current challenge and problems of device engineering. We hope that this review could provide some useful perspectives for the development of OSCs device engineering and the in-depth study of device engineering will promote the commercial application of OSCs.

Conflict of interest   The authors declare no conflict of interest.

1   Liu Y, Liu B, Ma CQ, Huang F, Feng G, Chen H, Hou J, Yan L, Wei Q, Luo Q, Bao Q, Ma W, Liu W, Li W, Wan X, Hu X, Han Y, Li Y, Zhou Y, Zou Y, Chen Y, Li Y, Chen Y, Tang Z, Hu Z, Zhang ZG, Bo

Z. *Sci China Chem*, 2022, 65: 224–268

2   Cui Y, Xu Y, Yao H, Bi P, Hong L, Zhang J, Zu Y, Zhang T, Qin J, Ren J, Chen Z, He C, Hao X, Wei Z, Hou J. *Adv Mater*, 2021, 33: 2102420

3   Drummy LF, Davis RJ, Moore DL, Durstock M, Vaia RA, Hsu JWP. *Chem Mater*, 2011, 23: 907–912

4   Köntges W, Perkhun P, Kammerer J, Alkarsifi R, Würfel U, Margeat O, Videlot-Ackermann C, Simon JJ, Schröder RR, Ackermann J, Pfannmöller M. *Energy Environ Sci*, 2020, 13: 1259–1268

5   Du J, Hu K, Zhang J, Meng L, Yue J, Angunawela I, Yan H, Qin S, Kong X, Zhang Z, Guan B, Ade H, Li Y. *Nat Commun*, 2021, 12: 5264

6   Gao J, Wang J, An Q, Ma X, Hu Z, Xu C, Zhang X, Zhang F. *Sci China Chem*, 2020, 63: 83–91

7   Xu C, Ma X, Zhao Z, Jiang M, Hu Z, Gao J, Deng Z, Zhou Z, An Q, Zhang J, Zhang F. *Sol RRL*, 2021, 5: 2100175

8   Wang C, Araki T, Ade H. *Appl Phys Lett*, 2005, 87: 214109

9   Wang C, Araki T, Watts B, Harton S, Koga T, Basu S, Ade H. *J Vacuum Sci Tech A-Vacuum Surfs Films*, 2007, 25: 575–586

10   Hexemer A, Bras W, Glossinger J, Schaible E, Gann E, Kirian R, MacDowell A, Church M, Rude B, Padmore H. *J Phys-Conf Ser*, 2010, 247: 012007

11   Tsao HN, Cho DM, Park I, Hansen MR, Mavrinskiy A, Yoon DY, Graf R, Pisula W, Spiess HW, Müllen K. *J Am Chem Soc*, 2011, 133: 2605–2612

12   Seifrid M, Reddy GNM, Chmelka BF, Bazan GC. *Nat Rev Mater*, 2020, 5: 910–930

13   Geng SZ, Yang WT, Gao J, Li SX, Shi MM, Lau TK, Lu XH, Li CZ, Chen HZ. *Chin J Polym Sci*, 2019, 37: 1005–1014

14   Liu X, Wang X, Xiao Y, Yang Q, Guo X, Li C. *Adv Energy Mater*, 2020, 10: 1903650

15   Dai S, Zhou J, Chandrabose S, Shi Y, Han G, Chen K, Xin J, Liu K, Chen Z, Xie Z, Ma W, Yi Y, Jiang L, Hodgkiss JM, Zhan X. *Adv Mater*, 2020, 32: 2000645

16   Ma Y, Zhang M, Wan S, Yin P, Wang P, Cai D, Liu F, Zheng Q. *Joule*, 2021, 5: 197–209

17   Xu X, Feng K, Bi Z, Ma W, Zhang G, Peng Q. *Adv Mater*, 2019, 31: 1901872

18   Zhang ZG, Bai Y, Li Y. *Chin J Polym Sci*, 2020, 39: 1–13

19   Liu F, Wang D, Li JY, Xiao CY, Wu YG, Li WW, Fu GS. *Chin J Polym Sci*, 2020, 39: 43–50

20   Zhang Y, Wang Y, Ma R, Luo Z, Liu T, Kang SH, Yan H, Yuan Z, Yang C, Chen Y. *Chin J Polym Sci*, 2020, 38: 797–805

21   Biernat M, Dąbczyński P, Biernat P, Rysz J. *Chin J Polym Sci*, 2020, 38: 1025–1033

22   Ma L, Yao H, Wang J, Xu Y, Gao M, Zu Y, Cui Y, Zhang S, Ye L, Hou J. *Angew Chem Int Ed*, 2021, 60: 15988–15994

23   Lee S, Park KH, Lee J, Back H, Sung MJ, Lee J, Kim J, Kim H, Kim Y, Kwon S, Lee K. *Adv Energy Mater*, 2019, 9: 1900044

24   Ye L, Hu H, Ghasemi M, Wang T, Collins BA, Kim JH, Jiang K, Carpenter JH, Li H, Li Z, McAfee T, Zhao J, Chen X, Lai JLY, Ma T, Bredas JL, Yan H, Ade H. *Nat Mater*, 2018, 17: 253–260

25   Ye L, Li S, Liu X, Zhang S, Ghasemi M, Xiong Y, Hou J, Ade H. *Joule*, 2019, 3: 443–458

26   Nian L, Kan Y, Wang H, Gao K, Xu B, Rong Q, Wang R, Wang J, Liu F, Chen J, Zhou G, Russell TP, Jen AKY. *Energy Environ Sci*, 2018, 11: 3392–3399

27   Bi Z, Naveed HB, Sui X, Zhu Q, Xu X, Gou L, Liu Y, Zhou K, Zhang L, Zhang F, Liu X, Ma W. *Nano Energy*, 2019, 66: 104176

28   Li D, Zhu L, Liu X, Xiao W, Yang J, Ma R, Ding L, Liu F, Duan C, Fahlman M, Bao Q. *Adv Mater*, 2020, 32: 2002344

29   Mai J, Xiao Y, Zhou G, Wang J, Zhu J, Zhao N, Zhan X, Lu X. *Adv Mater*, 2018, 30: 1802888

30   Yu R, Yao H, Hong L, Qin Y, Zhu J, Cui Y, Li S, Hou J. *Nat Commun*, 2018, 9: 4645

31   Zhang L, Xu X, Lin B, Zhao H, Li T, Xin J, Bi Z, Qiu G, Guo S, Zhou K, Zhan X, Ma W. *Adv Mater*, 2018, 30: 1805041

32   Zhou Z, Xu S, Song J, Jin Y, Yue Q, Qian Y, Liu F, Zhang F, Zhu X. *Nat Energy*, 2018, 3: 952–959

33   Zhang S, Ye L, Zhang H, Hou J. *Mater Today*, 2016, 19: 533–543

34   Li MJ, Fan BB, Zhong WK, Zeng ZMY, Xu JK, Ying L. *Chin J Polym Sci*, 2020, 38: 791–796

35   Dong S, Jia T, Zhang K, Jing J, Huang F. *Joule*, 2020, 4: 2004–2016

36   Zhu C, Li Z, Zhong W, *et al. Chem Commun (Camb)*, 2021

37   Liu Y, Zhao J, Li Z, Mu C, Ma W, Hu H, Jiang K, Lin H, Ade H, Yan H. *Nat Commun*, 2014, 5: 5293

38   Zhao J, Li Y, Yang G, Jiang K, Lin H, Ade H, Ma W, Yan H. *Nat Energy*, 2016, 1: 15027

39   Xu X, Zhang G, Yu L, Li R, Peng Q. *Adv Mater*, 2019, 31: 1906045

40   Lin B, Zhang L, Zhao H, Xu X, Zhou K, Zhang S, Gou L, Fan B, Zhang L, Yan H, Gu X, Ying L, Huang F, Cao Y, Ma W. *Nano Energy*, 2019, 59: 277–284

41   Zhu L, Zhong W, Qiu C, Lyu B, Zhou Z, Zhang M, Song J, Xu J, Wang J, Ali J, Feng W, Shi Z, Gu X, Ying L, Zhang Y, Liu F. *Adv Mater*, 2019, 31: 1902899

42   Zhao H, Naveed HB, Lin B, Zhou X, Yuan J, Zhou K, Wu H, Guo R, Scheel MA, Chumakov A, Roth SV, Tang Z, Müller-Buschbaum P, Ma W. *Adv Mater*, 2020, 32: 2002302

43   Lin B, Zhou X, Zhao H, Yuan J, Zhou K, Chen K, Wu H, Guo R, Scheel MA, Chumakov A, Roth SV, Mao Y, Wang L, Tang Z, Müller-Buschbaum P, Ma W. *Energy Environ Sci*, 2020, 13: 2467–2479

44   van Franeker JJ, Turbiez M, Li W, Wienk MM, Janssen RAJ. *Nat Commun*, 2015, 6: 6229

45   Liang Q, Jiao X, Yan Y, Xie Z, Lu G, Liu J, Han Y. *Adv Funct Mater*, 2019, 29: 1807591

46   Li M, Liu F, Wan X, Ni W, Kan B, Feng H, Zhang Q, Yang X, Wang Y, Zhang Y, Shen Y, Russell TP, Chen Y. *Adv Mater*, 2015, 27: 6296–6302

47   Gao K, Deng W, Xiao L, Hu Q, Kan Y, Chen X, Wang C, Huang F, Peng J, Wu H, Peng X, Cao Y, Russell TP, Liu F. *Nano Energy*, 2016, 30: 639–648

48   McDowell C, Abdelsamie M, Toney MF, Bazan GC. *Adv Mater*, 2018, 30: 1707114

49   Chen J, Bi Z, Xu X, Zhang Q, Yang S, Guo S, Yan H, You W, Ma W. *Adv Sci*, 2019, 6: 1801560

50   Huang Y, Kramer EJ, Heeger AJ, Bazan GC. *Chem Rev*, 2014, 114: 7006–7043

51   Peet J, Soci C, Coffin RC, Nguyen TQ, Mikhailovsky A, Moses D, Bazan GC. *Appl Phys Lett*, 2006, 89: 252105

52   Peet J, Kim JY, Coates NE, Ma WL, Moses D, Heeger AJ, Bazan GC. *Nat Mater*, 2007, 6: 497–500

53   Rogers JT, Schmidt K, Toney MF, Kramer EJ, Bazan GC. *Adv Mater*, 2011, 23: 2284–2288

54   Ma X, Zeng A, Gao J, Hu Z, Xu C, Son JH, Jeong SY, Zhang C, Li M, Wang K, Yan H, Ma Z, Wang Y, Woo HY, Zhang F. *Natl Sci Rev*, 2021, 8: doi: 10.1093/nsr/nwaa305

55   Ma X, Wang J, An Q, Gao J, Hu Z, Xu C, Zhang X, Liu Z, Zhang F. *Nano Energy*, 2020, 70: 104496

56   Ghasemi M, Balar N, Peng Z, Hu H, Qin Y, Kim T, Rech JJ, Bidwell M, Mask W, McCulloch I, You W, Amassian A, Risko C, O′Connor BT, Ade H. *Nat Mater*, 2021, 20: 525–532

57   Pokuri BSS, Sit J, Wodo O, Baran D, Ameri T, Brabec CJ, Moule AJ, Ganapathysubramanian B. *Adv Energy Mater*, 2017, 7: 1701269

58   Meng X, Zhang L, Xie Y, Hu X, Xing Z, Huang Z, Liu C, Tan L, Zhou W, Sun Y, Ma W, Chen Y. *Adv Mater*, 2019, 31: 1903649

59   Tada A, Geng Y, Wei Q, Hashimoto K, Tajima K. *Nat Mater*, 2011, 10: 450–455

60   Scharber M , Mühlbacher D, Koppe M, Denk P, Waldauf C, Heeger A , Brabec C . *Adv Mater*, 2006, 18: 789–794

61   Wang C, Ouyang L, Xu X, Braun S, Liu X, Fahlman M. *Sol RRL*, 2018, 2: 1800122

62   Liu J, Chen S, Qian D, Gautam B, Yang G, Zhao J, Bergqvist J, Zhang F, Ma W, Ade H, Inganäs O, Gundogdu K, Gao F, Yan H. *Nat*

Energy, 2016, 1: 16089

63 Classen A, Chochos CL, Lüer L, Gregoriou VG, Wortmann J, Osvet A, Forberich K, McCulloch I, Heumüller T, Brabec CJ. *Nat Energy*, 2020, 5: 711–719

64 Braun S, Salaneck WR, Fahlman M. *Adv Mater*, 2009, 21: 1450–1472

65 Verlaak S, Beljonne D, Cheyns D, Rolin C, Linares M, Castet FÃÃ, Cornil JÃ, Heremans P. *Adv Funct Mater*, 2009, 19: 3809–3814

66 Zhang Q, Liu X, Jiao F, Braun S, Jafari MJ, Crispin X, Ederth T, Fahlman M. *J Mater Chem C*, 2017, 5: 275–281

67 Sworakowski J, Lipiński J, Janus K. *Org Electron*, 2016, 33: 300–310

68 Sworakowski J, Janus K. *Org Electron*, 2017, 48: 46–52

69 Bao Q, Liu X, Braun S, Li Y, Tang J, Duan C, Fahlman M. *Sol RRL*, 2017, 1: 1700142

70 Bao Q, Sandberg O, Dagnelund D, Sandén S, Braun S, Aarnio H, Liu X, Chen WM, Österbacka R, Fahlman M. *Adv Funct Mater*, 2014, 24: 6309–6316

71 Deschler F, Da Como E, Limmer T, Tautz R, Godde T, Bayer M, von Hauff E, Yilmaz S, Allard S, Scherf U, Feldmann J. *Phys Rev Lett*, 2011, 107: 127402

72 Akaike K, Koch N, Heimel G, Oehzelt M. *Adv Mater Interfaces*, 2015, 2: 1500232

73 Li Y, Li P, Lu ZH. *Adv Mater*, 2017, 29: 1700414

74 Bussolotti F, Yang J, Hinderhofer A, Huang Y, Chen W, Kera S, Wee ATS, Ueno N. *Phys Rev B*, 2014, 89: 115319

75 Yang JP, Bussolotti F, Kera S, Ueno N. *J Phys D-Appl Phys*, 2017, 50: 423002

76 Guo X, Zhang Y, Liu X, Braun S, Wang Z, Li B, Li Y, Duan C, Fahlman M, Tang J, Fang J, Bao Q. *Org Electron*, 2018, 59: 15–20

77 Wang C, Luo D, Gao Y, Wang G, Wang C, Ma P, Li H, Wen S, Dong W, Ruan S. *J Phys Chem C*, 2019, 123: 16546–16555

78 Huang S, Duan L, Zhang D. *J Mater Chem A*, 2020, 8: 18792–18801

79 Bao Q, Liu X, Xia Y, Gao F, Kauffmann LD, Margeat O, Ackermann J, Fahlman M. *J Mater Chem A*, 2014, 2: 17676–17682

80 Raoufi M, Hörmann U, Ligorio G, Hildebrandt J, Pätzel M, Schultz T, Perdigon L, Koch N, List-Kratochvil E, Hecht S, Neher D. *Phys Status Solidi A*, 2020, 217: 1900876

81 Sun Z, Shi S, Bao Q, Liu X, Fahlman M. *Adv Mater Interfaces*, 2015, 2: 1400527

82 van Reenen S, Kouijzer S, Janssen RAJ, Wienk MM, Kemerink M. *Adv Mater Interfaces*, 2014, 1: 1400189

83 Bao Q, Liu X, Wang E, Fang J, Gao F, Braun S, Fahlman M. *Adv Mater Interfaces*, 2015, 2: 1500204

84 Cao B, He X, Fetterly CR, Olsen BC, Luber EJ, Buriak JM. *ACS Appl Mater Interfaces*, 2016, 8: 18238–18248

85 Oehzelt M, Koch N, Heimel G. *Nat Commun*, 2014, 5: 4174

86 Zheng Z, Hu Q, Zhang S, Zhang D, Wang J, Xie S, Wang R, Qin Y, Li W, Hong L, Liang N, Liu F, Zhang Y, Wei Z, Tang Z, Russell TP, Hou J, Zhou H. *Adv Mater*, 2018, 30: 1801801

87 Lin Y, Nugraha MI, Firdaus Y, Scaccabarozzi AD, Aniés F, Emwas AH, Yengel E, Zheng X, Liu J, Wahyudi W, Yarali E, Faber H, Bakr OM, Tsetseris L, Heeney M, Anthopoulos TD. *ACS Energy Lett*, 2020, 5: 3663–3671

88 Zhang M, Zhu L, Zhou G, Hao T, Qiu C, Zhao Z, Hu Q, Larson BW, Zhu H, Ma Z, Tang Z, Feng W, Zhang Y, Russell TP, Liu F. *Nat Commun*, 2021, 12: 309

89 Shockley W, Queisser HJ. *J Appl Phys*, 1961, 32: 510–519

90 Kirchartz T, Taretto K, Rau U. *J Phys Chem C*, 2009, 113: 17958–17966

91 Vandewal K, Ma Z, Bergqvist J, Tang Z, Wang E, Henriksson P, Tvingstedt K, Andersson MR, Zhang F, Inganäs O. *Adv Funct Mater*, 2012, 22: 3480–3490

92 Ma Z, Sun W, Himmelberger S, Vandewal K, Tang Z, Bergqvist J, Salleo A, Andreasen JW, Inganäs O, Andersson MR, Müller C, Zhang F, Wang E. *Energy Environ Sci*, 2014, 7: 361–369

93 Vandewal K, Tvingstedt K, Gadisa A, Inganäs O, Manca JV. *Nat*

Mater, 2009, 8: 904–909

94 Vandewal K, Tvingstedt K, Gadisa A, Inganäs O, Manca JV. *Phys Rev B*, 2010, 81: 125204

95 Qian D, Zheng Z, Yao H, Tress W, Hopper TR, Chen S, Li S, Liu J, Chen S, Zhang J, Liu XK, Gao B, Ouyang L, Jin Y, Pozina G, Buyanova IA, Chen WM, Inganäs O, Coropceanu V, Bredas JL, Yan H, Hou J, Zhang F, Bakulin AA, Gao F. *Nat Mater*, 2018, 17: 703–709

96 Liu S, Yuan J, Deng W, Luo M, Xie Y, Liang Q, Zou Y, He Z, Wu H, Cao Y. *Nat Photonics*, 2020, 14: 300–305

97 Cheng P, Li G, Zhan X, Yang Y. *Nat Photon*, 2018, 12: 131–142

98 Benduhn J, Tvingstedt K, Piersimoni F, Ullbrich S, Fan Y, Tropiano M, McGarry KA, Zeika O, Riede MK, Douglas CJ, Barlow S, Marder SR, Neher D, Spoltore D, Vandewal K. *Nat Energy*, 2017, 2: 17053

99 Tang Z, Tress W, Bao Q, Jafari MJ, Bergqvist J, Ederth T, Andersson MR, Inganäs O. *Adv Energy Mater*, 2014, 4: 1400643

100 Tress W, Corvers S, Leo K, Riede M. *Adv Energy Mater*, 2013, 3: 873–880

101 Koster LJA, Smits ECP, Mihailetchi VD, Blom PWM. *Phys Rev B*, 2005, 72: 085205

102 Zhou Y, Fuentes-Hernandez C, Shim J, Meyer J, Giordano AJ, Li H, Winget P, Papadopoulos T, Cheun H, Kim J, Fenoll M, Dindar A, Haske W, Najafabadi E, Khan TM, Sojoudi H, Barlow S, Graham S, Brédas JL, Marder SR, Kahn A, Kippelen B. *Science*, 2012, 336: 327–332

103 He C, Zhong C, Wu H, Yang R, Yang W, Huang F, Bazan GC, Cao Y. *J Mater Chem*, 2010, 20: 2617–2622

104 Vandewal K. *Annu Rev Phys Chem*, 2016, 67: 113–133

105 Liu H, Li M, Wu H, Wang J, Ma Z, Tang Z. *J Mater Chem A*, 2021, 9: 19770–19777

106 Eisner FD, Azzouzi M, Fei Z, Hou X, Anthopoulos TD, Dennis TJS, Heeney M, Nelson J. *J Am Chem Soc*, 2019, 141: 6362–6374

107 Azzouzi M, Yan J, Kirchartz T, Liu K, Wang J, Wu H, Nelson J. *Phys Rev X*, 2018, 8: 031055

108 Li G, Zhu R, Yang Y. *Nat Photon*, 2012, 6: 153–161

109 Hashemi SA, Ramakrishna S, Aberle AG. *Energy Environ Sci*, 2020, 13: 685–743

110 Park S, Heo SW, Lee W, Inoue D, Jiang Z, Yu K, Jinno H, Hashizume D, Sekino M, Yokota T, Fukuda K, Tajima K, Someya T. *Nature*, 2018, 561: 516–521

111 Li Y, Xu G, Cui C, Li Y. *Adv Energy Mater*, 2018, 8: 1701791

112 Qin J, Lan L, Chen S, Huang F, Shi H, Chen W, Xia H, Sun K, Yang C. *Adv Funct Mater*, 2020, 30: 2002529

113 Wang J, Wang C, Cai P, Luo Y, Cui Z, Loh XJ, Chen X. *ACS Nano*, 2021, 15: 18671–18678

114 Qu T, Zuo L, Chen J, Shi X, Zhang T, Li L, Shen K, Ren H, Wang S, Xie F, Li Y, Jen AK, Tang J. *Adv Opt Mater*, 2020, 8: 2000669

115 Seo JH, Hwang I, Um HD, Lee S, Lee K, Park J, Shin H, Kwon TH, Kang SJ, Seo K. *Adv Mater*, 2017, 29: 1701479

116 Lee J, Sun C, Ma BS, Kim HJ, Wang C, Ryu JM, Lim C, Kim T, Kim Y, Kwon S, Kim BJ. *Adv Energy Mater*, 2021, 11: 2003367

117 Zhang J, Xue R, Xu G, Chen W, Bian GQ, Wei C, Li J, Li Y. *Adv Funct Mater*, 2018, 28: 1705847

118 Wen X, Fang S, Xu Y, Zheng N, Liu L, Xie Z, Würthner F. *ACS Appl Mater Interfaces*, 2019, 11: 34151–34157

119 Zhang YX, Fang J, Li W, Shen Y, Chen JD, Li Y, Gu H, Pelivani S, Zhang M, Li Y, Tang JX. *ACS Nano*, 2019, 13: 4686–4694

120 Song W, Fanady B, Peng R, Hong L, Wu L, Zhang W, Yan T, Wu T, Chen S, Ge Z. *Adv Energy Mater*, 2020, 10: 2000136

121 Seo KW, Lee J, Jo J, Cho C, Lee JY. *Adv Mater*, 2019, 31: 1902447

122 Meng W, Ge R, Li Z, Tong J, Liu T, Zhao Q, Xiong S, Jiang F, Mao L, Zhou Y. *ACS Appl Mater Interfaces*, 2015, 7: 14089–14094

123 Tong J, Xiong S, Zhou Y, Mao L, Min X, Li Z, Jiang F, Meng W, Qin F, Liu T, Ge R, Fuentes-Hernandez C, Kippelen B, Zhou Y. *Mater Horiz*, 2016, 3: 452–459

124 Dong X, Shi P, Sun L, Li J, Qin F, Xiong S, Liu T, Jiang X, Zhou Y.

J Mater Chem A, 2019, 7: 1989–1995

125 Koo D, Jung S, Seo J, Jeong G, Choi Y, Lee J, Lee SM, Cho Y, Jeong M, Lee J, Oh J, Yang C, Park H. *Joule*, 2020, 4: 1021–1034

126 MacDonald WA, Looney MK, MacKerron D, Eveson R, Adam R, Hashimoto K, Rakos K. *J Soc Inf Display*, 2007, 15: 1075

127 Zardetto V, Brown TM, Reale A, di Carlo A. *J Polym Sci B Polym Phys*, 2011, 49: 638–648

128 Asare J, Agyei-Tuffour B, Amonoo EA, Dodoo-Arhin D, Nyankson E, Mensah B, Oyewole OO, Yaya A, Onwona-Agyeman B. *Cogent Engineering*, 2020, 7: 1829274

129 Choi MC, Kim Y, Ha CS. *Prog Polym Sci*, 2008, 33: 581–630

130 Kimura H, Fukuda K, Jinno H, Park S, Saito M, Osaka I, Takimiya K, Umezu S, Someya T. *Adv Mater*, 2019, 31: 1808033

131 Hasegawa M, Horie K. *Prog Polym Sci*, 2001, 26: 259–335

132 Bitla Y, Chu YH. *FlatChem*, 2017, 3: 26–42

133 Yi C, Li W, Shi S, He K, Ma P, Chen M, Yang C. *Sol Energy*, 2020, 195: 340–354

134 Zhou N, Buchholz DB, Zhu G, Yu X, Lin H, Facchetti A, Marks TJ, Chang RPH. *Adv Mater*, 2014, 26: 1098–1104

135 Yan T, Song W, Huang J, Peng R, Huang L, Ge Z. *Adv Mater*, 2019, 31: 1902210

136 Jeon I, Cui K, Chiba T, Anisimov A, Nasibulin AG, Kauppinen EI, Maruyama S, Matsuo Y. *J Am Chem Soc*, 2015, 137: 7982–7985

137 Zhao G, Wang W, Bae TS, Lee SG, Mun CW, Lee S, Yu H, Lee GH, Song M, Yun J. *Nat Commun*, 2015, 6: 8830

138 Wang G, Zhang J, Yang C, Wang Y, Xing Y, Adil MA, Yang Y, Tian L, Su W, Shang W, Lu K, Shuai Z, Wei Z. *Adv Mater*, 2020, 32: 2005153

139 Sun Y, Chang M, Meng L, Wan X, Gao H, Zhang Y, Zhao K, Sun Z, Li C, Liu S, Wang H, Liang J, Chen Y. *Nat Electron*, 2019, 2: 513–520

140 Chen X, Xu G, Zeng G, Gu H, Chen H, Xu H, Yao H, Li Y, Hou J, Li Y. *Adv Mater*, 2020, 32: 1908478

141 Hau SK, Yip HL, Baek NS, Zou J, O'Malley K, Jen AKY. *Appl Phys Lett*, 2008, 92: 253301

142 Boehme M, Charton C. *Surf Coatings Tech*, 2005, 200: 932–935

143 Vosgueritchian M, Lipomi DJ, Bao Z. *Adv Funct Mater*, 2012, 22: 421–428

144 Song W, Fan X, Xu B, Yan F, Cui H, Wei Q, Peng R, Hong L, Huang J, Ge Z. *Adv Mater*, 2018, 30: 1800075

145 Kim N, Kang H, Lee JH, Kee S, Lee SH, Lee K. *Adv Mater*, 2015, 27: 2317–2323

146 Kim N, Kee S, Lee SH, Lee BH, Kahng YH, Jo YR, Kim BJ, Lee K. *Adv Mater*, 2014, 26: 2268–2272

147 Wang X, Jin H, Nagiri RCR, Poliquit BZL, Subbiah J, Jones DJ, Kopidakis N, Burn PL, Yu J. *Sol RRL*, 2019, 3: 1800286

148 Tavakoli MM, Azzellino G, Hempel M, Lu A, MartinMartinez FJ, Zhao J, Yeo J, Palacios T, Buehler MJ, Kong J. *Adv Funct Mater*, 2020, 30: 2001924

149 Pasquier AD, Unalan HE, Kanwal A, Miller S, Chhowalla M. *Appl Phys Lett*, 2005, 87: 203511

150 Rowell MW, Topinka MA, McGehee MD, Prall HJ, Dennler G, Sariciftci NS, Hu L, Gruner G. *Appl Phys Lett*, 2006, 88: 233506

151 Wong CC, Smith HI, Thompson CV. *Appl Phys Lett*, 1986, 48: 335–337

152 Li H, Liu X, Wang W, Lu Y, Huang J, Li J, Xu J, Fan P, Fang J, Song W. *Sol RRL*, 2018, 2: 1800123

153 Mao L, Chen Q, Li Y, Li Y, Cai J, Su W, Bai S, Jin Y, Ma CQ, Cui Z, Chen L. *Nano Energy*, 2014, 10: 259–267

154 Czolk J, Landerer D, Koppitz M, Nass D, Colsmann A. *Adv Mater Technol*, 2016, 1: 1600184

155 Jiang Z, Fukuda K, Xu X, Park S, Inoue D, Jin H, Saito M, Osaka I, Takimiya K, Someya T. *Adv Mater*, 2018, 30: 1707526

156 Lee JY, Connor ST, Cui Y, Peumans P. *Nano Lett*, 2008, 8: 689–692

157 Ge Y, Liu J, Liu X, Hu J, Duan X, Duan X. *J Am Chem Soc*, 2019, 141: 12251–12257

158 Yim JH, Joe S, Pang C, Lee KM, Jeong H, Park JY, Ahn YH, de Mello JC, Lee S. *ACS Nano*, 2014, 8: 2857–2863

159 Zeng G, Zhang J, Chen X, Gu H, Li Y, Li Y. *Sci China Chem*, 2019, 62: 851–858

160 Song M, Park JH, Kim CS, Kim DH, Kang YC, Jin SH, Jin WY, Kang JW. *Nano Res*, 2014, 7: 1370–1379

161 Jiang Z, Fukuda K, Huang W, Park S, Nur R, Nayeem MOG, Yu K, Inoue D, Saito M, Kimura H, Yokota T, Umezu S, Hashizume D, Osaka I, Takimiya K, Someya T. *Adv Funct Mater*, 2019, 29: 1808378

162 Sun Y, Meng L, Wan X, Guo Z, Ke X, Sun Z, Zhao K, Zhang H, Li C, Chen Y. *Adv Funct Mater*, 2021, 31: 2010000

163 Hu L, Liu Y, Mao L, Xiong S, Sun L, Zhao N, Qin F, Jiang Y, Zhou Y. *J Mater Chem A*, 2018, 6: 2273–2278

164 Hu L, Xiong S, Wang W, Sun L, Qin F, Zhou Y. *J Phys Chem C*, 2020, 124: 2307–2312

165 Xiong S, Hu L, Hu L, Sun L, Qin F, Liu X, Fahlman M, Zhou Y. *Adv Mater*, 2019, 31: 1806616

166 Qin F, Wang W, Sun L, Jiang X, Hu L, Xiong S, Liu T, Dong X, Li J, Jiang Y, Hou J, Fukuda K, Someya T, Zhou Y. *Nat Commun*, 2020, 11: 4508

167 Qin F, Sun L, Chen H, Liu Y, Lu X, Wang W, Liu T, Dong X, Jiang P, Jiang Y, Wang L, Zhou Y. *Adv Mater*, 2021, 33: 2103017

168 Jiang Y, Liu T, Zhou Y. *Adv Funct Mater*, 2020, 30: 2006213

169 Wan J, Fan X, Huang H, Wang J, Zhang Z, Fang J, Yan F. *J Mater Chem A*, 2020, 8: 21007–21015

170 Zhang W, Song W, Huang J, Huang L, Yan T, Ge J, Peng R, Ge Z. *J Mater Chem A*, 2019, 7: 22021–22028

171 Root SE, Savagatrup S, Printz AD, Rodriquez D, Lipomi DJ. *Chem Rev*, 2017, 117: 6467–6499

172 Han J, Bao F, Huang D, Wang X, Yang C, Yang R, Jian X, Wang J, Bao X, Chu J. *Adv Funct Mater*, 2020, 30: 2003654

173 Huang W, Jiang Z, Fukuda K, Jiao X, McNeill CR, Yokota T, Someya T. *Joule*, 2020, 4: 128–141

174 Lee C, Lee S, Kim GU, Lee W, Kim BJ. *Chem Rev*, 2019, 119: 8028–8086

175 Kim T, Kim JH, Kang TE, Lee C, Kang H, Shin M, Wang C, Ma B, Jeong U, Kim TS, Kim BJ. *Nat Commun*, 2015, 6: 8547

176 Chen S, Jung S, Cho HJ, Kim NH, Jung S, Xu J, Oh J, Cho Y, Kim H, Lee B, An Y, Zhang C, Xiao M, Ki H, Zhang ZG, Kim JY, Li Y, Park H, Yang C. *Angew Chem Int Ed*, 2018, 57: 13277–13282

177 Fan Q, Su W, Chen S, Kim W, Chen X, Lee B, Liu T, Méndez-Romero UA, Ma R, Yang T, Zhuang W, Li Y, Li Y, Kim TS, Hou L, Yang C, Yan H, Yu D, Wang E. *Joule*, 2020, 4: 658–672

178 Zhang L, Jia T, Pan L, Wu B, Wang Z, Gao K, Liu F, Duan C, Huang F, Cao Y. *Sci China Chem*, 2021, 64: 408–412

179 Fukuda K, Yu K, Someya T. *Adv Energy Mater*, 2020, 10: 2000765

180 Kim DH, Ahn JH, Choi WM, Kim HS, Kim TH, Song J, Huang YY, Liu Z, Lu C, Rogers JA. *Science*, 2008, 320: 507–511

181 Fukuda K, Sekine T, Shiwaku R, Morimoto T, Kumaki D, Tokito S. *Sci Rep*, 2016, 6: 27450

182 Kaltenbrunner M, White MS, Głowacki ED, Sekitani T, Someya T, Sariciftci NS, Bauer S. *Nat Commun*, 2012, 3: 770

183 Jinno H, Fukuda K, Xu X, Park S, Suzuki Y, Koizumi M, Yokota T, Osaka I, Takimiya K, Someya T. *Nat Energy*, 2017, 2: 780–785

184 Chang SY, Cheng P, Li G, Yang Y. *Joule*, 2018, 2: 1039–1054

185 Traverse CJ, Pandey R, Barr MC, Lunt RR. *Nat Energy*, 2017, 2: 849–860

186 Yu R, Yao H, Hou J. *Adv Energy Mater*, 2018, 8: 1702814

187 Hou J, Inganäs O, Friend RH, Gao F. *Nat Mater*, 2018, 17: 119–128

188 Liu Y, Lu H, Li M, Zhang Z, Feng S, Xu X, Wu Y, Bo Z. *Macromolecules*, 2018, 51: 8646–8651

189 Kini GP, Jeon SJ, Moon DK. *Adv Funct Mater*, 2021, 31: 2007931

190 Hu Z, Wang J, Wang Z, Gao W, An Q, Zhang M, Ma X, Wang J, Miao J, Yang C, Zhang F. *Nano Energy*, 2019, 55: 424–432

191 Hu Z, Wang J, Ma X, Gao J, Xu C, Wang X, Zhang X, Wang Z, Zhang F. *J Mater Chem A*, 2021, 9: 6797–6804

192 Xu C, Jin K, Xiao Z, Zhao Z, Ma X, Wang X, Li J, Xu W, Zhang S,

Ding L, Zhang F. *Adv Funct Mater*, 2021, 31: 2107934

193 Dou L, You J, Yang J, Chen CC, He Y, Murase S, Moriarty T, Emery K, Li G, Yang Y. *Nat Photon*, 2012, 6: 180–185

194 Chen CC, Dou L, Zhu R, Chung CH, Song TB, Zheng YB, Hawks S, Li G, Weiss PS, Yang Y. *ACS Nano*, 2012, 6: 7185–7190

195 Chen J, Li G, Zhu Q, Guo X, Fan Q, Ma W, Zhang M. *J Mater Chem A*, 2019, 7: 3745–3751

196 Su W, Fan Q, Guo X, Wu J, Zhang M, Li Y. *Phys Chem Chem Phys*, 2019, 21: 10660–10666

197 Chang CY, Zuo L, Yip HL, Li Y, Li CZ, Hsu CS, Cheng YJ, Chen H, Jen AKY. *Adv Funct Mater*, 2013, 23: 5084–5090

198 Lin Y, Wang J, Zhang ZG, Bai H, Li Y, Zhu D, Zhan X. *Adv Mater*, 2015, 27: 1170–1174

199 Wang W, Yan C, Lau TK, Wang J, Liu K, Fan Y, Lu X, Zhan X. *Adv Mater*, 2017, 29: 1701308

200 Cui Y, Yang C, Yao H, Zhu J, Wang Y, Jia G, Gao F, Hou J. *Adv Mater*, 2017, 29: 1703080

201 Li X, Meng H, Shen F, Su D, Huo S, Shan J, Huang J, Zhan C. *Dyes Pigments*, 2019, 166: 196–202

202 Yuan J, Zhang Y, Zhou L, Zhang G, Yip HL, Lau TK, Lu X, Zhu C, Peng H, Johnson PA, Leclerc M, Cao Y, Ulanski J, Li Y, Zou Y. *Joule*, 2019, 3: 1140–1151

203 Hu Z, Wang Z, An Q, Zhang F. *Sci Bull*, 2020, 65: 131–137

204 Wang D, Qin R, Zhou G, Li X, Xia R, Li Y, Zhan L, Zhu H, Lu X, Yip HL, Chen H, Li CZ. *Adv Mater*, 2020, 32: 2001621

205 Yin P, Yin Z, Ma Y, Zheng Q. *Energy Environ Sci*, 2020, 13: 5177–5185

206 Luo M, Zhao C, Yuan J, Hai J, Cai F, Hu Y, Peng H, Bai Y, Tan Z, Zou Y. *Mater Chem Front*, 2019, 3: 2483–2490

207 Sun C, Xia R, Shi H, Yao H, Liu X, Hou J, Huang F, Yip HL, Cao Y. *Joule*, 2018, 2: 1816–1826

208 Zhang J, Xu G, Tao F, Zeng G, Zhang M, Yang YM, Li Y, Li Y. *Adv Mater*, 2019, 31: 1807159

209 Strohm S, Machui F, Langner S, Kubis P, Gasparini N, Salvador M, McCulloch I, Egelhaaf HJ, Brabec CJ. *Energy Environ Sci*, 2018, 11: 2225–2234

210 Wang D, Liu H, Li Y, Zhou G, Zhan L, Zhu H, Lu X, Chen H, Li CZ. *Joule*, 2021, 5: 945–957

211 Liu Y, Cheng P, Li T, Wang R, Li Y, Chang SY, Zhu Y, Cheng HW, Wei KH, Zhan X, Sun B, Yang Y. *ACS Nano*, 2019, 13: 1071–1077

212 Wang H, Lu H, Chen Y, Zhang A, Liu Y, Li D, Liu Y, Xu X, Bo Z. *Adv Energy Mater*, 2022, 12: 2104028

213 Wang Y, Wang X, Lin B, Bi Z, Zhou X, Naveed HB, Zhou K, Yan H, Tang Z, Ma W. *Adv Energy Mater*, 2020, 10: 2000826

214 Lee J, Seo Y, Kwon S, Kim D, Jang S, Jung H, Lee Y, Weerasinghe H, Kim T, Kim JY, Vak D, Na S. *Adv Energy Mater*, 2019, 9: 1901805

215 Khim D, Han H, Baeg KJ, Kim J, Kwak SW, Kim DY, Noh YY. *Adv Mater*, 2013, 25: 4302–4308

216 Xing Z, Meng X, Sun R, Hu T, Huang Z, Min J, Hu X, Chen Y. *Adv Funct Mater*, 2020, 30: 2000417

217 Sun R, Wu Q, Guo J, Wang T, Wu Y, Qiu B, Luo Z, Yang W, Hu Z, Guo J, Shi M, Yang C, Huang F, Li Y, Min J. *Joule*, 2020, 4: 407–419

218 Xu W, Ma X, Son JH, Jeong SY, Niu L, Xu C, Zhang S, Zhou Z, Gao J, Woo HY, Zhang J, Wang J, Zhang F. *Small*, 2022, 18: 2104215

219 Diao Y, Zhou Y, Kurosawa T, Shaw L, Wang C, Park S, Guo Y, Reinspach JA, Gu K, Gu X, Tee BCK, Pang C, Yan H, Zhao D, Toney MF, Mannsfeld SCB, Bao Z. *Nat Commun*, 2015, 6: 7955

220 Ro HW, Downing JM, Engmann S, Herzing AA, DeLongchamp DM, Richter LJ, Mukherjee S, Ade H, Abdelsamie M, Jagadamma LK, Amassian A, Liu Y, Yan H. *Energy Environ Sci*, 2016, 9: 2835–2846

221 Dong S, Zhang K, Xie B, Xiao J, Yip HL, Yan H, Huang F, Cao Y. *Adv Energy Mater*, 2019, 9: 1802832

222 Zhang L, Zhao H, Yuan J, Lin B, Xing Z, Meng X, Ke L, Hu X, Ma W, Yuan Y. *Org Electron*, 2020, 83: 105771

223 Dong S, Zhang K, Jia T, Zhong W, Wang X, Huang F, Cao Y. *EcoMat*, 2019, 1: e12006

224 Wan J, Zhang L, He Q, Liu S, Huang B, Hu L, Zhou W, Chen Y. *Adv Funct Mater*, 2020, 30: 1909760

225 Mao L, Tong J, Xiong S, Jiang F, Qin F, Meng W, Luo B, Liu Y, Li Z, Jiang Y, Fuentes-Hernandez C, Kippelen B, Zhou Y. *J Mater Chem A*, 2017, 5: 3186–3192

226 Cui Y, Yao H, Hong L, Zhang T, Tang Y, Lin B, Xian K, Gao B, An C, Bi P, Ma W, Hou J. *Natl Sci Rev*, 2020, 7: 1239–1246

227 Ma L, Zhang S, Yao H, Xu Y, Wang J, Zu Y, Hou J. *ACS Appl Mater Interfaces*, 2020, 12: 18777–18784

228 Zhang J, Zhao Y, Fang J, Yuan L, Xia B, Wang G, Wang Z, Zhang Y, Ma W, Yan W, Su W, Wei Z. *Small*, 2017, 13: 1700388

229 Ma L, Xu Y, Zu Y, Liao Q, Xu B, An C, Zhang S, Hou J. *Sci China Chem*, 2019, 63: 21–27

230 Liu S, Chen D, Hu X, Xing Z, Wan J, Zhang L, Tan L, Zhou W, Chen Y. *Adv Funct Mater*, 2020, 30: 2003223

231 Ji G, Zhao W, Wei J, Yan L, Han Y, Luo Q, Yang S, Hou J, Ma CQ. *J Mater Chem A*, 2019, 7: 212–220

232 Lin Y, Yu L, Xia Y, Firdaus Y, Dong S, Müller C, Inganäs O, Huang F, Anthopoulos TD, Zhang F, Hou L. *Sol RRL*, 2019, 3: 1900179

233 Yang J, Lin Y, Zheng W, Liu A, Cai W, Yu X, Zhang F, Liang Q, Wu H, Qin D, Hou L. *ACS Appl Mater Interfaces*, 2018, 10: 22485–22494

234 Jiang X, Sun L, Wang W, Qin F, Xie C, Hu L, Zhou Y. *J Mater Chem A*, 2020, 8: 69–76

235 Han Y, Chen X, Wei J, Ji G, Wang C, Zhao W, Lai J, Zha W, Li Z, Yan L, Gu H, Luo Q, Chen Q, Chen L, Hou J, Su W, Ma CQ. *Adv Sci*, 2019, 6: 1901490

236 Wang Z, Han Y, Yan L, Gong C, Kang J, Zhang H, Sun X, Zhang L, Lin J, Luo Q, Ma C-. *Adv Funct Mater*, 2021, 31: 2007276

237 Krebs FC. *Sol Energy Mater Sol Cells*, 2009, 93: 394–412

238 Huang KM, Wong YQ, Lin MC, Chen CH, Liao CH, Chen JY, Huang YH, Chang YF, Tsai PT, Chen SH, Liao CT, Lee YC, Hong L, Chang CY, Meng HF, Ge Z, Zan HW, Horng SF, Chao YC, Wong HY. *Prog Photovolt Res Appl*, 2019, 27: 264–274

239 Distler A, Brabec CJ, Egelhaaf H. *Prog Photovolt Res Appl*, 2020, 29: 24–31

240 Pan W, Han Y, Wang Z, Luo Q, Ma C, Ding L. *J Semicond*, 2021, 42: 050301

241 Li Y, Li T, Lin Y. *Mater Chem Front*, 2021, 5: 2907–2930

242 Xu X, Li D, Yuan J, Zhou Y, Zou Y. *EnergyChem*, 2021, 3: 100046

243 Kang H, Kim G, Kim J, Kwon S, Kim H, Lee K. *Adv Mater*, 2016, 28: 7821–7861

244 Duan L, Uddin A. *Adv Sci*, 2020, 7: 1903259

245 Feron K, Nagle TJ, Rozanski LJ, Gong BB, Fell CJ. *Sol Energy Mater Sol Cells*, 2013, 109: 169–177

246 Norrman K, Gevorgyan SA, Krebs FC. *ACS Appl Mater Interfaces*, 2009, 1: 102–112

247 Kawano K, Pacios R, Poplavskyy D, Nelson J, Bradley DDC, Durrant JR. *Sol Energy Mater Sol Cells*, 2006, 90: 3520–3530

248 Norrman K, Madsen MV, Gevorgyan SA, Krebs FC. *J Am Chem Soc*, 2010, 132: 16883–16892

249 Tamai Y, Ohkita H, Namatame M, Marumoto K, Shimomura S, Yamanari T, Ito S. *Adv Energy Mater*, 2016, 6: 1600171

250 Inasaridze LN, Shames AI, Martynov IV, Li B, Mumyatov AV, Susarova DK, Katz EA, Troshin PA. *J Mater Chem A*, 2017, 5: 8044–8050

251 Wong HC, Li Z, Tan CH, Zhong H, Huang Z, Bronstein H, McCulloch I, Cabral JT, Durrant JR. *ACS Nano*, 2014, 8: 1297–1308

252 Heumueller T, Mateker WR, Distler A, Fritze UF, Cheacharoen R, Nguyen WH, Biele M, Salvador M, von Delius M, Egelhaaf HJ, McGehee MD, Brabec CJ. *Energy Environ Sci*, 2016, 9: 247–256

253 Manor A, Katz EA, Tromholt T, Krebs FC. *Adv Energy Mater*, 2011, 1: 836–843

254 Yan L, Ma CQ. *Energy Tech*, 2021, 9: 2000920

255 Neugebauer H, Brabec C, Hummelen JC, Sariciftci NS. *Sol Energy*

Mater Sol Cells, 2000, 61: 35–42

256 Chang CY, Tsai FY. *J Mater Chem*, 2011, 21: 5710–5715

257 Sapkota SB, Spies A, Zimmermann B, Dürr I, Würfel U. *Sol Energy Mater Sol Cells*, 2014, 130: 144–150

258 Channa IA, Distler A, Zaiser M, Brabec CJ, Egelhaaf H-. *Adv Energy Mater*, 2019, 9: 1900598

259 Distler A, Sauermann T, Egelhaaf HJ, Rodman S, Waller D, Cheon KS, Lee M, Guldi DM. *Adv Energy Mater*, 2014, 4: 1300693

260 Sachs-Quintana IT, Heumüller T, Mateker WR, Orozco DE, Cheacharoen R, Sweetnam S, Brabec CJ, McGehee MD. *Adv Funct Mater*, 2014, 24: 3978–3985

261 Yan L, Zhao W, Yang Y, *et al. Acta Polym Sin*, 2021, 52: 350–362

262 Du X, Heumueller T, Gruber W, Almora O, Classen A, Qu J, He F, Unruh T, Li N, Brabec CJ. *Adv Mater*, 2020, 32: 1908305

263 Yan L, Yi J, Chen Q, Dou J, Yang Y, Liu X, Chen L, Ma CQ. *J Mater Chem A*, 2017, 5: 10010–10020

264 Burlingame Q, Huang X, Liu X, Jeong C, Coburn C, Forrest SR. *Nature*, 2019, 573: 394–397

265 Gevorgyan SA, Espinosa N, Ciammaruchi L, Roth B, Livi F, Tsopanidis S, Züfle S, Queirós S, Gregori A, Benatto GAR, Corazza M, Madsen MV, Hösel M, Beliatis MJ, Larsen-Olsen TT, Pastorelli F, Castro A, Mingorance A, Lenzi V, Fluhr D, Roesch R, Maria Duarte Ramos M, Savva A, Hoppe H, Marques LSA, Burgués I, Georgiou E, Serrano-Luján L, Krebs FC. *Adv Energy Mater*, 2016, 6: 1600910

266 Gevorgyan SA, Madsen MV, Roth B, Corazza M, Hösel M, Søndergaard RR, Jørgensen M, Krebs FC. *Adv Energy Mater*, 2016, 6: 1501208

267 Tong Y, Xiao Z, Du X, Zuo C, Li Y, Lv M, Yuan Y, Yi C, Hao F, Hua Y, Lei T, Lin Q, Sun K, Zhao D, Duan C, Shao X, Li W, Yip HL, Xiao Z, Zhang B, Bian Q, Cheng Y, Liu S, Cheng M, Jin Z, Yang S, Ding L. *Sci China Chem*, 2020, 63: 758–765

268 Speller EM, Clarke AJ, Luke J, Lee HKH, Durrant JR, Li N, Wang T, Wong HC, Kim JS, Tsoi WC, Li Z. *J Mater Chem A*, 2019, 7: 23361–23377

269 Armin A, Li W, Sandberg OJ, Xiao Z, Ding L, Nelson J, Neher D, Vandewal K, Shoaee S, Wang T, Ade H, Heumüller T, Brabec C, Meredith P. *Adv Energy Mater*, 2021, 11: 2003570

270 Dang MT, Hirsch L, Wantz G. *Adv Mater*, 2011, 23: 3597–3602

271 Mateker WR, McGehee MD. *Adv Mater*, 2017, 29: 1603940

272 Rafique S, Abdullah SM, Sulaiman K, Iwamoto M. *Renew Sustain Energy Rev*, 2018, 84: 43–53

273 Gu H, Yan L, Saxena S, Shi X, Zhang X, Li Z, Luo Q, Zhou H, Yang Y, Liu X, Wong WWH, Ma CQ. *ACS Appl Energy Mater*, 2020, 3: 9714–9723

274 Yan L, Gu H, Li Z, Zhang J, Yang Y, Wang H, Liu X, Wei Z, Luo Q, Ma CQ. *Mater Adv*, 2020, 1: 1307–1317

275 Lindqvist C, Sanz-Velasco A, Wang E, Bäcke O, Gustafsson S, Olsson E, Andersson MR, Müller C. *J Mater Chem A*, 2013, 1: 7174–7180

276 Li N, Perea JD, Kassar T, Richter M, Heumueller T, Matt GJ, Hou Y, Güldal NS, Chen H, Chen S, Langner S, Berlinghof M, Unruh T, Brabec CJ. *Nat Commun*, 2017, 8: 14541

277 Peters CH, Sachs-Quintana IT, Mateker WR, Heumueller T, Rivnay J, Noriega R, Beiley ZM, Hoke ET, Salleo A, McGehee MD. *Adv Mater*, 2012, 24: 663–668

278 Heumueller T, Burke TM, Mateker WR, Sachs-Quintana IT, Vandewal K, Brabec CJ, McGehee MD. *Adv Energy Mater*, 2015, 5: 1500111

279 Yan L, Wang Y, Wei J, Ji G, Gu H, Li Z, Zhang J, Luo Q, Wang Z, Liu X, Xu B, Wei Z, Ma CQ. *J Mater Chem A*, 2019, 7: 7099–7108

280 Li Z, Shan J, Yan L, Gu H, Lin Y, Tan H, Ma CQ. *ACS Appl Mater Interfaces*, 2020, 12: 15472–15481

281 Li Z, Yan L, Shan J, Gu H, Lin Y, Wang Y, Tan H, Ma CQ. *Energy Technol*, 2020, 8: 2000266

282 Bertho S, Janssen G, Cleij TJ, Conings B, Moons W, Gadisa A, D'Haen J, Goovaerts E, Lutsen L, Manca J, Vanderzande D. *Sol Energy Mater Sol Cells*, 2008, 92: 753–760

283 Zhang K, Guo J, Zhang L, Qin C, Yin H, Gao X, Hao X. *Adv Funct Mater*, 2021, 31: 2100316

284 Cheng P, Yan C, Lau TK, Mai J, Lu X, Zhan X. *Adv Mater*, 2016, 28: 5822–5829

285 Xiao M, Zhang K, Jin Y, Yin Q, Zhong W, Huang F, Cao Y. *Nano Energy*, 2018, 48: 53–62

286 Gasparini N, Salvador M, Strohm S, Heumueller T, Levchuk I, Wadsworth A, Bannock JH, de Mello JC, Egelhaaf HJ, Baran D, McCulloch I, Brabec CJ. *Adv Energy Mater*, 2017, 7: 1700770

287 You J, Dou L, Yoshimura K, Kato T, Ohya K, Moriarty T, Emery K, Chen CC, Gao J, Li G, Yang Y. *Nat Commun*, 2013, 4: 1446

288 Hong L, Yao H, Cui Y, Yu R, Lin YW, Chen TW, Xu Y, Qin J, Hsu CS, Ge Z, Hou J. *Small*, 2021, 17: 2101133

289 Günther M, Blätte D, Oechsle AL, Rivas SS, Yousefi Amin AA, Müller-Buschbaum P, Bein T, Ameri T. *ACS Appl Mater Interfaces*, 2021, 13: 19072–19084

290 Liu Q, Jiang Y, Jin K, Qin J, Xu J, Li W, Xiong J, Liu J, Xiao Z, Sun K, Yang S, Zhang X, Ding L. *Sci Bull*, 2020, 65: 272–275

291 Lin Y, Firdaus Y, Isikgor FH, Nugraha MI, Yengel E, Harrison GT, Hallani R, El-Labban A, Faber H, Ma C, Zheng X, Subbiah A, Howells CT, Bakr OM, McCulloch I, Wolf SD, Tsetseris L, Anthopoulos TD. *ACS Energy Lett*, 2020, 5: 2935–2944

292 Cheng P, Bai H, Zawacka NK, Andersen TR, Liu W, Bundgaard E, Jørgensen M, Chen H, Krebs FC, Zhan X. *Adv Sci*, 2015, 2: 1500096

293 Mao L, Luo B, Sun L, Xiong S, Fan J, Qin F, Hu L, Jiang Y, Li Z, Zhou Y. *Mater Horiz*, 2018, 5: 123–130

294 Du X, Heumueller T, Gruber W, Classen A, Unruh T, Li N, Brabec CJ. *Joule*, 2019, 3: 215–226

295 Luke J, Speller EM, Wadsworth A, Wyatt MF, Dimitrov S, Lee HKH, Li Z, Tsoi WC, McCulloch I, Bagnis D, Durrant JR, Kim J. *Adv Energy Mater*, 2019, 9: 1803755

296 Liu ZX, Yu ZP, Shen Z, He C, Lau TK, Chen Z, Zhu H, Lu X, Xie Z, Chen H, Li CZ. *Nat Commun*, 2021, 12: 3049

297 Jiang Y, Sun L, Jiang F, Xie C, Hu L, Dong X, Qin F, Liu T, Hu L, Jiang X, Zhou Y. *Mater Horiz*, 2019, 6: 1438–1443

298 Park S, Son HJ. *J Mater Chem A*, 2019, 7: 25830–25837

299 Liu B, Han Y, Li Z, Gu H, Yan L, Lin Y, Luo Q, Yang S, Ma CQ. *Sol RRL*, 2021, 5: 2000638

300 Ghasemi M, Hu H, Peng Z, Rech JJ, Angunawela I, Carpenter JH, Stuard SJ, Wadsworth A, McCulloch I, You W, Ade H. *Joule*, 2019, 3: 1328–1348

301 Xin Y, Zeng G, OuYang JY, Zhao X, Yang X. *J Mater Chem C*, 2019, 7: 9513–9522

302 Upama MB, Elumalai NK, Mahmud MA, Wright M, Wang D, Xu C, Uddin A. *Sol Energy Mater Sol Cells*, 2018, 176: 109–118

303 Hu L, Jiang Y, Sun L, Xie C, Qin F, Wang W, Zhou Y. *J Phys Chem Lett*, 2021, 12: 2607–2614

304 Han Y, Dong H, Pan W, Liu B, Chen X, Huang R, Li Z, Li F, Luo Q, Zhang J, Wei Z, Ma CQ. *ACS Appl Mater Interfaces*, 2021, 13: 17869–17881

305 Liu H, Wang W, Zhou Y, Li Z. *J Mater Chem A*, 2021, 9: 1080–1088

306 Zhu X, Liu S, Yue Q, *et al. CCS Chem*, 2021, 1070–1080

307 Xiao J, Ren M, Zhang G, Wang J, Zhang D, Liu L, Li N, Brabec CJ, Yip HL, Cao Y. *Sol RRL*, 2019, 3: 1900077

308 Xu X, Xiao J, Zhang G, Wei L, Jiao X, Yip HL, Cao Y. *Sci Bull*, 2020, 65: 208–216

309 Sun R, Wang W, Yu H, Chen Z, Xia XX, Shen H, Guo J, Shi M, Zheng Y, Wu Y, Yang W, Wang T, Wu Q, Yang YM, Lu X, Xia J, Brabec CJ, Yan H, Li Y, Min J. *Joule*, 2021, 5: 1548–1565

310 Liao Q, Kang Q, Yang Y, *et al. CCS Chem*, 4: 938–948